Pyrochlore as nuclear waste form: actinide uptake and chemical stability

Sarah Charlotte Finkeldei

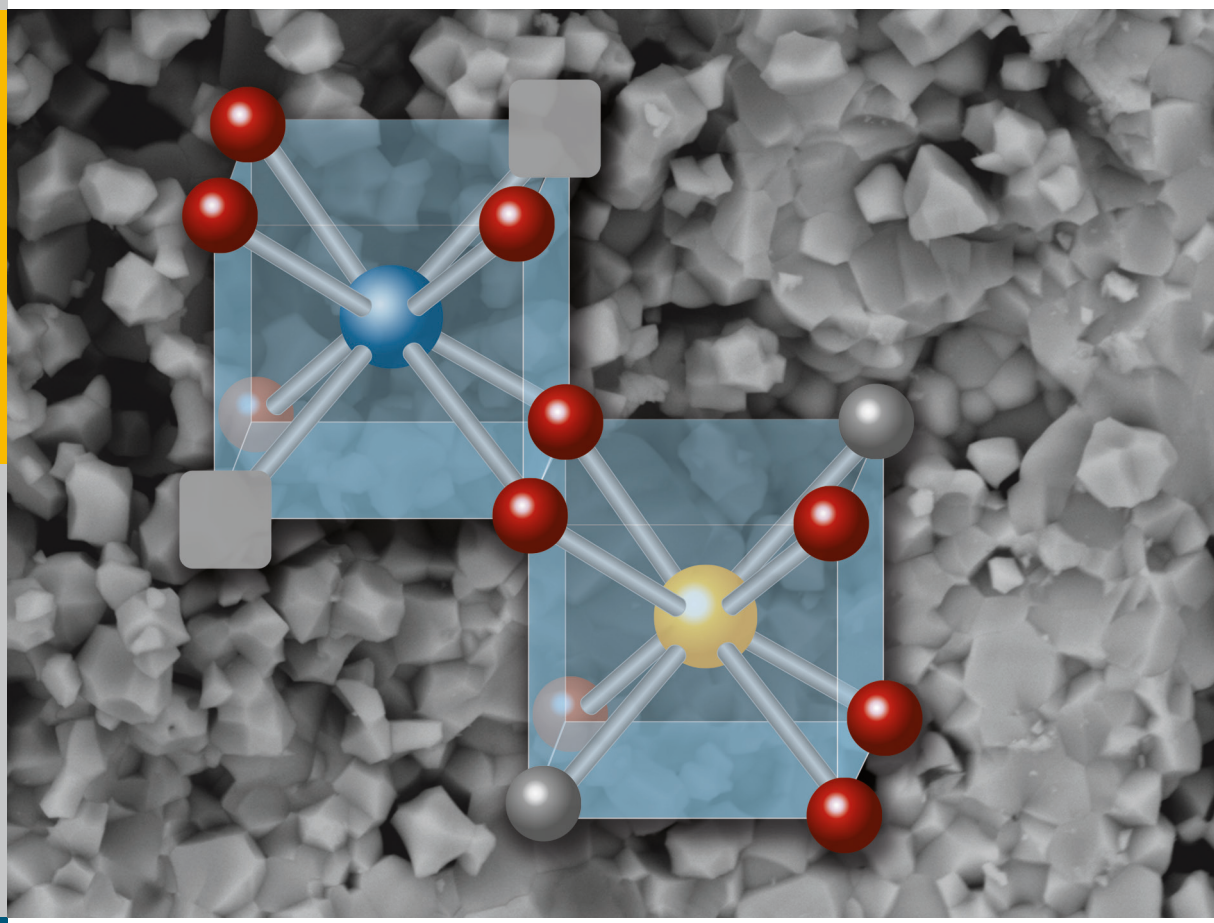

Energie & Umwelt / Energy & Environment
Band / Volume 276
ISBN 978-3-95806-072-2

JÜLICH
FORSCHUNGSZENTRUM

Schriften des Forschungszentrums Jülich
Reihe Energie & Umwelt / Energy & Environment Band / Volume 276

Forschungszentrum Jülich GmbH
Institut für Energie- und Klimaforschung
Nukleare Entsorgung und Reaktorsicherheit (IEK-6)

Pyrochlore as nuclear waste form: actinide uptake and chemical stability

Sarah Charlotte Finkeldei

Schriften des Forschungszentrums Jülich
Reihe Energie & Umwelt / Energy & Environment Band / Volume 276

ISSN 1866-1793 ISBN 978-3-95806-072-2

Bibliographic information published by the Deutsche Nationalbibliothek.
The Deutsche Nationalbibliothek lists this publication in the Deutsche Nationalbibliografie; detailed bibliographic data are available in the Internet at http://dnb.d-nb.de.

Publisher and Distributor: Forschungszentrum Jülich GmbH
Zentralbibliothek
52425 Jülich
Tel: +49 2461 61-5368
Fax: +49 2461 61-6103
Email: zb-publikation@fz-juelich.de
www.fz-juelich.de/zb

Cover Design: Grafische Medien, Forschungszentrum Jülich GmbH

Printer: Grafische Medien, Forschungszentrum Jülich GmbH

Schriften des Forschungszentrums Jülich
Reihe Energie & Umwelt / Energy & Environment, Band / Volume 276

D 82 (Diss. RWTH Aachen University, 2014)

ISSN 1866-1793
ISBN 978-3-95806-072-2

The complete volume is freely available on the Internet on the Jülicher Open Access Server (JuSER) at www.fz-juelich.de/zb/openaccess.

Kein Wissen scheint schwerer zu erwerben als die Erkenntnis, wann man aufhören muss.

Jonathan Swift, ein Tonnenmärchen.

Meiner Mama

Abstract

Radioactive waste is generated by many different technical and scientific applications. For the past decades, different waste disposal strategies have been considered. Several questions on the waste disposal strategy remain unanswered, particularly regarding the long-term radiotoxicity of minor actinides (Am, Cm, Np), plutonium and uranium. These radionuclides mainly arise from high level nuclear waste (HLW), specific waste streams or dismantled nuclear weapons. Although many countries have opted for the direct disposal of spent fuel, from a scientific and technical point of view it is imperative to pursue alternative waste management strategies. Apart from the vitrification, especially for trivalent actinides and Pu, crystalline ceramic waste forms are considered. In contrast to glasses, crystalline waste forms, which are chemically and physically highly stable, allow the retention of radionuclides on well-defined lattice positions within the crystal structure. Besides polyphase ceramics such as SYNROC, single phase ceramics are considered as tailor made host phases to embed a specific radionuclide or a specific group. Among oxidic single phase ceramics pyrochlores are known to have a high potential for this application. This work examines ZrO_2 based pyrochlores as potential nuclear waste forms, which are known to show a high aqueous stability and a high tolerance towards radiation damage.

This work contributes to (1) understand the phase stability field of pyrochlore and consequences of non-stoichiometry which leads to pyrochlores with mixed cationic sites. Mixed cationic occupancies are likely to occur in actinide-bearing pyrochlores. (2) The structural uptake of radionuclides themselves was studied. (3) The chemical stability and the effect of phase transition from pyrochlore to defect fluorite were probed. This phase transition is important, as it is the result of radiation damage in ZrO_2 based pyrochlores.

$ZrO_2 – Nd_2O_3$ pellets with pyrochlore and defect crystal structure were synthesised via a wet-chemical coprecipitation route to obtain highly homogeneous ceramics. Their structure-properties relationships were studied by a combination of different characterisation techniques, e.g. powder X-Ray diffraction (XRD), transmission electron microscopy (TEM), scanning electron microscopy (SEM) and luminescence spectroscopy. These complementary techniques were chosen to gain insight into the radionuclide uptake and order-disorder transition from a bulk to a local structural level.

The transition of pyrochlore to the less ordered defect fluorite phase was examined by XRD and TEM and recognized to be a gradual transition. This transition was proven to have no significant impact on the aqueous durability under acidic conditions. In addition to their high radiation tolerance ZrO_2 based pyrochlores are therefore expected to ensure high long-term durability even during the decay of embedded radionuclides.

The radionuclide uptake on well-defined lattice positions within the pyrochlore crystal structure was probed by luminescence spectroscopy (time resolved laser fluorescence spectroscopy, TRLFS) of Cm and Eu doped $La_2Zr_2O_7$ pyrochlores and defect fluorite samples. TRLFS is an ideal method to unravel the lattice site by probing the local environment of the dopant. According to TRLFS results Eu and Cm adopt the A site within the pyrochlore crystal structure and regular cation lattice sites in the defect fluorite. In addition, a minor species is present in the pyrochlore which was identical to the major species observed in the defect fluorite. Vice versa, the defect fluorite contains a minor species which has adopted the pyrochlore environment. This is in good agreement with the TEM findings. Due to the different pyrochlore and defect fluorite species, TRLFS could be used as a tool to quantify radiation damage in ZrO_2 based pyrochlore nuclear waste forms.

In order to more closely imitate a realistic waste form 5 mol% and 10 mol% Pu-pyrochlores were synthesised. To this end, a wet chemical synthesis route was developed. Characterisation by XRD, SEM and EDX indicates a homogeneous structural uptake of Pu-239 into pyrochlore.

Extensive dissolution studies were carried out on Nd_2O_3 - ZrO_2 pyrochlores using static and dynamic experimental setups including variations of pH, temperature and chemical composition. Typical for all experiments is an initial incongruent dissolution with a preferential Nd release. The higher initial rates decreased with time until a steady state was reached oftentimes approaching a congruent dissolution of Nd and Zr. The steady state of the Zr release was reached after 10 - 20 days in experiments at 110 °C and $c(H^+)$ = 0.1 mol/L. Differences in the Zr-O and Nd-O bonding strengths may be partly responsible for the higher initial release rate of Nd. The activation energy E_a (Zr-based pyrochlore) = 47 kJ/mol and E_a = 28 kJ/mol for the defect fluorite indicated a surface controlled dissolution mechanism. A rough estimation for a $Nd_2Zr_2O_7$ pyrochlore leads to a dissolution rate in the order of 10^{-10} $gm^{-2}d^{-1}$ under repository relevant conditions, demonstrating its ability to serve as a highly durable nuclear waste form.

Complementary to the macroscopic approach microscopic observations were made to gain a more detailed view into the dissolution. SEM and vertical scanning interferometry provided new insights into the dissolution kinetics at grain boundaries and the surface retreat of individual grains. These microscopic methods indicate a temporal evolution of the surface reactivity. The combination of macroscopic and microscopic dissolution studies allowed first insights into the dissolution mechanism of a ZrO_2 – Nd_2O_3 pyrochlore series which is essential for a profound understanding of the chemical stability of a nuclear waste form.

Kurzzusammenfassung

Radioaktive Abfälle entstehen bei verschiedenen technischen und wissenschaftlichen Anwendungen. Innerhalb der letzten Jahrzehnte sind unterschiedliche Entsorgungspfade entwickelt worden. Im Hinblick auf die Langzeitradiotoxizität von minoren Actiniden (Am, Cm, Np), Plutonium und Uran die aus hochaktiven, wärmeentwickelnden Abfällen, spezifischen Abfallströmen oder abgereicherten Waffen stammen, gibt es noch offene Fragen bezüglich der Endlagerung. Obwohl sich einige Länder für die direkte Endlagerung abgebrannter Brennelemente entschieden haben, ist es aus wissenschaftlicher und technischer Sicht wichtig alternative Entsorgungsstrategie weiter zu verfolgen, die in anderen Ländern entwickelt werden. Besonders für Plutonium und die dreiwertigen Actiniden werden neben der Verglasung z.B. maßgeschneiderte Keramiken als alternative Abfallformen untersucht. Im Gegensatz zu amorphen Gläsern werden die Radionuklide in den kristallinen Keramiken auf genau definierten Gitterpositionen innerhalb der Kristallstruktur immobilisiert, woraus sich eine hohe chemische und physikalische Beständigkeit dieser Abfallform ergibt. Anfänglich wurden besonders mehrphasige Keramiken, wie z.B. SYNROC hinsichtlich ihrer Eignung als potentielle nukleare Abfallform betrachtet. Einphasige Keramiken sind besonders interessant für die maßgeschneiderte Immobilisierung einzelner Radionuklide nachdem diese vom übrigen Abfallstrom abgetrennt worden sind. Neben anderen geeigneten Keramiktypen wurde hierfür die Gruppe der Pyrochlore als interessanter Kandidat identifiziert.

Im Fokus dieser Arbeit stehen ZrO_2 basierte Pyrochlore als potentielle Wirtsphasen für die Einbindung von Radionukliden. Diese zeichnen sich besonders durch ihre hohe wässrige Beständigkeit sowie ihre hohe Toleranz gegenüber Strahlenschäden als potentielle nukleare Abfallformen aus. Diese Arbeit liefert Beiträge zum Verständnis (1) des Stabilitätsbereiches von ZrO_2 – Nd_2O_3 Pyrochlor, besonders im Hinblick auf die nicht-stöchiometrischen Pyrochlore und den Übergang zur weniger geordneten Defektfluoritstruktur. Dies ist im Rahmen der Dotierung von Pyrochloren mit Actiniden von Interesse, da dieser Einbau meist zur Bildung von nicht-stöchiometrischen Pyrochloren, d.h. mehreren unterschiedlichen Kationen auf einer Kationenposition, führt. (2) Der strukturelle Einbau von Actiniden wurde detailliert untersucht und (3) die Korrosionsbeständigkeit wurde besonders im Hinblick auf den Phasenübergang von Pyrochlor zu Defektfluorit analysiert.

ZrO_2 – Nd_2O_3 Keramikpellets mit Pyrochlor und Defektfluoritstruktur wurden im Rahmen dieser Arbeit durch nasschemische Copräzipitation hergestellt. Ihre Struktur-Eigenschafts-beziehungen wurden mittels Röntgenpulverdiffraktometrie (XRD), Transmissions- und Rasterelektronenmikroskopie (TEM, REM) und Lumineszenzspektroskopie (time resolved laser fluorescence spectroscopy, TRLFS) betrachtet. Diese Methoden ermöglichen eine strukturelle Charakterisierung der Keramiken von der Gesamtprobe bis hin zur lokalen

Struktur. Der Übergang von der geordneten Pyrochlorstruktur zur weniger geordneten Defektfluoritstruktur wurde mittels XRD und TEM betrachtet. Die Ergebnisse deuten auf einen graduellen Übergang von Pyrochlor zu Defektfluorit hin. Anhand von Auflösungsexperimenten wurde festgestellt, dass dieser Strukturübergang keinen signifikanten Einfluss auf die Korrosionsbeständigkeit hat, was die Eignung von ZrO_2-basierten Pyrochloren als potentielle Abfallformen unterstreicht.

Der strukturelle Einbau von Cm und Eu als Modellsysteme für die Actiniden auf einer definierten regulären Kristallgitterposition des Pyrochlors wurde mittels TRLFS bestätigt. Eine zweite, minore Spezies innerhalb der Pyrochlorprobe zeigt eine für den Defektfluorit typische lokale Umgebung. Diese Ergebnisse wurden von TEM-Messungen bestätigt, die ebenfalls auf Defektfluorit-Anteile im Pyrochlor hindeuten und Pyrochlor-Anteile im Defektfluorit. TRLFS könnte zukünftig aufgrund der unterschiedlichen Spezies in den beiden Strukturen zur Quantifizierung von Strahlenschäden in ZrO_2 basierten Pyrochloren Anwendung finden.

In Annäherung an eine reale Abfallform wurden Pyrochlore mit einem Pu-Anteil von 5 mol% und 10 mol% über eine nasschemischen Fällungsreaktion hergestellt. XRD, REM und EDX Ergebnisse zeigen einen strukturellen Einbau von Pu in Pyrochlor.

Statische und dynamische Auflösungsexperimente wurden an ZrO_2 - Nd_2O_3 Pyrochloren mit Variation von z.B. pH und Temperatur durchgeführt und zeigten in jedem Fall eine anfänglich stark inkongruente Auflösung mit bevorzugter Nd-Freisetzung. Oft näherten sich die anfänglich sehr unterschiedlichen Nd- und Zr-basierte Rate im später beobachteten stationären Zustand soweit an, dass die Auflösung in dieser Phase der Auflösung als kongruent angesehen werden kann. Eine geringere Stärke von Nd-O im Vergleich zu Zr-O Bindungen könnte u.a. für die bevorzugte Nd-Freisetzung verantwortlich sein. Zr-basierte Aktivierungsenergien von 47 kJ/mol für den Pyrochlor und 28 kJ/mol für den Defektfluorit deuten auf eine oberflächenkontrollierte Auflösung hin. Aus den neu bestimmten Daten kann eine Pyrochlor-Auflösungsrate für endlagerrelevante Bedingungen abgeschätzt werden, die in der Größenordnung von 10^{-10} $gm^{-2}d^{-1}$ liegt. Diese sehr niedrige Auflösungsrate verdeutlicht die Eignung von ZrO_2-basierten Pyrochloren und Defektfluoriten als potentielle nukleare Abfallform.

Komplementär zu dem obigen makroskopischen Ansatz wurde REM und Weißlichtinterferometrie verwendet, um ein detaillierteres Verständnis für die Pyrochlorauflösung zu erlangen. Anhand der mikroskopischen Methoden wurde eine zeitliche Entwicklung der Oberflächenreaktivität sichtbar, die am Anfang durch Korngrenzen und Tripelpunkte, später durch den Rückzug gesamter Körner und weitere Auflösung an bestimmten Korngrenzen bestimmt wird.

Contents

Abbreviations

AFM	atomic force microscopy
An	actinides
BF	bright field
BSED	Backscattered electron detector
CCD	Charge-Coupled-Device
DF	dark field
EDX	energy-dispersive X-ray spectroscopy
EXAFS	extended X-ray absorption fine structure
fcc	face centered cubic
FIB	focused ion beam
HLW	High level waste
HMTA	hexamethylenetetramine
IAP	ion activity product
ICP-MS	inductive coupled plasma mass spectrometry
ICP-OES	inductively coupled plasma atomic emission spectrometry
LFD	large field detector
MA	minor actinides
PFA	perfluoroalkoxy polymer
pzc	point of zero charge
PTFE	polytetrafluoroethylene
SAD	selected-area diffraction
SEM	Scanning electron microscope
SI	Saturation index
SYNROC	synthetic rock
TEM	transmission electron microscope
TRLFS	Time resolved laser fluorescence spectroscopy
TST	Transition state theory
VSI	vertical scanning interferometry
XAFS	X-ray absorption fine structure
XANES	X-ray absorption near edge structure
XRD	X-ray Diffraction

1 Introduction

The safe disposal of radioactive waste which is generated by many different technical and scientific applications is a challenging issue. It is a general consensus within the scientific community that the safest option will be a deep geological waste repository [1]. During the last decades different waste disposal strategies were considered. The direct disposal of spent fuel and the vitrification of separated waste streams are well-established. However, from a scientific and technical point of view it is reasonable to pursue alternative waste management strategies. Some open questions remain regarding the long-term radiotoxicity of minor actinides (Am, Cm, Np), plutonium and uranium which arise from high level nuclear waste (HLW), specific waste streams or dismantled nuclear weapons.

Within the framework of innovative waste management strategies ceramics are considered as an alternative nuclear waste form [2]. One important advantage of ceramics compared to glasses is their crystallinity which ensures retention of the radionuclides on defined lattice sites inside a chemically and physically very stable host phase [2]. A crystalline waste form allows a full characterisation of its chemical composition, the identification of the present phases and the exact localisation of the radionuclide inside the host phase. This information enables a profound understanding of the final waste form and its stability. Some ceramic systems are also known for their superior stability against aqueous dissolution e.g. ZrO_2 or TiO_2.

Polyphase ceramics were developed to directly substitute nuclear waste glass, because they can accommodate a number of different radionuclides. A poylphase ceramic called SYNROC (**syn**thetic **roc**k) was developed by Ringwood in 1979 [3]. Different types of SYNROC were evolved for the conditioning of various waste streams. SYNORC-C mainly consists of four titanate ceramics: zirconolite, hollandite, perovskite and titanium oxide [4]. One advantage of SYNROC is its superior groundwater durability in comparison to borosilicate glass [5].

A major concern for a crystalline waste form is the change and potential loss of its valuable properties such as e.g. a high aqueous durability and high radiation tolerance as consequence of radiation damage. Several titanates are known to transform to amorphous phases due to radiation damage [6].

In contrast to the well-established vitrification of reprocessed spent fuel in borosilicate glasses the fabrication of SYNROC is much more demanding due to its complex composition of several crystalline phases. Moreover, the immobilisation of a separated waste stream in a borosilicate glass was found to be suitable and already well-established. Therefore, the polyphase ceramics did not become established in the framework of nuclear waste management.

Spent fuel, glass and polyphase ceramics were waste forms which include all radionuclides of a specific waste stream although the contribution to the long-term radiotoxicity varies and therefore much volume is used for the storage of waste which may not contribute much to the long-term dose. Especially the minor actinides (MA = Am, Cm, Np) contribute a high share of the long-term radiotoxicity [7] even though they contribute only a small share of the nuclear waste from a volumetric point of view (0.1% [8]). Moreover, significant amounts of excess Pu either from the reprocessing of civil Pu (e.g. 123 tonnes in Great Britain [9]) or from dismantled nuclear weapons are stored in different countries and need to be safely disposed.

Several of the phases included in SYNROC were later on studied as single phase ceramics to immobilise a specific nuclide or a specific group, e.g. the MA in a tailor made ceramic. Single phase ceramics are especially of interest for separated civil Pu as well as for excess weapon Pu. A high aqueous durability, a high radiation tolerance as well as the structural uptake of the radionuclides make them attractive potential nuclear waste forms. Ceramic waste forms need to exhibit some porosity to avoid cracking of the matrix due to fission gas release and α-decay. This can be adjusted by choosing an appropriate synthesis route. The advantage of the tailor made immobilisation of a certain radionuclide comes along with the drawback of a necessary reprocessing step in order to separate this radionuclide from the main waste stream.

Beside rare earth phosphates like monazites, in particular titanate based ceramics such as brannerite, zirconolite, perovskite and pyrochlore are examined as potential nuclear waste forms [10]. Natural analogues exist for many of these ceramics, containing a natural share of radionuclides for more than 40 million years [2]. These natural analogues prove a high chemical stability, a high durability and a distinct tolerance towards radiation damage of certain ceramic waste forms. However, it is not fully understood what causes this high stability and the geological environment also has an impact on the chemical durability [5]. The main drawback of the titanate phases, especially of the brannerite is their amorphisation due to radiation damage which is sometimes accompanied by a lowering of the aqueous durability [2]. Besides the titanate or stannate based pyrochlores zirconate based pyrochlores are of interest, due to their high radiation tolerance [11] ensuring a high long-term durability. From technical applications, ZrO_2 based ceramics are known to be extremely corrosion resistant.

In order to include ceramic waste forms into a safety assessment for a deep geological nuclear waste repository, a process understanding of these outstanding properties is required. The HLW is foreseen to be stored in a deep geological repository typically in 500 – 1500 m depth [12]. Several geological environments are considered for a deep geological repository such as granite, clay rock, salt rock and tuff rock [13]. Granite is mostly considered

by Finland, Sweden and Canada. In Germany clay rock or salt rock is considered for a deep geological repository, whereas the options currently considered by the US are salt rock or tuff rock [14]. All of these concepts have their assets and drawbacks and often it is a geological issue which concept is chosen due to the availability in the corresponding country. Especially for HLW, the properties of a nuclear waste form are considered as part of the engineered barrier.

Here, the properties of ZrO_2 based pyrochlores with respect to their radionuclide uptake and chemical stability were investigated. Qualitatively ZrO_2 based pyrochlores were already well known for their high radiation tolerance and chemical stability [11]. However, there is a lack of quantitative details concerning the rate of dissolution at repository relevant conditions, the phase stability field of ZrO_2 based pyrochlores and the uptake of radionuclides and these aspects have therefore been in the focus of this study.

2 Scientific and theoretical background

2.1. The ZrO_2-Nd_2O_3 system

ZrO_2 is a chemically, thermally and mechanically robust oxide [15]. Cubic zirconia and zirconate based pyrochlores exhibit a higher chemical durability than zirconolite or Ti-based pyrochlores [2]. In general, ZrO_2 based ceramic systems are well studied, but only limited information is available on the ZrO_2-Nd_2O_3 system. Below two selected phase diagrams of the ZrO_2-Nd_2O_3 system are discussed with a special focus on the pyrochlore stability field. These diagrams demonstrate the variable and complex behaviour as a function of composition and temperature including up to seven distinct cubic, hexagonal and tetragonal phases.

Figure 1a shows the ZrO_2 – Nd_2O_3 phase diagram from Rouanet (1971) [16] for temperatures above 1400 °C. The liquidus curves were measured by the author via thermal analysis, whereas the solidus curves were estimated. According to this phase diagram the pyrochlore solid solution can be obtained in a narrow region around the stoichiometric $Nd_2Zr_2O_7$ composition. At temperatures above 2100 °C and 2050 °C for the ZrO_2 rich or rather the Nd_2O_3 rich region the stability field of the pyrochlore crystal structure is expanded to the range between 22 mol% up to 45 mol% Nd_2O_3. Below these temperatures Rouanet reports exsolution into pyrochlore and a cubic phase. Within the ZrO_2 rich region the cubic phase has a fluorite type structure, whereas a Tl_2O_3 type structure is reported for the Nd_2O_3 rich region. At a temperature around 2300 °C and above the pyrochlore phase is no longer stable and Rouanet describes the presence of two cubic phases. However it is not clear at which chemical composition the Tl_2O_3 type structure is the favoured phase over the fluorite type structure. An eutectic point is reported at 1440 °C for equal amounts of ZrO_2 and Nd_2O_3. The cubic Tl_2O_3-type phase is frozen into a mixed pyrochlore and a hexagonal phase. The further details of this phase diagram are not discussed, because they were not in the focus of this work.

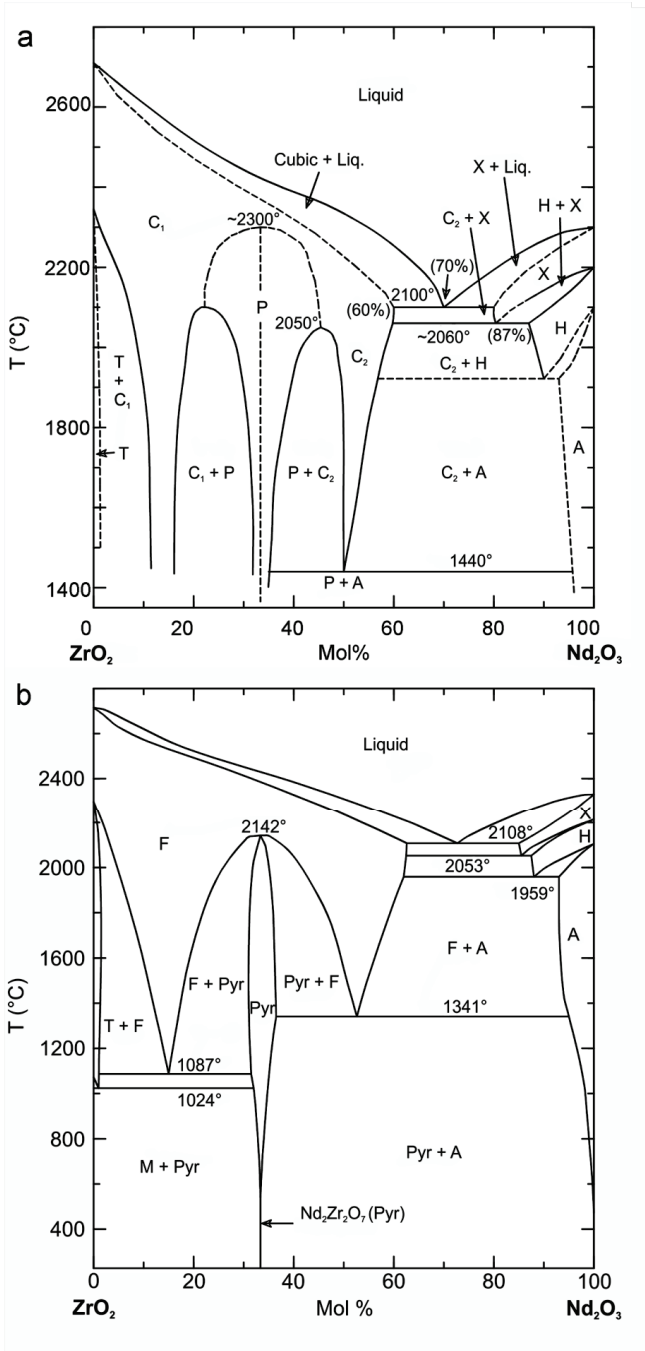

Figure 1: ZrO_2-Nd_2O_3 **phase diagrams (a) adapted from Rouanet [16] with A = hexagonal ss, C_1 = cubic ss of the fluorite type, C_2 = cubic ss of the Tl_2O_3 type, H = hexagonal ss, P = pyrochlore-type compound, T = tetragonal ss, X = cubic ss; (b) calculated ZrO_2 – Nd_2O_3 phase diagram adapted from Fabrichnaya [17]. With A = Nd_2O_3; Pyr = pyrochlore $Nd_2Zr_2O_7$; M, F, and T are forms of ZrO_2.**

Figure 1b shows the calculated phase diagram for ZrO_2-Nd_2O_3 by Fabrichnaya and Seifert (2008) [17]. At a first glance this phase diagram is similar to the phase diagram of Rouanet (1971). A temperature dependent phase transition of $Nd_2Zr_2O_7$ from pyrochlore crystal structure to the defect fluorite was calculated to occur at 2142 °C. Rouanet proposed a higher transition temperature of 2300 °C. In contrast to Rouanet's phase diagram there is no broadening of the pyrochlore stability field in the phase diagram suggested by Fabrichnaya at higher temperatures. Moreover, for ZrO_2 and Nd_2O_3 rich phases according to Fabrichnaya there should not be a differentiation between several cubic compounds which coexist with pyrochlore due to exsolution. This appears to be more reasonable because there is no phase boundary between the two cubic phases C_1 and C_2 in Rouanet (1971). At temperatures between 1400 °C and 1600 °C as applied in this study, Fabrichnaya suggests a miscibility gap on both sides of the pyrochlore stability field and the transition to a fluorite type phase which later on will be referred to as defect fluorite.

According to Fabrichnaya and Seifert (2008), at temperatures below 700 °C only the stoichiometric $Nd_2Zr_2O_7$ is stable and neither a small ZrO_2 excess nor a small excess of Nd_2O_3 can be accommodated in the pyrochlore phase. The above described phase diagrams show that the $Nd_2Zr_2O_7$ pyrochlore is a high temperature phase. Therefore, the pyrochlore has to be considered as metastable at ambient temperatures.

2.2. Synthesis of ZrO_2 - Nd_2O_3 ceramic pellets

Ceramics are a group of non-metallic, inorganic materials which are produced by sintering at high temperatures [18]. In contrast to other studies which only produced ceramic powders [19-20], here ceramic pellets were fabricated. These pellets are characterised by their compact, defined and commonly well-established microstructure.

The fabrication of ceramic pellets involves two major steps. First, a highly reactive powder needs to be synthesised which then promotes the sintering during the later ceramic body formation. Both steps are discussed in detail below.

2.2.1 Powder fabrication

In general two different synthesis routes have been described in the literature: dry synthesis routes via solid state reactions or wet chemical routes, like precipitation or coprecipitation reactions. Within a solid state reaction the educts are mixed by grinding or ball milling which complicates a mixing process at the molecular level. To synthesise homogeneous ceramics, wet synthesis routes are preferable. Therefore all synthesis routes used within this work are wet chemical synthesis routes. For these types of reactions the possibility of mixing the different educts at the molecular scale appears likely.

Within this work two types of precipitation reactions and a sol-gel synthesis were carried out. A first attempt was a precipitation of the hydroxides with gaseous ammonia as precipitation agent. As described in the diploma thesis of Finkeldei [21] this might lead to at least two different precipitation types.

Figure 2a schematically shows that (I) starting from a metal salt solution (II) first $Zr(OH)_4$ starts to precipitate around a pH of 2-3 (III) whereas $Nd(OH)_3$ is formed at a higher pH. To obtain a highly homogeneous precipitate and later on a very homogeneous ceramic the reverse dropping procedure according to Chen [22] was applied. In contrast to the subsequent precipitation of the different metal hydroxides a coprecipitate of the metal hydroxides is obtained. Figure 2b shows that (I) adding the mixed metal salt solution to aqueous ammonia as precipitation agent (II) assures a coprecipitation of the metal hydroxides due to a constant, high pH during the whole precipitation procedure. In this case the hydroxides are already mixed at the molecular level.

The sol-gel process is an alternative wet chemical synthesis route to the coprecipitation reaction. A homogeneous sol or solution is transformed into a gel via a cross linking process of the particles or ions. The networking process can be initialized by e.g. a pH change. The gel formation is therefore a solidification process of the sol or solution. The gel itself is amorphous and the crystallisation takes place during the sintering procedure [23].

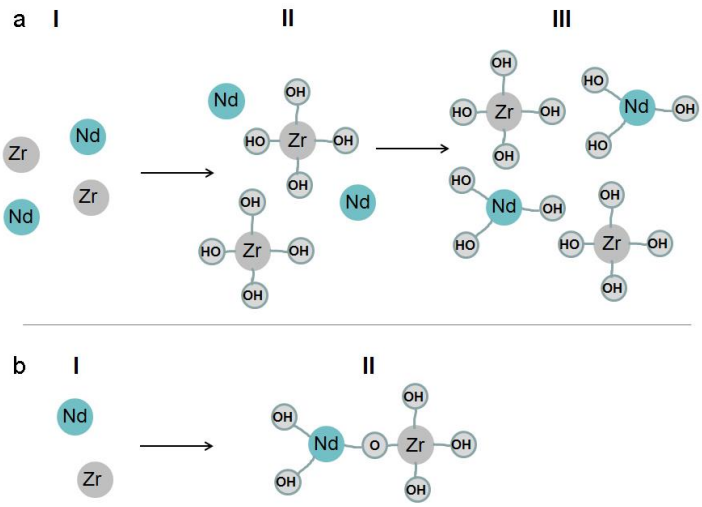

Figure 2: Schematic drawing for different precipitation mechanisms of $Zr(OH)_4$ and $Nd(OH)_3$. (a) Starting from a metal salt solution with Nd and Zr cations (I) the addition of e.g. gaseous ammonia leads first to the formation of $Zr(OH)_4$ (II) and $Nd(OH)_3$ is precipitated subsequently (III); (b) addition of the metal salt solution (I) to a precipitation agent as liquid ammonia leads to a coprecipitation of $Nd(OH)_3$ and $Zr(OH)_4$ (II) due to a constantly high pH. Adapted from Chen [22].

The sol-gel route is an entirely dust-free process which makes it very attractive for the synthesis of actinide- (An) bearing ceramics. One of the main drawbacks is the demanding precursor formulation for different chemical compositions which limited the applicability of this reaction type for this work. The mechanism of the internal gelation with hexamethylenetetramine (HMTA) is described in detail elsewhere [21]. The sol-gel route is a promising alternative synthesis procedure besides the coprecipitation because a homogeneous sol or solution solidifies as it is by preserving the homogeneity of the starting mixture. Moreover, this synthesis route allows the synthesis of porous beads and ceramics which could be used for infiltration reactions of e.g. actinides [24].

For ceramics, which are considered as potential nuclear waste forms, the presence of pores is indispensable, as the α-decay of the embedded radionuclides will lead to a release of gaseous He. This gas needs to be stored inside the pores or released through them. Otherwise gas formation would lead to the evolution of cracks within the matrix [25]. Therefore, the ceramics produced for this study were all porous materials with a typical porosity of about 10 %.

2.2.2 Ceramic pellet formation

The formation of a ceramic pellet from powders was achieved by cold or hot pressing.

Cold pressing – After cold pressing of a pellet a subsequent sintering process needs to be applied to obtain a ceramic. One of the main advantages of cold pressing is the preservation of the adjusted stoichiometry, because the sintering procedure can be carried out in air. In general a cold press is a relatively simple experimental setup.

Hot pressing – This method allows a simultaneous sintering and pressing. This permits a rotation and movement of the particles at all time, leading to fresh and therefore, highly sintering active contact areas of the particles. Therefore a more advanced microstructure and higher density can be achieved compared to cold pressing and sintering. However, the setup is more complex and often times include graphite based tools which may influence the purity of the final ceramic.

2.3. Structural characterisation of ZrO_2 - Nd_2O_3 ceramics

2.3.1 The pyrochlore and defect fluorite crystal structure

The pyrochlore crystal structure can be derived from the fluorite structure type via the defect fluorite structure [11]. Within the fluorite crystal structure AX_2 the cations (blue) form a face centered cubic package (fcc) and the anions (red) occupy all tetrahedral sites.

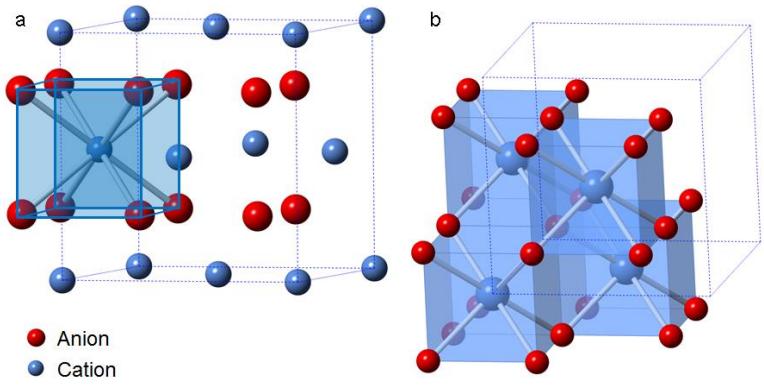

Figure 3: Scheme of (a) the fluorite crystal structure unit cell with one coordination polyhedron of a single cation; (b) the connection of the coordination polyhedra.

The cations are eightfold coordinated by anions in a cubic array (Figure 3a). These cubes are joined along edges to form the three dimensional network of the fluorite structure (Figure 3b).

Introducing a defect into the fluorite structure by randomly removing 1/8 of the oxygen leads to the defect fluorite crystal structure (Figure 4a). Due to the introduction of an anionic vacancy the mean coordination number of the cations is reduced from eight to seven. The defect fluorite crystallises in the Fm-3m space group.

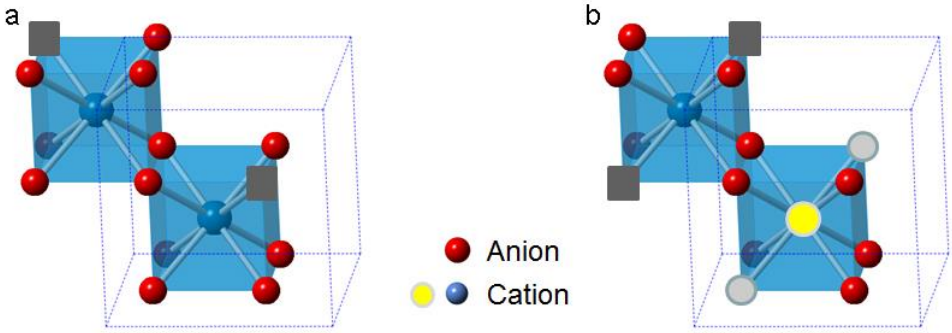

Figure 4: (a) Anionic coordination polyhedra of a defect fluorite with the cations shown in blue and the vacancies as grey squares. (b) Anionic coordination polyhedra of a pyrochlore with the cations A (yellow), B (blue) the vacancies (grey squares) and further oxygen ions at the Y position (light grey). Within the pyrochlore crystal structure the oxygen ions are displaced to a certain degree of the cubic summit as consequence of the scaleonhedron and trigonal antiprism coordination of the cations.

Removing oxygen from well-defined lattice positions leads to the presence of two distinctively different cationic positions, A (yellow) and B (blue) (Figure 4b). Moreover, the anions are no longer symmetrically equivalent. Now two distinct anionic sites and the oxygen vacancies are created. This leads to the general formula $A_2B_2X_6Y$. The A cation is eightfold coordinated by six X anions and two Y anions arranged in a scalenohedron shape. Within this array the A-Y bond length is slightly shorter than the A-X bond length [26]. The B cation is only sixfold coordinated by X anions in a trigonal antiprism due to the absence of 1/8 of the oxygen. These coordination polyhedra are joined along edges to form the pyrochlore crystal structure, just as it was the case for the defect fluorite and fluorite structure.

The pyrochlore crystallises in the Fd-3m space group. Within the Wyckoff nomenclature the A position is at the 16d site whereas the B position is located at the 16c site with the origin at the B site. The X anions at the 48f sites are fourfold coordinated by two A and two B cations, respectively. The anions at the Y position are solely coordinated by four A cations whereas the anionic vacancy is fourfold coordinated by the B cations.

In the literature, the pyrochlore formation is described to be dependent on radii of the cations and on their ratio. The pyrochlore crystal structure is formed within the ranges of r_A = 0.085 – 0.155 nm and r_B = 0.040 – 0.078 nm [27]. The pyrochlore structure is stable for a cationic ratio of r_A/r_B = 1.46 – 1.78 [26] and the range can be expanded from 1.29 up to 2.30 for high temperature and high pressure syntheses [11]. If the cations become similar in size the defect fluorite structure becomes more favourable.

Besides natural pyrochlores, e.g. $(Ca,Na)_2(Nb,Ta)_2O_6(O,OH,F)$ [28] hundreds of different pyrochlores have been synthesised [2]. The A and B sites of a pyrochlore can be occupied by trivalent and tetravalent or bivalent and pentavalent cations, respectively. The A position is often occupied by rare earth elements whereas pyrochlores with Sc, Y, Tl or Bi are also reported in the literature [11, 26]. The B position is mainly adopted by 3d, 4d, 5d transition metals or cations of the IVa group [11, 26]. The X position is always occupied by oxygen while the Y position can also be filled with fluoride ions or hydroxyl groups.

In the framework of the nuclear waste management, pyrochlores with trivalent A sites and tetravalent B sites are especially examined, because they can accommodate radionuclides with the oxidation states +III and +IV [11]. Moreover, pentavalent radionuclides e.g. Np(V) can also be taken up by the pyrochlore crystal structure [29]. Many studies have been performed on titanate based pyrochlores [30-35]. However, these pyrochlores become amorphous due to radiation damage which is unfavourable for a nuclear waste form. Within this work the ZrO_2 based pyrochlores were studied due to their high radiation tolerance. In contrast to the titanates, the zirconates undergo a phase transition from the pyrochlore to the defect fluorite as a consequence of radiation damage. This underlines why the order-disorder

transition of the pyrochlore is a subject of great interest in terms of application as a nuclear waste form.

The A and B positions of stoichiometric pyrochlores are each occupied by only one cation. As a result of the higher ordering of the pyrochlore compared to the defect fluorite structure the lattice parameter a for the pyrochlore is twice the parameter a of the defect fluorite structure [36]. The higher ordering leads to the presence of superstructure reflexes in diffraction pattern of the pyrochlore (Figure 5).

Pyrochlores with more than one cation at the A or B position will be referred in this work as non-stoichiometric pyrochlores. Lumpkin reports waste loadings of up to 35 wt% of Pu or actinides for pyrochlores [2]. Therefore, the uptake of actinides will most likely lead to a non-stoichiometric pyrochlore, resulting in a mixed occupancy by different cations at the A or B position. In order to derive a profound understanding of the actinide uptake, the transition of the pyrochlore to the defect fluorite structure is studied in detail within this work.

In the literature, the non-stoichiometric pyrochlores are mostly studied by the introduction of a third cation at the A or B site. For example Harvey et al. (2005) [36] studied the solid solution formation and structural changes in the non-stoichiometric pyrochlores by means of $(La_{1-x}Nd_x)_2Zr_2O_7$ and $Nd_2(Zr_{1-x}Ti_x)_2O_7$ systems. In the present work the non-stoichiometry was introduced by mixing Zr and Nd cations at either the A or B position. The advantage of the so introduced non-stoichiometry is that the system is kept as simple as possible without the introduction of further complications by the introduction of a third cation. The consequences of mixing cations at the A or B position for the pyrochlore crystal structure will be examined especially by diffraction pattern.

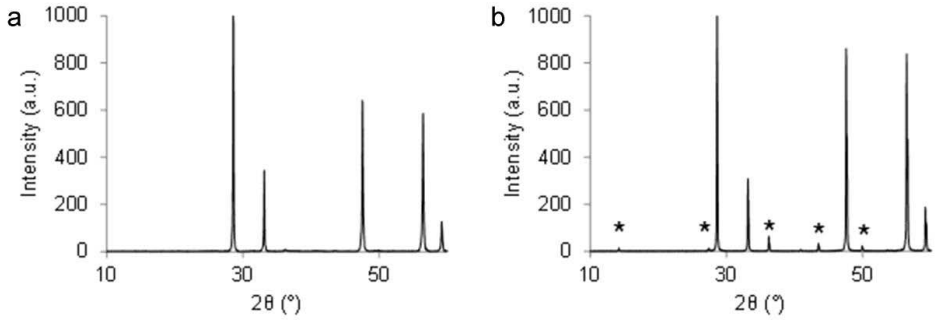

Figure 5: Typical powder XRD pattern of (a) a defect fluorite and (b) a pyrochlore ceramic. The superstructure reflexes of the pyrochlore structure are marked with asterisks.

The following techniques were applied for structural characterisation within this study:

- Powder X-ray diffraction
- Electron diffraction
- Time resolved laser fluorescence spectroscopy

Below, these techniques are briefly described.

2.3.2 Powder diffraction

X-ray Diffraction (XRD) is an analytical method to determine the long-range order of a crystalline material. From the XRD pattern the crystal structure of the material can be deduced. A qualitative and a quantitative phase analysis is possible.

The basic principle is the diffraction of an incident monochromatic X-ray at a specimen. Diffraction occurs whenever the Bragg equation is fulfilled:

$$2 d_{hkl} \sin \theta = n \lambda \tag{1}$$

With d_{hkl} the spacing between the diffracting planes, the diffraction angle 2θ, the wavelength λ of the X-rays and the diffraction order n which is a natural number. On the surface of the cones which are coaxial to the incident X-rays, the Bragg-equation is fulfilled (Figure 6a).

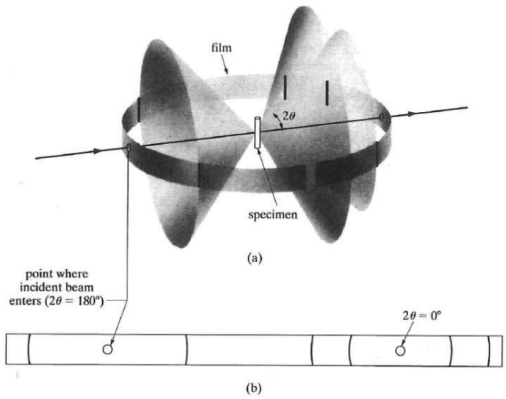

Figure 6: (a) Debye-Scherrer method of powder X-ray diffraction. (b) The flat film shows the arcs which are caused by diffracted X-rays whereas the holes correspond to the entrance and exit position of the X-ray at the film [37].

The X-rays are diffracted with the angle 2θ and the diffracted X-rays can propagate in all spatial directions with the specific diffraction angle. In the Debye-Scherrer setup, the sample was surrounded by a film to detect the diffraction pattern (Figure 6a). The diffracted X-rays propagate along the cone surface and strike the film which causes the arcs on the film (Figure 6b). The diffraction pattern showing the intensity versus the diffraction angle 2θ are generated normal to the film. The thickness of the diffraction ring on the film corresponds to the reflex intensity in the diffraction pattern. These days the film is substituted by a detector system, which comes along with a more advanced experimental setup. However the principle of the generation of powder X-ray diffraction pattern remains the same.

To identify the crystal structure from a powder diffractogram the position of the reflexes need to be identified. In a second step the pattern are compared with reference pattern to be able to identify the crystal structure. Afterwards the reflexes are indexed with the Miller indices (hkl) for a complete evaluation of the diffraction pattern. Finally structural parameters as the lattice parameter can be derived.

For a cubic crystal structure the lattice parameter *a* is defined by the following equation:

$$a = \lambda \frac{\sqrt{\left(h^2 + k^2 + l^2\right)}}{2 \sin \theta} \tag{2}$$

where h, k and l are the Miller indices.

Determination of lattice parameters, mean crystallite size and lattice distortion - The lattice parameters of all synthesised phases were determined using the Nelson-Riley method [38-39]. The values of the mean crystallite size and the lattice distortions were determined from the XRD measurements using the Hall-Williamson method [40].

The reflexes of the X-ray diffraction pattern were fitted in the measured 2θ range as a sum of Gaussian functions corresponding to each Bragg reflection. Fitting the reflexes of the XRD pattern the reflex positions 2θ, the intensity *I* and the half width *B* are received.

Within the Nelson-Riley method the lattice parameter (equation (2)) is determined for each reflex. Afterwards the value of the Nelson-Riley function is calculated according to the formula:

$$f(\theta) = \frac{1}{2}\left(\frac{\cos^2 \theta}{\sin \theta} + \frac{\cos^2 \theta}{\theta}\right) \tag{3}$$

The lattice parameter *a* of the unit cell can be extrapolated by linear regression of the lattice parameter a of each reflex versus the Nelson-Riley function value.
The main fit parameters of the Bragg lines were the line positions (2*θ*), which depend on the lattice parameter, and the integral half-width of reflections (*B*), which allow the estimation of the mean crystallite size (*L*) and lattice distortions ($\langle \varepsilon^2 \rangle^{0.5}$) with the Hall-Williamson method.

$$\frac{\beta \cdot \cos\theta}{\lambda} = \frac{1}{L} + 4\left\langle \varepsilon^2 \right\rangle^{0.5} \frac{\sin\theta}{\lambda} \tag{4}$$

with the Bragg angle of diffraction *θ* and the wavelength λ of the incident X-rays. The reflex half-width B is defined as the integral surface of the reflex profile divided by its height, whereas the parameter β includes a correction of the profile due to the geometry of the path of rays. In a Hall-Williamson plot the lattice distortion can be derived from the slope and the crystallite size from the intersection of the line with the ordinate

2.3.3 Electron diffraction – single crystal diffraction

A transmission electron microscope (TEM) allows a detailed, local characterisation of the structure of an electron transparent sample. In addition to an image in real space the observation of the corresponding focal plane in reciprocal space is possible via TEM. Thus a real image at very high resolution and the corresponding structural information can be combined.
The scattering of neutrons and electrons obey the same geometric rules which are valid for diffracted X-rays [41]. Diffraction at a three-dimensional crystal can therefore only be observed if the Bragg equation is fulfilled in all three dimensions. The Ewalds' sphere is a more descriptive way to depict when the Bragg equation is fulfilled for all three dimensions (Figure 7). This sphere translates the Bragg equation in a geometric way into reciprocal space.
The radius of the Ewald sphere corresponds to the reciprocal wavelength λ. Therefore the Ewald sphere is much larger for electron diffraction than for X-ray diffraction. The wave vector CO or k_I of the incident beam shows that the Ewald sphere needs to pass through the origin of the reciprocal lattice O (Figure 7). The vector k_D represents any radius vector inside the Ewald sphere. All diffraction points which will lie on the Ewald sphere will be observed. For every point or lattice plane where diffraction occurs a diffraction point exists in the reciprocal space, because the reciprocal space gives a complete image of the scattering phenomena of the real crystal. How the real space and the reciprocal space correlate is shown in Figure 8.

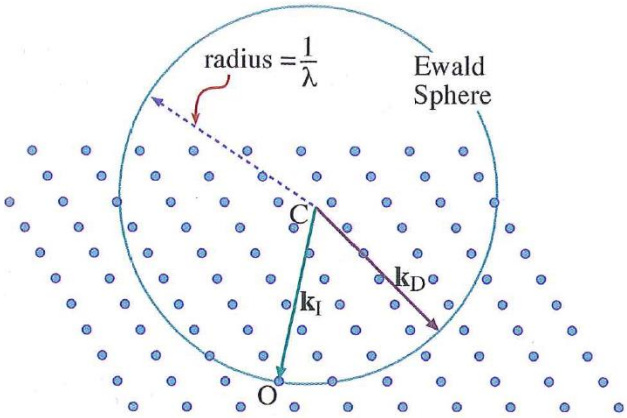

Figure 7: Ewald sphere with the radius 1/λ and the origin O of the reciprocal lattice [42].

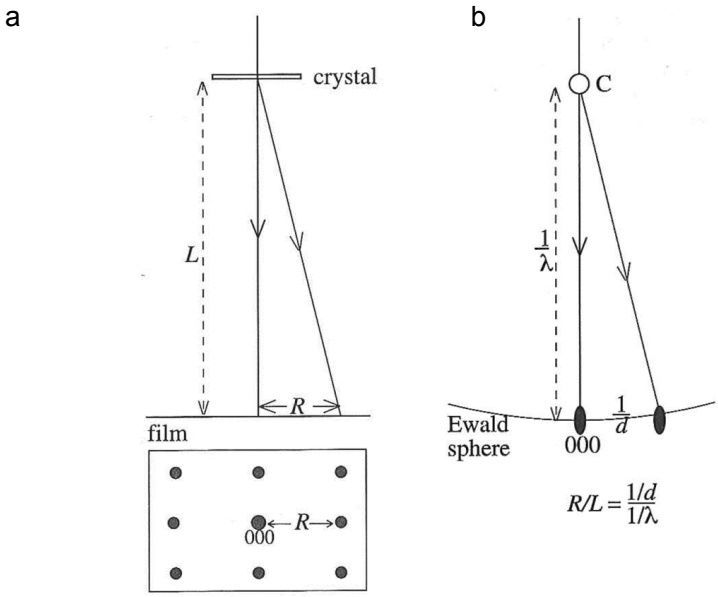

Figure 8: (a) Correlation of the real lattice and (b) the reciprocal lattice for electron diffraction [43].

The distances between the diffracted points in reciprocal space are interrelated to the reciprocal spacing between the lattice planes *d* of the real crystal. Therefore the crystal lattice defines where the diffraction points occur within the diffraction pattern. Each scattered beam can be described as a wave of a specific phase and amplitude which is expressed by the structure factor *F(hkl)*. The structure factor sums up all diffracted waves of one sort of atoms and is defined as follows:

$$F(hkl) = \sum_j f_j \cdot e^{-2\pi \cdot i\left(x_j \cdot h + y_j \cdot k + z_j \cdot l\right)} \tag{5}$$

with the atomic scattering factor f_j, the imaginary number *i* and the coordinates of the atom *j* inside the unit cell x_j, y_j and z_j. The absolute value of the structure factor $|F(hkl)|$ is called structure amplitude and defines the amplitude of the diffracted wave. The intensity of the diffracted beam equals the square of the structure amplitude $|F(hkl)|^2$.

The structure of the investigated crystal can therefore directly be derived from the diffraction pattern collected by TEM. In contrast to powder X-ray diffraction, where the bulk structure is studied, electron diffraction pattern give access to the structure of individual grains. This is of special interest to study order-disorder phenomena just as the transition from a stoichiometric pyrochlore to a defect fluorite. The structural change may start at a certain point of the crystal or the formation of clusters might also be conceivable.

Within the imaging plane of a TEM one has to distinguish a bright field (BF) and dark field (DF) image (Figure 9a and b).

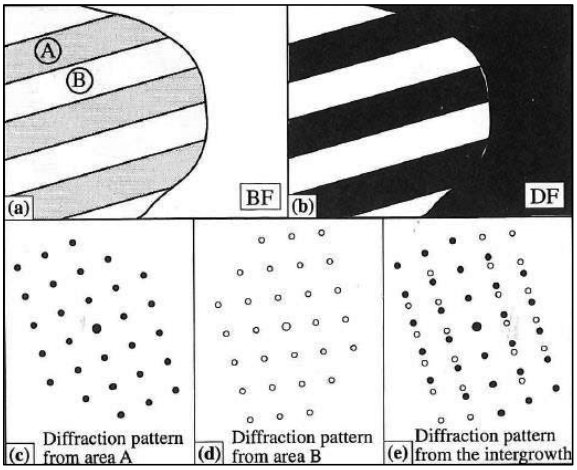

Figure 9: (a) Bright field and (b) dark field image of a two phase material. The electronic diffraction pattern are shown for (c) phase A, (d) phase B and (e) for the intergrowth region. The DF image is generated by a diffraction point of phase B [43].

Both modes are imaging methods and the diffraction pattern are obtained by changing to the focal plane.

Within a BF image singly the undiffracted beam passes through the apertures to the image plane. Therefore a crystalline phase like A in Figure 9a which scatters the beam stronger than the phase B appears darker in the obtained image. To receive the diffraction pattern one has to switch to the focal plane. Usually a further aperture is inserted to select an area of the specimen of which the diffraction pattern are obtained Figure 9c and d. This method is called selected-area diffraction (SAD). By switching back to the image plane a DF image is generated. Figure 9b shows the DF image of the crystalline phase B and therefore all areas of this phase are bright in the image. Changing from a BF image to the diffraction pattern and back to a DF image is useful to probe if the specimen is a single phase material. Within this work SAD pattern were collected and the specimens were probed for the presence of second phases by characterisation of the sample with BF and DF images.

2.3.4 Time resolved laser fluorescence spectroscopy / luminescence spectroscopy

Time resolved laser fluorescence spectroscopy (TRLFS) is a highly sensitive technique to probe the local environment of f-elements e.g. Eu or Cm. In general an electron absorbs light and populates an excited energy level. Within the relaxation process light is emitted and can be detected. TRLFS can be applied to solids, suspensions and solutions. Within this work the UV and direct excitation fluorescence spectroscopy of Cm and Eu were probed in $La_2Zr_2O_7$ samples with the defect fluorite and pyrochlore crystal structure.

Curium fluorescence spectroscopy - For the trivalent curium ion many ff-transitions exist. The selection principle of Laporte prohibits electric dipole transitions for transitions with equal parity. In the presence of a ligand this selection principle can be circumvented. The presence of states with opposite parity is accompanied by a symmetry distortion and is called enforced electric dipole transition.

With UV excitation at 396.6 nm the Cm ion is excited with a laser into a higher energy level and de-excites into the A-state by non-radiative relaxation to populate the $^6D_{7/2}$ state (Figure 10).

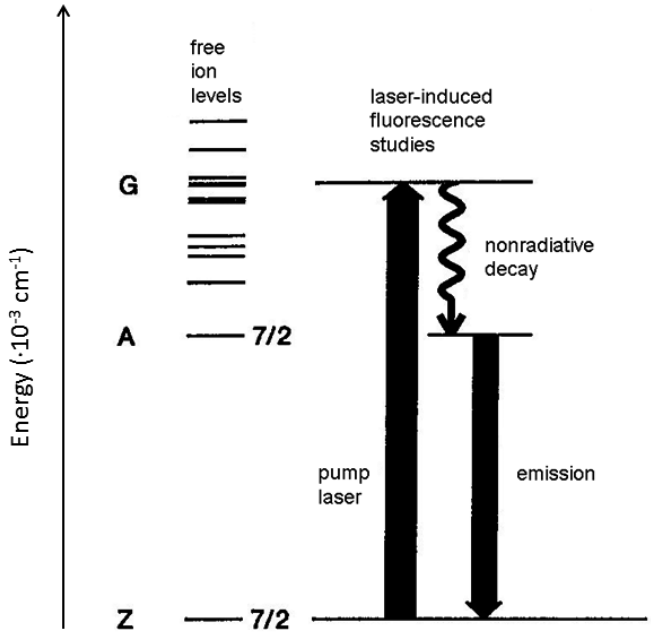

Figure 10: Energy levels of a free Cm ion (left) and the excitation and relaxation processes (right). The excitation is laser-induced and within the UV excitation the first relaxation step is a non-radiative decay from the G to the A state which is followed by relaxation to the ground state via fluorescence emission. Adapted from Beitz [44].

Due to the large energy difference of the A and Z state the relaxation to the ground state can also occur by fluorescence (Figure 10). The four ground states of Cm are degenerate in the gas phase. The presence of a ligand causes a change in the crystal field splitting. This leads to a change of the relaxation energy which is expressed as a shift of the band in the emission spectrum. Depending on the strength of interactions with the first coordination sphere of the Cm ion the fluorescence signal can show a splitting of the ground state. The interaction of the Cm(III) ion with a strong crystal field causes an energy decrease of the $^6D_{7/2}$ state which results in a bathochromic shift compared to the Cm aquo ion in the emission spectra.

Determination of lifetime – At the time *t*, *N(t)* atoms occupy an excited state. The relaxation to the ground state is a statistical process and can be expressed by the Boltzmann distribution:

$$N(t) = N_0 \cdot e^{-t/\tau} \tag{6}$$

with

τ lifetime of the excited state

$N(t)$ occupancy of the N^{th} state at the time t

N_0 occupancy of the ground state.

In order to determine the lifetime of a species, the delay time until the camera opens is constantly increased whereas the gate width is kept constant to collect the entire fluorescence signal. The integration of the collected fluorescence signal on a logarithmic scale is plotted against time. The lifetime is determined from the reciprocal slope of this plot.
Water is known to quench the fluorescence signal due to harmonic oscillations as concurring relaxation process to the fluorescence. Horrocks [45] and Kimura [46] formed equations which express the correlation of the amount of water molecules and the fluorescence lifetime for Eu and Cm, respectively.

Europium fluorescence spectroscopy – In contrast to Cm, Eu has $^7F_{0\text{-}6}$ ground states which are non-degenerate (Figure 11). Each level is split into (2*J*+1) sublevels. Mostly the emission of fluorescence is observed for the $^5D_0 \rightarrow {}^7F_J$ transitions.
Due to its non-degeneracy (2*J*+1=2·0+1=1), the $^7F_0$ transition gives the information on the number of present Eu specie by a single band for every Eu species in the UV emission spectrum. The degree of degeneracy of the other ground state levels is dependent on the symmetry of the ligand field. A low symmetry of the surrounding atoms leads to non-degenerate splitting of the subniveaus which is observed by a high degree of band splitting in the emission spectrum. The $^5D_0 \rightarrow {}^7F_{0,1,2}$ transitions allow the attribution of the splitting to symmetry classes. With the help of the Görller-Walrand and Binnemans table the point group of the Eu(III) environment can be identified. However, isocentric point groups such as D_{3d} at the A site of the pyrochlore are not listed in this table.

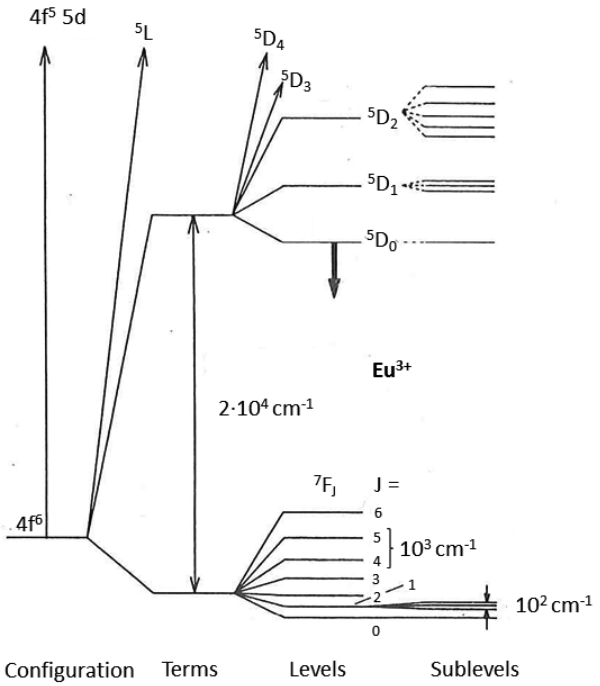

Figure 11: Section of the Eu(III) energy scheme. The downwards pointing arrow at the $^5D_0$ energy level indicates the relaxation of the excited Eu(III) to the ^7F_J levels by a fluorescence signal. The splitting of the $^7F_1$ level shows the non-degenerate sublevels. Adapted from Bünzli and Choppin [47].

Besides the UV excitation at 394 nm, the direct excitation was used to probe the local environment of the different Eu species separately. Therefore, the energy of the excitation laser was adjusted to the wavelength of each species which was identified by the UV excitation measurement.

Lifetime measurements by direct excitation allowed a determination of the lifetime for the corresponding species.

2.4. Properties of ZrO_2 - Nd_2O_3 ceramics as potential nuclear waste forms

Relevant properties of nuclear waste forms are

- Radiation tolerance
- Chemical stability
- Radionuclide uptake

Although it is generally well known that pyrochlores meet most of these criteria, a detailed process understanding is still missing. This study has focused on the chemical stability in terms of radionuclide uptake and dissolution kinetics.

2.4.1 Structural uptake of Pu

Pu-239 has a half-life of about 24110 years. Therefore, the long-term radiotoxicity of high level nuclear waste could be reduced significantly by the separation and embedding of Pu-239 in a tailor-made matrix. Moreover, the UK holds about 123 tons of civil plutonium which is already separated [9]. The embedding of the plutonium in a ceramic matrix could be a suitable option to ensure a safe disposal.

To investigate the ability of pyrochlore to serve as host material for actinides it is important to synthesise materials where the actinides are a major component. Icenhower et al. used titanate based pyrochlores for their dissolution experiments, containing about 12 wt% PuO_2 [48]. Nästren et al. [24] synthesised $Nd_{1.8}An_{0.2}Zr_2O_7$ (An = Pu, Am, Np, Th, U) pyrochlores by a liquid infiltration method into porous beads, whereas Gregg et al. [49] used a modified alkoxide nitrate route. A hydroxide coprecipitation route to form Pu-pyrochlores has so far not been reported in the literature.

There are specific challenges concerning the aqueous chemistry of Pu due to the high number of possible oxidation states and the possible formation of polymers. It is known from the literature that Pu(IV) tends to form a Pu polymer under hydrolysis [50-52]. This colloidal Pu has a green colour [53]. The probability of the plutonium polymer formation is described to increase with increasing plutonium concentration, increasing temperature and increasing pH. However, it is not fully understood how the plutonium polymer is formed [51]. Once the polymer has formed it is hardly possible to depolymerise this colloid. As a consequence the formation of a separate Pu-phase becomes likely. Even the dilution of an acidic Pu solution e.g. with water which results in a solution with a pH below two, can cause the polymer formation as the solution may have too high pH values during the homogenisation [52].

A wet-chemical coprecipitation route was adapted with the aim of a homogeneous uptake of Pu by the pyrochlore crystal structure. Precautions as acidification and direct processing were taken to avoid a plutonium polymer formation.

2.4.2 Theoretical background: Dissolution kinetics

Dissolution and recrystallization are processes taking place whenever a solid and an aqueous solution get in contact with each other which are not in thermodynamic equilibrium. These processes occur in nature at many different scales, e.g. weathering and erosion, transport and deposition and mineral dissolution and recrystallization, just to name a few. In many cases the reaction pathway plays a key role, because these processes are kinetically controlled.

Within nuclear waste management the waste form is often considered as engineered barrier. Therefore thermodynamic aspects such as the stable phase or the possible formation of secondary phases become relevant. Besides the thermodynamic aspects, kinetic questions concerning the corrosion, the processes controlling the elemental release or leaching arise. The simplest assumption would be a complete dissolution as consequence of waste form - water interaction which would make the waste form itself irrelevant.

In realistic scenarios dissolution and possible reprecipitation processes become relevant. To overcome the phenomenological descriptions of dissolution tests, the transition state theory (TST) was introduced [54-55]. The TST rate equation is still widely used although it is mainly based on macroscopic observation [56-57]. With the help of this model and dissolution experiments predictions for several scenarios can be made. In the end a mechanistic understanding how the dissolution processes take place at an atomic scale is needed to derive a refined model of dissolution kinetics.

The formulation of a dissolution model is a challenging task which requires experiments at the macroscopic and microscopic scale which are in the best case combined with computer based simulations. However, a first approach within the nuclear waste management is the derivation of a simplified source term for radionuclide release under repository relevant conditions to predict the stability of potential waste forms.

To understand dissolution kinetics, there are several aspects which need to be looked at, such as the dissolution mechanism, the reactive surface area, the effect of temperature and pH and the chemistry of the dissolving solutions, just to mention some of them. A separate investigation of these parameters will allow the identification of the contribution of each parameter to the overall dissolution rate. The following section is devoted to these parameters.

It is still common practice to determine an overall dissolution rate with a macroscopic approach without considering a differentiation of the different steps or different dissolution mechanisms. In fact the dissolution of minerals or oxides consists of a sequence of several steps: (1) the transport and (2) adsorption of the leachant to the surface, (3) the formation of the activated complex and (4) its detachment of the surface and (5) the transport in solution

away from the surface [54]. The first process is controlled by diffusion whereas the processes (2) to (4) are surface controlled. The last step can either be diffusion or surface controlled. The rate determining step is given by the slowest reaction for sequentially occurring reactions and by the fastest reaction for parallel occurring reactions [58].

The solid/water interface or rather the solid surface needs to be studied in detail as this is the site where the dissolution takes place. Crystalline solids e.g. minerals do not possess a perfect surface but exhibits different features. Classical publications by Kossel (1927) [59] and Stranski (1927) [60] introduced a simplified model of monoatomic layers to describe the solid surfaces (Figure 12). Screw dislocations were added into this model by Frank (1949) [61].

Within their model the surface is built from square units and there are seven different sites: (1) corresponds to a vacancy at a terrace and (2) is a vacancy at a step. Position (3) shows an adatom at a terrace and (4) an adatom at a step. (5) depictes an edge dislocation whereas (6) shows a screw dislocation and (7) corresponds to a kink site. An adatom at a terrace (3) can easily be dissolved as it is only attached to the surface at one site. However, the removal of an adatom is only of minor contribution to the overall dissolution process, because its removal leads to a flat terrace which does not initiate a subsequent dissolution step. In contrast a kink site plays an important role in dissolution processes. Kink sites are units which have three neighbours at the solid surface whereas the remaining three sites are directly accessible. If a kink site is added in crystal growth theory or removed due to dissolution, a new kink site is created. Due to their propagation these sites play a key role in crystal growth or dissolution processes as they allow these to continuously act on the solid surface.

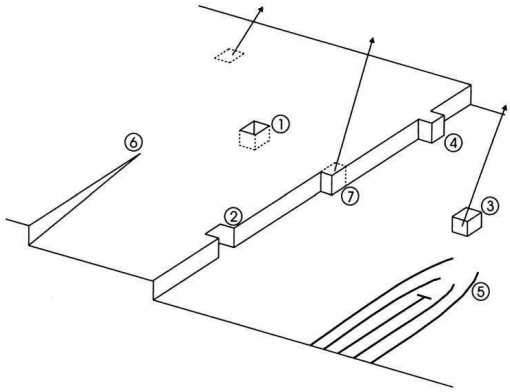

Figure 12: Simplified scheme of the different sites at a solid surface: (1) vacancies within a terrace or (2) a step, (3) adatoms at a terrace or (4) step, (5) edge dislocations or (6) screw dislocations and (7) kink sites. Taken from Lasaga [54].

The formation of a vacancy within a terrace which is also referred to as etch pit (1) (Figure 12) is less favoured. There is only one site directly accessible and a detachment of the atom from the five remaining sites, representing the bonds between atoms, is necessary to create a vacancy. Frank extended the Kossel and Stranski model with the introduction of edge and screw dislocations [61], where the dissolution can also take place. In general the crystal growth or dissolution propagates stepwise within an atomic layer through the crystal. Which of the above described processes initiates the stepwise growth or dissolution is dependent on the nanotopography and the deviation from equilibrium.

The macroscopic scale - To describe surface controlled crystal growth or dissolution the TST rate equation is widely used [55]:

$$Rate = k_0 \cdot A_{reactive} \cdot e^{-E_a/RT} \cdot a_{H^+}^{n_{H^+}} \cdot \Pi a_i^{n_i} \cdot f(\Delta G_r) \qquad (7)$$

with

k_0	rate constant
$A_{reactive}$	reactive surface area
E_a	apparent activation energy
$a_{H^+}^{n_{H^+}}$	hydronium ion activity in solution with the reaction order n
Πa_i^{ni}	activity for all ions in solution
$f(\Delta G_r)$	deviation from thermodynamic equilibrium.

This rate equation is a mathematical expression that combines the most important factors of influence on the dissolution rate. The main advantage of this rate equation is the possibility to separate all variables. Therefore, the influence of each factor mentioned in the rate equation such as temperature or pH can be studied individually. In the end a prediction of the rate under various conditions is possible with the rate equation. In the following section the main variables of interest for this thesis from the rate equation will be explained in detail.

Surface controlled dissolution as example of the transition state theory - The dependence of the surface controlled dissolution on the bulk free-energy change can be derived from the transition state theory (TST). Within the TST the concentration of the activated complex and the forward dissolution rate R_+ are set to be proportional for far from equilibrium conditions.

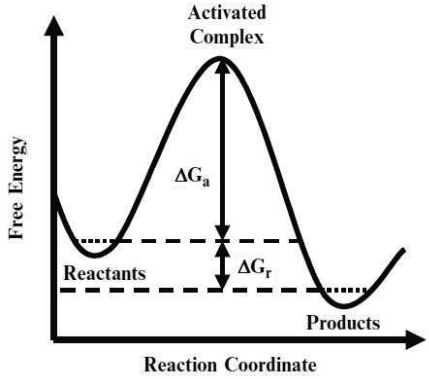

Figure 13: Schematic illustration of the transition state theory. In the case of dissolution the reactants form with the aqueous species a precursor complex. The precursor complex is converted into the activated complex which decomposes into the products, e.g. the dissolved ion. Taken from Kubicki [62].

The dissolution reaction is described by several reactions or steps which are occurring successively [58]:

Reactants ± aqueous species precursor complex activated complex → products

This reaction is visualised in Figure 13 with the activated complex as transition state prior to a decomposition into the products. According to the chemical equation the activated complex concentration which is not directly accessible can be expressed via the precursor species. These two species do not differ in their chemical formula, but the activated complex is instable due to its higher energy.

As a result of the law of mass action the concentration of the activated complex is a constant fraction of the precursor complex:

$$Rate_{+} = k_{+} X_{P} \tag{8}$$

with

k_+ rate constant that takes the ratio of the precursor complex and the activated complex into account

X_P mole fraction at the surface for the precursor complex.

Oelkers (2001) [58] describes the application of TST to the dissolution of a multioxide under acidic conditions. Under the assumption that the precursor complex is in equilibrium with the original solid, its concentration can also be expressed via the composition of the aqueous solution, and the law of mass action for its formation. A multioxide may be described by the following expression:

$$\sum_{i=1}^{m} \left(M_{i_{n_i}} \right) O_{\sum_{i=1}^{m} \left(\frac{n_i z_i}{2} \right)} \tag{9}$$

with

M_i metal atom

n_i stoichiometric number of the metal atom M_i normalised to the formation of a precursor complex

z_i valence of the metal atom.

The substitution of the metal atom by protons is given by:

$$\sum_{i=1}^{m} \left(M_{i_{n_i}} \right) O_{\sum_{i=1}^{m} \left(\frac{n_i z_i}{2} \right)} + n_k z_k H^+ \leftrightarrow n_k M_k^{z_k +} + \sum_{i=1, i \neq k}^{m} \left(M_{i_{n_i}} \right) H_{n_k z_k} O_{\sum_{i=1}^{m} \left(\frac{n_i z_i}{2} \right)} \tag{10}$$

The formation of the protonated oxide due to the elimination of M_k can be expressed as follows:

$$\sum_{i=1, i \neq k}^{m} \left(M_{i_{n_i}} \right) H_{n_k z_k} O_{\sum_{i=1}^{m} \left(\frac{n_i z_i}{2} \right)} \tag{11}$$

The law of mass action for the precursor is given by:

$$K_k = \left(\frac{a_{M_k z_{k+}}}{a_{H^+}^{z_k}} \right)^{n_k} \frac{X_P}{X_M} \tag{12}$$

with

a_i	activity of the corresponding species
X_P	mole fraction of the protonated species at the surface (precursor complex)
X_M	mole fraction of the primary surface
K_k	equilibrium constant for the protonation of the metal species at the mineral surface.

Moreover, the surface is either protonated $\left(\equiv \mathrm{SOH}_2^+\right)$ or the primary species $(\equiv \mathrm{SOH})$ is present. This is mathematically expressed via:

$$X_P + X_M = 1 \tag{13}$$

This can be rewritten as:

$$X_P = \frac{K_k \left(\frac{a_{H^+}^{z_k}}{a_{M_k z_{k+}}} \right)^{n_k}}{\left[1 + K_k \left(\frac{a_{H^+}^{z_k}}{a_{M_k z_{k+}}} \right)^{n_k} \right]} \tag{14}$$

For the numerator >> 1, the metal ion is removed from the mineral surface. This can lead to the formation of leached layers. If the pH decreases, the ratio of the activities increases. This corresponds with the observation of leached layer formation in many cases with an acidic pH regime. If the dissolution reaction is described by the first until the j^{th} protonation reaction of the metal species at the surface which are all thermodynamically independent, the mole fraction of the precursor complex can be written as:

$$X_P = \prod_{i=1}^{j} \frac{K_k \left(\frac{a_{H^+}^{z_k}}{a_{M_k z_{k+}}} \right)^{n_k}}{\left[1 + K_k \left(\frac{a_{H^+}^{z_k}}{a_{M_k z_{k+}}} \right)^{n_k} \right]} \tag{15}$$

A combination with equation (8) leads to the following expression for the forward dissolution rate:

$$Rate_{+} = k_{+} \prod_{i=1}^{j} \frac{K_k \left(\frac{a_{H^+}^{z_k}}{a_{M_k z_{k+}}} \right)^{n_k}}{\left[1 + K_k \left(\frac{a_{H^+}^{z_k}}{a_{M_k z_{k+}}} \right)^{n_k} \right]} \tag{16}$$

This is an attempt to describe the dissolution rate as a function of the released metal cations into solution. For multioxides like pyrochlores the dissolution is much more complex than for single oxides, because there are two different cationic species present which results in a variety of possible reaction pathways to explain how the dissolution occurs [58].

PH dependence of the dissolution rate - The presence of protons or hydroxyl groups on the surface of minerals is thought to fasten dissolution mechanisms. This leads to the rate equation:

$$Rate = k_H a_{H^+}^n + k_{OH} a_{OH^-}^m \tag{17}$$

with

a activity of the corresponding species

k rate constants of the dissolution reactions which are accelerated by the protons or hydroxyl groups

n, m order of corresponding reaction.

To involve the dissolution at neutral conditions a term for k_{H_2O} is added in some cases. The reaction orders are different for different minerals. According to Stumm and Furrer [63] an oxide surface is polarized as a consequence of H^+ ad- or desorption due to the polarisation of the oxygen-metal bond. This might ease or hinder the breaking of the bond.
The complexation of an oxide is expressed via the following reaction mechanisms:

$$\equiv \mathrm{SOH}_2^+ \underset{+H^+}{\overset{1}{\rightleftharpoons}} \equiv \mathrm{SOH} \underset{2}{\overset{+OH^-, -H_2O}{\rightleftharpoons}} \equiv \mathrm{SO}^- \tag{18}$$

where ≡SO denotes the surface complex, here with a negative, neutral and positive charge.

Taking ≡SOH as a starting point, reaction 1 occurs in the presence of protons. If the dissolution takes place in the presence of hydroxyl groups the separation of water leads to a negatively charge surface according to reaction 2. From the reaction equation (18) the following dissolution rate equation was derived [64]:

$$Rate = k_H \left[\equiv SOH_2^+ \right]^{q_1} + k_{OH} \left[\equiv SO^- \right]^{q_2} \tag{19}$$

q_1 and q_2 are constants which are different for the different oxides or minerals and often different than unity. In some articles q_1 is correlated with the oxidation state of the metal, because this corresponds with the number of protons which are adsorbed by the metal to form the protonated surface complex [63, 65]. This is schematically shown by the proton accelerated dissolution of a metal oxide in Figure 14:

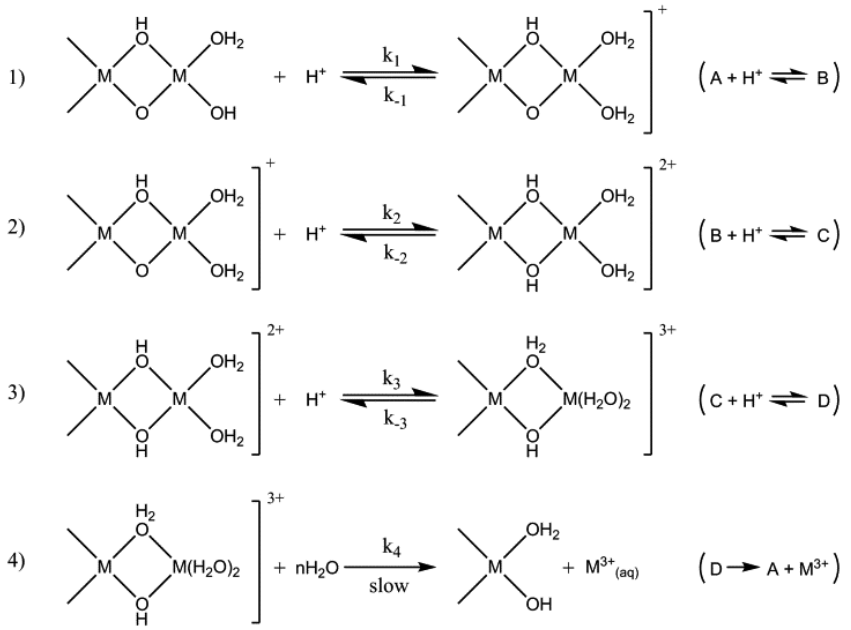

Figure 14: Schematic diagram about the proton accelerated dissolution of a metal oxide M_2O_3. Adapted from Furrer and Stumm [63].

Within three steps the oxide or hydroxide groups around the metal at the surface are protonated and three OH_2^+ groups surround this metal centre (reactions 1-3, Figure 14). In an adjacent reaction the bonds between the metal ion and the H_2O^+ groups break resulting in the release of a threefold positively charged cation M^{3+} into the solution (reaction 4). This cationic release exposes a new metal cation to the surface and the dissolution proceeds by a repetition of the above mentioned mechanisms at the new site. At the pH_{pzc} point of zero charge the surface charges are balanced. For most minerals or oxides the lowest dissolution rate is observed at the pH corresponding to the point of zero charge, because no surface complexation that enhances the dissolution is present. For $pH \neq pH_{pzc}$ usually a higher dissolution rate is observed. The change of the rate dependence on the pH is shown exemplarily for corundum in Figure 15.

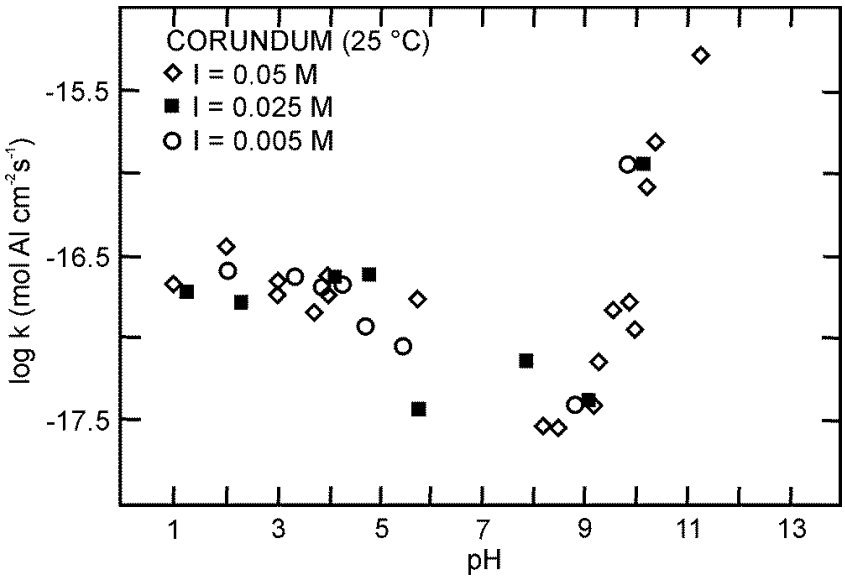

Figure 15: Steady state rate k of corundum as a function of pH for different ionic strengths I. Adapted from Carroll-Webb and Walther [66].

It becomes also visible that the dependence of the rate on the pH is different for the lower and higher pH region or rather below and above the point of zero charge.

Temperature dependence - The apparent activation energy E_a' links the rate and the temperature according to Arrhenius' law:

$$Rate = A \cdot e^{-E_A'/RT} \tag{20}$$

with

A	pre-exponential factor
R	gas constant
T	temperature in Kelvin.

The solution chemistry might also have an impact on the apparent activation energy. In this case the Arrhenius approach is expressed via [64]:

$$Rate_H(T) = k_H(T_0) \cdot e^{-E_A/RT} \tag{21}$$

with the rate constant for proton promoted dissolution $Rate_H$ and the temperature independent pre-exponential factor $k_H(T_0)$.

The dependence of the activation energy on two parameters is in conflict with the classical rate equation after Lasaga, which proposes all parameters to be independent of each other.

Equation (20) gives the pH dependent apparent activation energy E_a' from an ln(Rate) vs $1/T$ plot. This activation energy is only valid for the pH at which the temperature variations were conducted. From equation (21) an $\ln(k_H)$ vs $1/T$ plot is usually derived and the apparent activation energy is valid for any pH. In the case of n of equation (17) being temperature independent E_a' equals E_a. However, the impact of this additional factor is discussed to be of minor importance in the literature and is thus commonly ignored [64].

In general dissolution reactions can either be diffusion controlled or surface controlled. The diffusion controlled dissolution rate changes due to variations of the flow rate, because a high concentration gradient from the surface into the solution exists. Surface controlled dissolution rates directly correspond to the dissolution of the solid at the solid - water interface. One possibility to differentiate between these two mechanisms is their activation energy, because the apparent activation energy is dependent on the rate-controlling step. Diffusion controlled processes exhibit a much lower activation energy than surface controlled processes. Commonly activation energies below 20 kJ/mol are assigned to diffusion controlled reactions [54]. According to Brantley [64] activation energies for purely surface controlled dissolution should be >60 kJ/mol. Common values for the apparent activation energy for many different minerals are in the range of 42 – 84 kJ/mol [54].

Overall a change in temperature can have a very strong impact on the dissolution rate because of the exponential relation. Therefore within a broad temperature range a change of the dissolution mechanism may be observed. In this case Equations (20) and (21) are more accurately expressed by a summation of two Arrhenius terms:

$$Rate = A_1 e^{-E_1/RT} + A_2 e^{-E_2/RT} \tag{22}$$

The deviation from equilibrium - In aqueous solutions the deviation from equilibrium can be described by:

$$\Delta G_r = RT \ln\left(\frac{\Pi a_i^{v_i}}{K_{sp}}\right) \tag{23}$$

a_i species in solution
v_i mol of the element i
K_{sp} solubility product

with the supersaturation index Ω:

$$\Omega = \frac{\Pi a_i^{v_i}}{K_{sp}} \tag{24}$$

When Ω equals one the system is in thermodynamic equilibrium. For a supersaturation index $\Omega < 1$ dissolution will propagate whereas a supersaturation index $\Omega > 1$ correlates to crystal growth. Figure 16 shows the dependence of the dissolution rate on ΔG_r for magnesite. Approaching equilibrium the history of the sample plays an important role. This can be seen in the different shapes of the curves A and B in Figure 16.

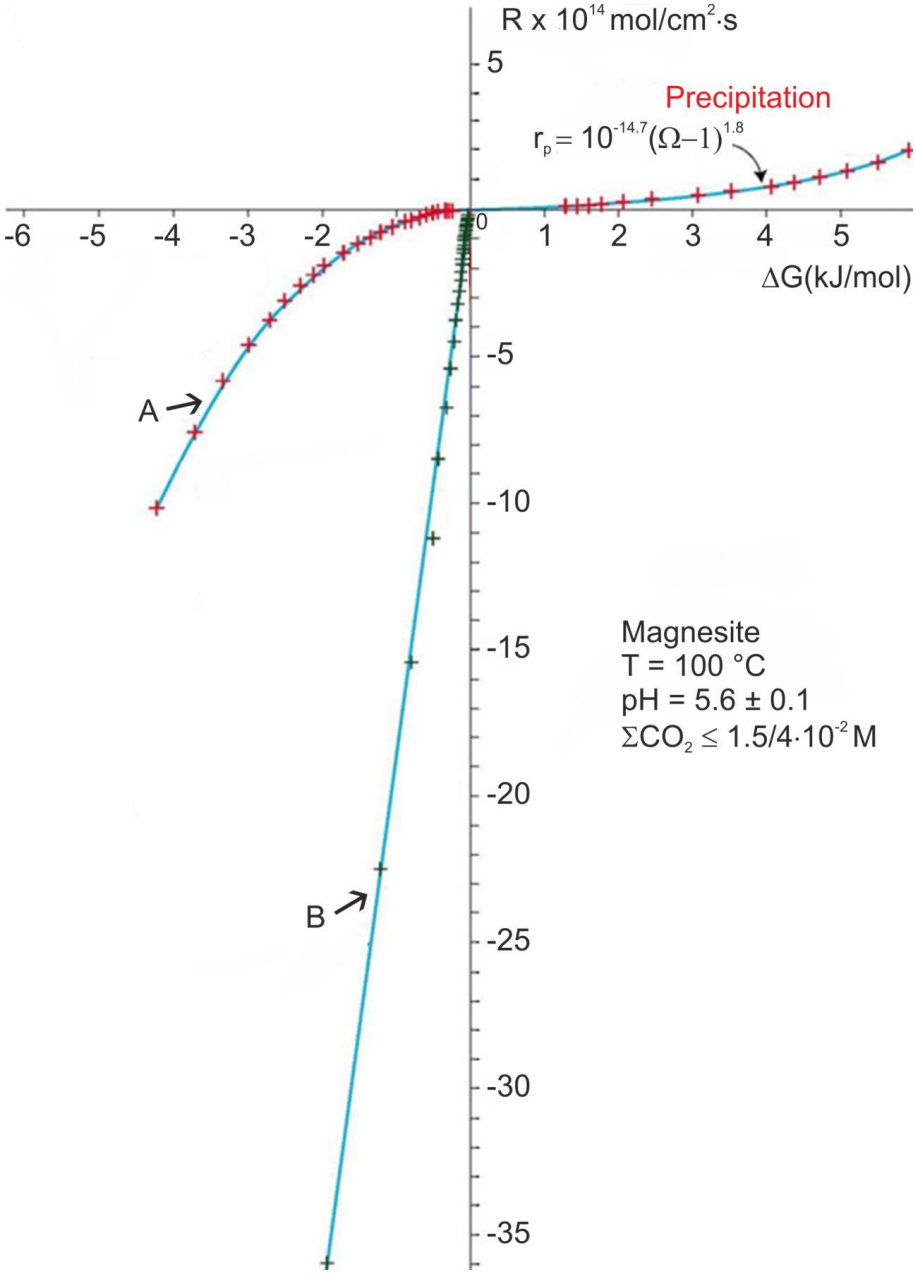

Figure 16: Dissolution rate and growth rate of magnesite close to equilibrium. Curve A corresponds to dissolution initiated by disrupting equilibrium whereas curve B shows dissolution which was initiated far from equilibrium. Adapted from Schott et al. [67].

Approaching $\Delta G_r = 0$ from far from equilibrium conditions (curve B) implies a different surface reactivity due to the existence of etch pits whereas a disruption of equilibrium conditions (curve A) leads to lower dissolution rates because of the absence of etch pits. Far from equilibrium, the dissolution rate becomes independent of ΔG_r. This region is called the dissolution plateau. To exclude any effect of ΔG_r on the dissolution rate dissolution experiments are usually carried out in the region of the dissolution plateau. If a change of the conditions from far from equilibrium to close to equilibrium occurs this is often accompanied by a change from surface to diffusion controlled dissolution. A change of the dissolution mechanism may be indicated by the critical saturation index. Below this index the predominant processes are the formation and propagation of etch pits at dislocations which is assigned to processes far from equilibrium. Above the critical saturation index the dissolution propagates especially at high energy surface sites such as corners or edges which indicate dissolution close to equilibrium. The change of the dissolution mechanism might be accounted for a change in the slope of the rate function dependent on ΔG_r approaching the equilibrium.

For example the dissolution of magnesite far from equilibrium is dominated by the nucleation of etch pits at dislocation outcrops. These are the starting points for the step formation by which the dissolution proceeds at the surface. Close to equilibrium the dissolution only proceeds at already present edges and corners and the nucleation of new sites stops if no etch pits were generated earlier [67]. Therefore close to equilibrium the deviation from the thermodynamic equilibrium is dependent on the accessible reactive sites. In turn the reactive sites are dependent on the history of the sample, e.g. a sample that was already inserted in a dissolution experiment might show a high number of etch pits. The dissolution rate of such a sample might differ from a sample of the same chemical composition that was e.g. prepared in a different way because the samples might differ in their type and number of reactive sites. Additionally the reactive sites such as etch pits, grain boundaries and edges can change when dissolution proceeds. This gives rise to different rates for similar samples. Studying dissolution kinetics close to equilibrium has the disadvantage that a comparison of experimentally derived data to study e.g. the pH dependence for a mineral would hardly be possible as the ΔG_r would always need to be adjusted to the same value.

The reactive surface area – Within the rate equation the reactive surface area is listed as one parameter in order to describe the proportion of the surface which is actually involved in the dissolution process [54]. However, for practical reasons elemental release rates are generally normalized either by geometric or the BET surface area [68], representing the total surface area.

The specific surface area can be measured either with krypton or nitrogen as adsorption gas for BET measurements. For specific surface areas of silicates Brantley and Mellott [68] suggest an insufficient quality for surface areas below 0.1 m^2/g but an outstanding quality for specific surface areas above 0.4 m^2/g with an error of 5 %. The geometric surface area (A_{geo}) and the specific surface area determined by BET (A_{ads}) are related to each other via the roughness λ of the surface [69]:

$$\lambda = A_{ads} / A_{geo} \tag{25}$$

Due to different reactivities at the surface in many cases the reactive surface area may differ from the directly accessible specific surface area. For example grain boundaries exhibit a higher reactivity than the grains themselves as consequence of defect accumulation at the grain boundaries.

For highly porous powders, as used within this work, a normalisation to the specific BET area is more appropriate than a normalisation to the geometric surface area, because the pore surfaces participate in the dissolution processes and are taken into account by BET.

For feldspars, Holdren and Speyer [70] figured out that the reactive sites do not scale with the grain size. This finding illustrates the complexity of the reactive surface area for dissolution experiments. A further challenge can be the change of the reactive surface area due to the dissolution experiment, i.e. if the dissolution rate should be normalised to the initial or the final surface area. In case of a surface increase during the experiment but a constant dissolution rate it seems to be plausible to normalise to the initial surface area, because the increase of the surface does not correlate with a reactivity increase in such cases.

Figure 17 gives a further example that the specific surface area does not necessarily correlate with the reactive surface area. Although both solids possess the same specific surface area, the difference in their reactive surface areas is not accessible by BET measurements.

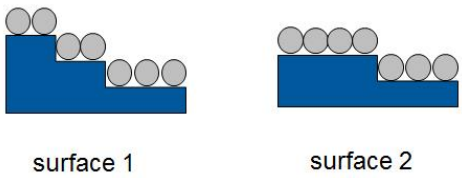

Figure 17: Schematic illustration of two surfaces with a different topography and spheres corresponding to the adsorbed gas molecules within a BET measurement. Even though the specific surface areas of the solids 1 and 2 are equal, they differ in their reactive surface area.

The characterisation of the surface area is still very difficult [71]. Especially in anisotropic solids, e.g. sheet minerals as clay or mica the BET surface might not match or even correlate with the reactive surface area due to different reactive edges of side and basal planes [72-73]. From a mechanistic point of view, the normalisation of the dissolution rate to a surface area regardless of its reactivity at the different surface site is an insufficient simplification which prohibits unravelling the different processes. Alternative microscopic approaches are applied to directly observe the dissolution at the mineral-water interface. Recent observations indicate that not only one dissolution rate but a spectrum of rates exists [74].

Figure 18 gives an example of rate spectra for micrite. The red curve corresponds to a single crystal and the blue one denotes a polycrystalline solid which is microcrystalline. This figure indicates a difference in dissolution behaviours of a single crystal and a polycrystalline solid in their distribution and the resulting overall dissolution rate. However, the mean values as depicted by the bars on top of the rate spectra correspond relatively well with the measured rate distribution. Especially for the microcrystalline micrite it matches relatively well which might be in a way similar to the pyrochlores of this study, because dissolution rates were measured for polycrystalline pyrochlores.

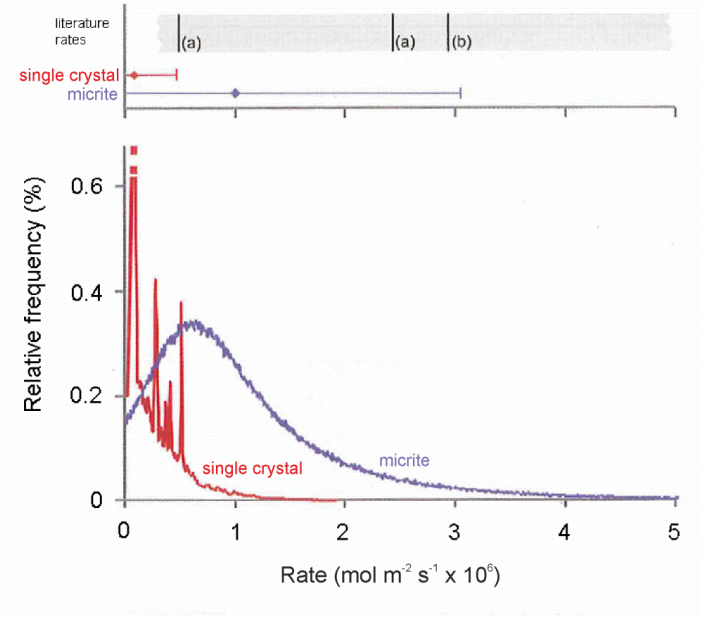

Figure 18: Micrite dissolution rates of a single crystal (red) and a polycrystalline solid (blue) with their contribution to the overall dissolution rate given in percentage values. The coloured bars correspond to mean values from VSI measurements whereas the literature data correspond to calcite dissolution rates at similar experimental conditions. Adapted from Lüttge et al. [74].

In the literature oftentimes minerals show different dissolution or growth rates along different crystallographic directions [75-76] indicating a different reactivity of the surface.
The dissolution and growth processes proceed stepwise according to the Kossel and Stranski model in section 2.4.2 (dissolution kinetics). Mostly reactive sites such as etch pits or kinks initiate the stepwise dissolution resulting in a heterogeneous surface [76]. There is a need to define the reactive site density to gain a profound understanding how the dissolution processes proceed. This points out, how important an additional microscopic analysis of the solid surface is.

Microscopic approaches - From a fundamental point of view, the empirical rate equation (7) is only valid if just one mechanism occurs at one defined surface site and does not change within the observed parameter interval. In complex systems such as the ceramics of the dissolution studies presented here the empirical approach can only be used to study the total dissolution rate regardless of the heterogeneity of surface sites which may depend on the different crystallographic planes and the occurrence of kinks, steps and surface roughness. A deconvolution of the total dissolution rate to the individual microscopic mechanisms and rates is not possible based on macroscopic observations. Therefore besides the macroscopic experiments there is a need for complementary microscopic information on the dissolution which will also consider the processes at the solid surface itself. Microscopic approaches such as atomic force microscopy (AFM) or vertical scanning interferometry (VSI) are suitable techniques to get access to the reactive surface area, which was discussed in the previous section. New theoretical approaches have been proposed in the literature to more accurately describe the dissolution rate based on microscopic observations, e.g. the step-wave model [77]. More recently, kinetic Monte Carlo calculations have been proposed as a way out of the problems related to the evolving surface reactivity [74].
However, from a pragmatic point of view macroscopic dissolution experiments are still the state of the art approach to gain insight into the dissolution behaviour of potential nuclear waste forms and AFM or VSI are only considered as complementary information to obtain a detailed process understanding of the dissolution mechanism.

2.4.3 Experimental background: Dissolution kinetics

Macroscopic determination of dissolution rates - The dissolution kinetics are an important property of potential host phases because it defines the source term for the radionuclides in the case of water intrusion into a high level nuclear waste repository. Within

this work, the influence of classical parameters such as pH and temperature on the dissolution kinetics is studied in detail. Moreover, a link between the crystal structure, the chemical composition and the dissolution kinetics is made.

In general there are two possible setups for dissolution experiments:

(1) batch experiments

(2) dynamic dissolution experiments.

These setups are described in detail with their assets and drawbacks in the following sections.

Batch dissolution experiments - Within a batch experiment a powdered or a monolithic sample is set into a closed reaction vessel with the dissolution medium (Figure 19). In many cases this is realised with highly durable plastic bottles, e.g. made of Nalgene as it was the case for this study. These are heated in a drying oven or an oil bath to the desired temperature for the dissolution experiment. The experimental setup of the batch experiment with ideal pyrochlore was adapted from Oelkers and Poitrasson [78].

The main asset of a batch experiment is its very simple experimental set up and the simulation of a closed system (Figure 19). Moreover, there are several standardised instructions e.g. the MCC tests, from the International Standards Organization's Materials Characterisation Centre (MCC) [10]. They were developed for a better comparison of the results, which was often a problem of former studies. The batch experiments are also applicable for radioactive samples, because they can be implemented into a glovebox. In general, batch experiments are the most common experimental setup in the available literature regarding the determination of mineral dissolution rates.

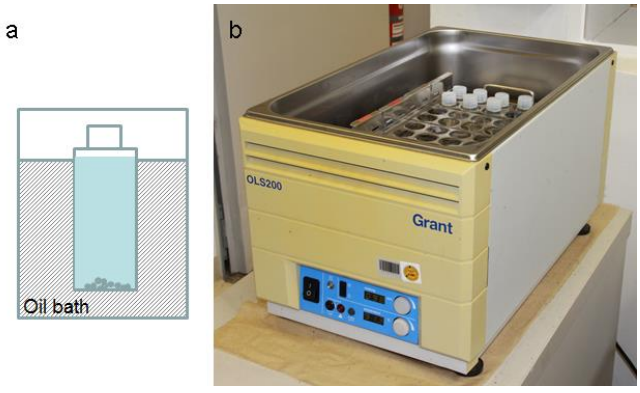

Figure 19: (a) Schema of a batch dissolution experiment; (b) the temperature of the reaction vessel is kept constant by a shaking oil bath which assures a homogeneous dissolution medium inside the reaction bottle due to constant movement.

The main drawback of this setup is the possibility of drifting conditions. Any changes of the starting conditions due to the dissolution processes inside the experiment will directly influence the experiment and cannot be controlled any longer, e.g. far-from equilibrium conditions or a constant pH cannot be assured. Therefore, the interpretation of data from this type of experiment has to be done with great caution.

Dynamic dissolution experiments - Dynamic experiments have been used in many kinetic studies [78-80] because the reaction rates are obtained at steady state conditions without any fitting procedure to a presumed rate law.

A setup for temperatures below 100 °C was presented in Neeway et al. [81] and Dacheux et al. [79]. This experiment consisted of a leachant reservoir, a peristaltic pump, a reactor and a collection bottle (Figure 20).

Dissolution experiments above 100 °C require a specialised experimental setup to keep the leachant solution in the stability field of water. Reactor systems for this task are described by Berger et al., (1994) [82], Dove and Crerar (1990) [83] and Oelkers and Poitrasson (2002) [78].

The main asset of dynamic dissolution experiments is the preservation of the conditions chosen at the beginning of the experiment during the whole duration of the experiment. The powder preparation is not as critical as for the batch experiments, because perturbations which are caused by fines will only occur during the initial phase of the experiment. Due to the constant exchange of the dissolution medium the experiment can be carried out at far from equilibrium conditions. This allows a separation of the variables according to the rate equation to study the influence of the different parameters individually.

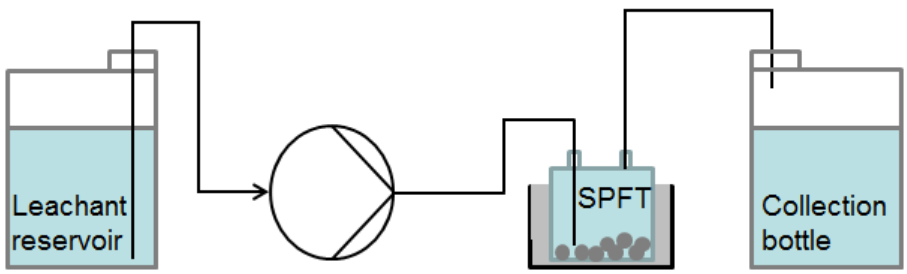

Figure 20: Schema of a dynamic dissolution experimental setup (1) with a single pass flow through reactor for experiments at temperatures below 100 °C. The dissolution medium is pumped with a peristaltic pump into the reactor with the ceramic powder at the bottom. The reactor is tempered with an oil bath. The outflow is cumulated in a collection bottle.

A disadvantage is the high consumption of the dissolution medium. Especially for actinide doped ceramics this is a critical aspect. Moreover, an advanced experimental setup is needed to study the temperature influence above 100 °C.

Derivation of dissolution rates from batch and dynamic experiments - The normalised dissolution rates R from batch experiments were determined from a linear fit of the Nd-concentration versus time (Figure 49) according to the following equation:

$$Rate(Nd) = \frac{dc(Nd)}{dt} \cdot \frac{V}{\nu(Nd) \cdot A \cdot m} \tag{26}$$

where *c(Nd)* refers to the concentration of Nd in the dissolution medium at the time *t*, *V* is the volume of the dissolution agent, ν(Nd) the stoichiometric number of Nd moles in one mole of pyrochlore, *A* the specific surface area of the ceramic powder determined by BET and *m* the mass of the ceramic powder [20].
The theoretical background of the determination of normalised dissolution rates from dynamic experiments is described in detail in the literature e.g. Dove and Crerar [83]. The normalised dissolution rate based on the release of an element i from a ceramic can be described by the following equation [73, 78, 83-85]:

$$Rate = \frac{F}{A \cdot m \cdot \nu_i} \cdot \Delta c_i \tag{27}$$

with

F fluid flow rate [$L \cdot d^{-1}$]

A the specific surface area of the ceramic powder [$m^2 \cdot g^{-1}$]

m mass of ceramic powder in the reactor [g]

ν_i stoichiometric number of moles of the element i (Nd or Zr) in one mole of pyrochlore or defect fluorite [-]

Δc_i concentration difference between the outflow and inflow concentrations of element i in solution [$g \cdot L^{-1}$]

The rate in equation (27) represents the total dissolution rate of the complete pyrochlore based on the release rates of the cations Nd and Zr. If the Nd- and Zr-derived pyrochlore rates are identical, congruent dissolution is observed. Multioxides often show significant differences in the dissolution of two or more elements, which is referred to as incongruent

dissolution. Incongruent dissolution is widely spread for multioxides and silicates and can be explained by the formation of secondary phases or the preferential dissolution of one of the elements. In such cases the release of the different elements needs to be monitored and potential secondary phases need to be studied to gain a complete idea about the dissolution mechanism. Non-ideal dissolution is observed when the rates calculated from Nd and Zr deviate beyond the total uncertainties of A, Δc_i, m and F which is about 40% for all experiments. This error was based on error propagation. Steady state rates were calculated from average concentrations of each experiment after a steady state was reached.

Thermodynamic calculations – The deviation from thermodynamic equilibrium at the preset conditions was calculated with thermodynamic modelling via the GEM-Selektor package [86-88]. There were two aims in the focus of the modelling procedure. In the first place the solubility of $Nd_2Zr_2O_7$ in acidic aqueous environments and at elevated temperatures should be identified. Secondly the possibility of precipitation of secondary phases, like Nd_2O_3, $Nd(OH)_3$, $Zr(OH)_4$ or ZrO_2, during the dissolution experiments carried out in the present study, should be identified. The Davies model was used to compute the activity coefficients of aqueous species [89]. The standard molar Gibbs free energies, enthalpies, entropies and heat capacity values for the $Nd_2Zr_2O_7$, Nd_2O_3 and $Nd(OH)_3$ solids were taken from Jacob et al. [90], Lutique et al. [91-92], Diakonov et al. [93] and Lide [94]. Additional thermodynamic data for other solids and aqueous complexes were adopted from implemented NAGRA-PSI (Hummel et al. [95]) and SUPCRT92/Slop98 (Shock et al. [96]) databases.

3 Aim of this work

ZrO_2 - Nd_2O_3 pyrochlore type ceramics as potential waste forms were in the focus of this study. The following main questions arise for pyrochlore ceramics in the context of nuclear waste management:

- Phase stability field of pyrochlore and consequence of non-stoichiometry?
- Structural uptake of radionuclides?
- Chemical stability and effect of phase transformation to defect fluorite?

Phase stability field of pyrochlore and consequence of non-stoichiometry – Based on the phase diagrams presented above the stability field of ZrO_2 - Nd_2O_3 pyrochlore type ceramics remains unclear. Only very few systematic studies exist which cover a wide range of possible compositions. However, for a detailed understanding of the consequences of partly exchanging the A or B cation with MA or Pu, pyrochlores with mixed A or B positions rather than stoichiometric $A_2B_2O_7$ pyrochlores become relevant. Therefore a broad range of different compositions was synthesised and characterised using XRD and TEM.

Structural uptake of radionuclides - Previous studies via extended X-ray absorption fine structure (EXAFS) with Am, Np, Pu and U have indicated that Pu can be taken up by the pyrochlore crystal lattice on regular lattice sites. Additional information was obtained by applying TRLFS to Eu and Cm doped pyrochlore and defect fluorite ceramics. To get closer to a real waste form ^{239}Pu-pyrochlores with different Pu contents were synthesised using the wet-chemical coprecipitation synthesis route. Subsequent characterisation by XRD, SEM and EDX was carried out.

Chemical stability and effect of phase transformation to defect fluorite – Only very limited systematic knowledge is available regarding the dissolution kinetics of pyrochlores as a function of deviation from the stoichiometric composition. The effect of the phase transformation of pyrochlore to defect fluorite with respect to the dissolution kinetics is so far not discussed in the open literature.
A systematic macroscopic study of dissolution kinetics was carried out for a wide range of compositions of ZrO_2 - Nd_2O_3 ceramics using batch and dynamic dissolution experiments. Besides the pH and temperature dependence of the dissolution kinetics a link between the microstructure and the dissolution kinetics was made. For a sophisticated understanding how the dissolution proceeds additional microscopic experiments were conducted. For the microscopic study of the dissolution kinetics SEM and VSI were applied.

4 Materials & methods

Within this work Nd_2O_3 – ZrO_2 ceramics with the pyrochlore and defect fluorite structure were synthesised by different approaches. Subsequent charactersiation took place, where the ceramics were studied on the bulk level with powder X-ray diffraction and at local sites, e.g. by transmission electron microscopy. Finally the properties such as dissolution kinetics and radionuclide uptake were covered.

This chapter is dedicated to the detailed explanation of the synthesis procedures. Moreover, all characterisation techniques which were applied within this work are listed.

4.1. Synthesis of pyrochlores

The different synthesis routes as precipitation and sol-gel synthesis, which were applied to obtain Nd_2O_3 – ZrO_2 ceramics are described within this chapter.

All ceramics were synthesised from high purity chemicals. A table with the purity and supplier of the used chemicals is provided in the appendix (Table 13).

4.1.1 Synthesis by coprecipitation with liquid ammonia

The coprecipitation synthesis route was carried out according to Chen (2009) [22]. Aqueous solutions with a concentration of 0.1 M of the metal salt solutions were prepared. All solution concentrations were checked by inductively coupled plasma optical emission spectrometry (ICP-OES; Thermo Scientific iCAP6500 Duo) measurements due to the hygroscopic nature of the starting salts. Batches of 20 mmol of the desired composition were prepared in order to obtain about 12 g of pyrochlore or defect fluorite compositions, respectively. The desired proportions of the metal salt solutions were mixed and stirred for 5 min to ensure a homogeneous mixture. The mixture was transferred into a dropping funnel and the hydroxides were simultaneously and quantitatively precipitated by addition of the metal salt solution into concentrated NH_4OH. This was realised using a dropping funnel with a dropping velocity was about 2 drops/sec. The precipitate was seperated by centrifugation for 15 min at 4000 rpm. The supernatant was checked for complete precipitation by addition of a few drops of NH_4OH. Afterwards, the precipitate was washed thoroughly by stirring with deionised water until the washing water was free of chloride and nitrate (QUANTOFIX dipsticks, Macherey-Nagel). Usually this was realised in six washing steps with each about 600 mL deionised water. After each washing step the precipitate was separated from the washing water by centrifugation for 20 min at 4000 rpm. The precipitate was transferred into a porcellaine dish and dried over night at 120 °C and ground thoroughly using a mortar and pistel.

4.1.2 Synthesis with gaseous ammonia

For the precipitation with gaseous ammonia 2.5 L of distilled water were poured into a 3 L Erlenmeyer flask. The desired amounts of $ZrOCl_2 \cdot 8H_2O$ and $Nd(NO_3)_3 \cdot 6H_2O$ were dissolved in the water to obtain a 10 mmol/L aqueous solution. The solution was homogenised by stirring for 10 min. To precipitate the hydroxides gaseous ammonia was introduced to the solution with a flow rate of 0.39 L/min. After 30 min the precipitation was complete, which was checked by ICP-MS measurements of the solution. The mixture was stirred for further 2 h before the precipitate was separated via filtration. The precipitate was washed several times until the washing water was free of chloride and nitrate. The precipitate was transferred into a porcelain dish and dried in a drying oven over night at 120 °C.

4.1.3 Sol-gel synthesis

Here an internal gelation process was chosen. 0.16 molar solutions of $ZrOCl_2$ and $Nd(NO_3)_3$ were prepared in distilled water. An aqueous solution of 2.4 mol/L urea and 0.8 mol/L HMTA was prepared.

The metal salt solutions were cooled with an ice bath and the desired proportions of the Zr- and Nd-solutions were mixed to obtain a total volume of 1 mL. Afterwards 1 mL of the urea/HMTA mixture was added, which was cooled to prevent a premature gelation. The solutions were stirred for 30 sec to obtain a homogeneous solution. Afterwards, the solution was dropped via a syringe with a needle into a column filled with 90 °C hot silicon oil. While the drops reached the sieve at the bottom of the column the gelation took place. The kernels were allowed to gelify for 30 min in the column. The oil was removed by two washing steps with petroleum ether (100 mL) each about 10 min. The kernels were aged overnight in 100 mL of a 12.5 % NH_4OH solution. The kernels were washed two times with ammonia solution (100 mL) and all washing waters were analysed by ICP-MS to exclude Nd- or Zr-losses due to the washing steps. The kernels were dried overnight at ambient temperature.

The following sintering procedure was applied to the kernels: The kernels were heated to 1980 °C with a heating rate of 1.9 °C/min. The temperature of 220 °C was reached with a heating rate of 0.5 °C/min while the heating rate was increased to 3 °C/min to reach a temperature of 400 °C. With 1.1 °C/min a temperature of 500 °C was approached whereas the final sintering temperature of 1400 °C was reached with a heating rate of 3.75 °C/min and the dwell time was 3.5 In the temperature range up to 500 °C slow heating rates were chosen to allow a decomposition of the organic residues without cracking of the kernels.

The sintering temperature of sample SF-12 was 1300 °C and therefore lower than for the other samples.

4.1.4 Ceramic pellet formation

For a ceramic pellet formation different procedures were applied to the hydroxides from section 4.1.1 and 4.1.2. All powders were thoroughly ground with mortar and pistil after drying. A calcination step was applied to each sample in air for 2 h at 600 °C in an alsint® sintering crucible. The heating and cooling rate was 4.8 °C/min. A second grinding step was applied after the calcination step. Then the following variations of cold pressing and subsequent sintering or hot pressing were applied, which are described in the following paragraphs.

Cold pressing & sintering - One approach to obtain a ceramic pellet was realised by cold pressing and a subsequent sintering procedure.

About 2.5 g of the calcined powder were poured into a die with a diameter of 10 mm. With a cold press a press capacity of 50 kN was applied for 7 sec to press a pellet. The pellet was sintered in an alsint® sintering crucible at 1600 °C.

The heating and cooling rate was 5.3 °C/min. The sintering durations were varied according to the following steps:

S1: Sintering duration of 5 h

S2: The pellets were ground after S1 for characterisation by XRD. Afterwards the powder was repressed with the cold press at the same conditions which were applied before. These pellets were sintered for additional 10 h, which leads to an overall sintering time of 15 h.

Hot pressing – S3: About 2.5 g of the calcined powder were pressed in the cold press under the conditions mentioned above. After this precompaction step the pellet was transferred into a graphite matrix of a hot uniaxial press. Here a HP W 5 of the company FCT Systeme GmbH was used. The pressing and sintering conditions were 1450 °C and 3.9 kN in inert gas atmosphere. The sintering time was 1.5 h whereas the full press capacity of 3.9 kN was applied during 0.5 h. The obtained pellets had a greyish colour due to the oxygen deficit. The surface of the pellets was polished to remove graphite contaminations. In order to adjust the oxygen deficit the pellets were resintered for 5 h at 1600 °C in air. The heating and cooling rate were 5.3 °C/min.

4.1.5 Powder preparation for dissolution experiments

The obtained pellets were crushed with a cold press and a mortar and pistil and wet sieved into two fractions of 180 – 100 µm and <100 µm. The 180 – 100 µm fraction was rinsed for 5 min with distilled water to remove residual fines. The powder was dried overnight at 120 °C in a drying oven.

4.1.6 Synthesis of $La_2Zr_2O_7$ for TRLFS measurements

For the TRLFS measurements $La_2Zr_2O_7$ samples with the defect fluorite and pyrochlore crystal structure were synthesised according to a coprecipitation with liquid ammonia (section 4.1.1). The Cm doped samples were synthesised with a 20 µmol/L stock solution in 1.0 mol/L $HClO_4$. The Cm-248 content was 97.3 % whereas Cm-246, Cm-245, Cm-247 and Cm-244 were only present in trace amounts.

The lanthanide samples contained 1000 ppm Eu whereas the Cm content was as low as 2 ppm. The sintering durations and the obtained crystal structure are listed in Table 1.

Table 1: Synthesis conditions and overview of samples which were characterised by TRLFS.

Name	Dopant	Content of dopant (ppm)	Sintering temperature (°C)	Crystal structure
Eu-DF	Eu	1000	1000	Defect fluorite
Eu-Py	Eu	1000	1400	Pyrochlore
Cm-DF	Cm	2	1000	Defect fluorite
Cm-Py	Cm	2	1400	Pyrochlore

4.1.7 Synthesis of Pu-pyrochlores

All work concerning the Pu-pyrochlores was carried out in a dedicated glovebox line at NRG in Petten, NL. The Pu-pyrochlores were synthesised according to the coprecipitation route (4.1.1). Standard solutions of 0.3 mol/L were prepared from $ZrOCl_2 \cdot 8H_2O$ and $Nd(NO_3)_3 \cdot 6H_2O$ and the concentration was checked by ICP-OES measurements. All syntheses described in this section were carried out in a glovebox line under air atmosphere. The thermal treatment was carried out in a glovebox line under argon atmosphere. The Pu compound was provided by NRG and originally obtained from Kjeller, Norway. This material was stored for more than 14 years at NRG in Petten. A thermal analysis in 1998 suggested the chemical formula $Pu(NO_3)_4 \cdot xH_2O$. In addition, impurities were reported. The described weight loss in two steps was in agreement with the thermal decomposition of $Pu(NO_3)_4 \cdot xH_2O$ (x = 3, 5) via a plutonylnitrate to PuO_2 [53, 97]. It was not possible to perform thermal analysis during my internship as the equipment was out of order. The X-ray diffraction of the

starting material did not give any further information as the material was found to be amorphous. All experiments were carried out based on the assumption that the starting composition had the stoichiometry of $Pu(NO_3)_4 \cdot 5H_2O$.

Prior to the synthesis of Pu-pyrochlores a stoichiometric $Nd_2Zr_2O_7$ pyrochlore was synthesised inside the glovebox as reference substance according to the synthesis route described in section 4.1.1. Modifications of the Pu pyrochlore fabrication lead to three different synthesis procedures: Pu-syn-1, Pu-syn-2 and Pu-syn-3. In order to yield highly homogeneous materials, the synthesis of ^{239}Pu-pyrochlore was realised by a coprecipitation route. The synthesis route which was applied here is not published in the open literature and was successively enhanced. Within the chosen synthesis, the hydroxides were precipitated using an aqueous ammonia solution.

Pu-syn-1: The appropriate amounts of $Nd(NO_3)_3$ and $ZrOCl_2$ standard solution (Table 2) were mixed and diluted to a concentration of 0.1 mol/L with deionised water in a PE bottle (V = 100 mL). The desired amount of $Pu(NO_3)_4 \cdot 5H_2O$ was dissolved in 1 mol/L HNO_3 to yield a 0.1 mol/L Pu-nitrate solution. First, the Pu hydroxide was precipitated dropwise in 40 mL liquid ammonia (Figure 21a) with the help of an Eppendorf pipette. Afterwards, $Nd(OH)_3$ and $Zr(OH)_4$ were coprecipitated to the Pu-hydroxides via a dropping funnel (1 drop/sec) (Figure 21b). The precipitate was separated from the solution by centrifugation with 4000 rpm/min for 10 minutes. A few drops of NH_4OH were added to the supernatant, to check for complete precipitation. In all cases a complete precipitation had taken place, because no further precipitation was observed after the NH_4OH addition. The precipitate was washed in several steps by stirring with 80 mL deionised water respectively the slurry of water and precipitate until the washing water was free of chloride and nitrate. This was checked by the use of chloride and nitrate dipsticks (Macherey-Nagel). Therefore, six washing steps were required. The washed precipitate was left to dry in the glovebox, transferred to an argon glovebox line and dried in a drying oven at 60 °C for 4 hours. The powder was ground and sintered in an alsint sintering crucible for 2 h at 600 °C in argon atmosphere. The heating and cooling rate was adjusted to 4.83 °C/min. The thoroughly ground powder was pressed into a pellet form with a 6 mm die and a pressure of about 760 MPa. The pellet was sintered at 1450 °C in a tube furnace under reducing atmosphere (Ar-5% H_2). The sintering time varied and is given in Table 15.

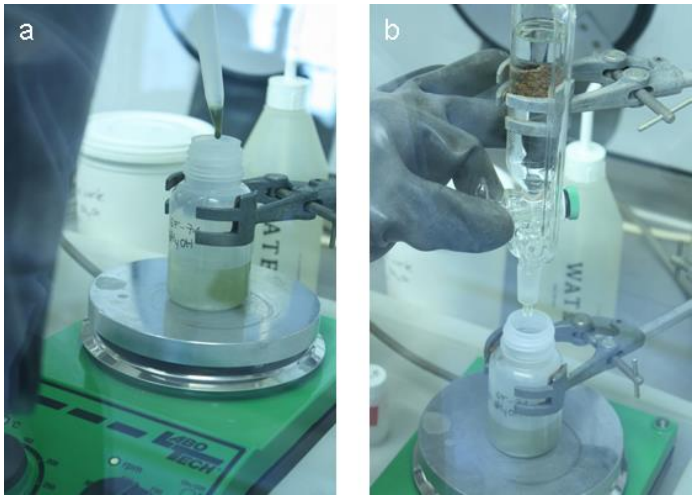

Figure 21: (a) Precipitation of the Pu-hydroxides and (b) adjacent precipitate of the Nd-, and Zr-hydroxides.

Table 2: Chemical composition and appropriate molar amounts of Nd, Zr and Pu.

Sample	Chemical formula	Synthesis method	n(Nd) (mmol)	n(Pu) (mmol)	n(Zr) (mmol)
SF-70	$Nd_2Zr_2O_7$	Section 4.1.1	8	-	8
SF-71-P1	$Nd_{1.9}Pu_{0.1}Zr_2O_7$	Pu-syn-1	2.56	0.135	2.70
SF-74-P1	$Nd_{1.8}Pu_{0.2}Zr_2O_7$	Pu-syn-2	2.39	0.265	2.65
SF-74-P2	$Nd_{1.8}Pu_{0.2}Zr_2O_7$	Pu-syn-2			
SF-77-P1	$Nd_{1.9}Pu_{0.1}Zr_2O_7$	Pu-syn-3	1.28	0.0675	1.35
SF-77-P2	$Nd_{1.9}Pu_{0.1}Zr_2O_7$	Pu-syn-3			

Pu-syn-2: The synthesis remained unchanged for a sample with 10 mol% Pu. For this sample the calcination as well as the sintering step were carried out under reducing atmosphere. The heating and cooling rates for the calcination step were lowered from 300 °C/h to 200 °C/h.

Pu-syn-3: Within a third approach a coprecipitation of all hydroxides including the plutonium hydroxide was realised (Figure 41b). The aqueous solutions of $Nd(NO_3)_3$ and $ZrOCl_2$ were acidified to $c(HNO_3)$ = 1 mol/L and mixed prior to the addition of the Pu solution to avoid the Pu polymer formation. The desired amount of $Pu(NO_3)_4 \cdot 5H_2O$ was dissolved in nitric acid. The Pu concentration was reduced to c(Pu) = 0.01 mol/L whereas the acidity of the nitric acid

was kept constant at 1 mol/L. A 0.01 mol/L $Pu(NO_3)_4$ solution was prepared with 1 mol/L HNO_3. Within the green solution some solid remained unsolved. The sample was gently heated to 50 °C under stirring for 70 min. The solid remained unsolved and was separated by centrifugation (4000 rpm, 10 min). The clear, light green solution was added slowly to the acidified metal salt solution which was shaken. No precipitation occurred. This solution was added into 40 mL concentrated ammonia solution via a dropping funnel with 1 drop/sec. The precipitate was separated by centrifugation, washed by stirring with deionised water and dried as mentioned above. The thermal treatment was carried out according to Table 15.

All samples were characterised by X-ray diffraction using a PDS120 Powder Diffractometer with a CPS120 Detector. The pattern were recorded from 0 – 120° 2θ. The pellet SF-71-P1 was additionally measured by a D2 from Bruker.
The pellet SF-77-P1 was characterised by XRD, ground and a second XRD analysis was carried out at the powdered sample. Afterwards the powder was repressed into a pellet and sintered for 5 h at 1450 °C to remain in pellet shape.
This pellet with the stoichiometry $Nd_{1.9}Pu_{0.1}Zr_2O_7$ was investigated by scanning electron microscopy (SEM) additionally. The pellet was sputtered with Au-Pd to avoid the charging of the specimen during measurements.

4.2. Dissolution Experiments

4.2.1 Batch dissolution experiments

All batch dissolution experiments were carried out in c(HCl) = 0.1 M at 90 °C. A shaking oil bath (Grant) was used to keep the temperature constant and to simultaneously assure a homogenisation of the leachant inside the reaction bottle. In a first stage of the experiment, the powder was pre-leached for 28 days in a perfluoroalkoxy polymer (PFA) bottle (V = 30 mL) by adding 25 mL of leachant to 200 mg of pyrochlore powder. The powder was washed with water, dried and afterwards used for the final batch dissolution experiment. The solid/liquid ratio of 8 $g \cdot L^{-1}$ was identical to the pre-leaching. Regularly, an aliquot of 500 µL was sampled. In order to avoid fines that may be present due to the powder preparation, or particles that may have been removed during sampling, the solution was filtered with an USY-1 ultrafilter (10,000 Da, Advantec). Afterwards, the Nd-concentration was determined by ICP-MS.

4.2.2 Dynamic dissolution experiments

Two different experimental setups were used, depending on the temperature of the experiment: (1) experiments at temperatures below 100 °C were set up in a perfluoroalkoxy polymer (PFA) reactor while (2) experiments at temperatures higher than 100 °C were set up in a pressurised titanium reactor.

Dissolution experiments at temperatures below 100 °C were carried out in a Savillex PFA reactor (50 mL) with a solution of deionised water and HCl as leachant. Blank tests were run before the dissolution experiments to clean the reactors and tubes and to derive blank concentrations of Zr and Nd. For the dissolution experiment about 900 mg of the prepared powder were placed in the PFA flow-through reactor and 45 mL of the acid were added. Due to the high density of pyrochlore 6.363 g/cm^3 [98] and defect fluorite and the coarse grain size used within the experiments no filters were used in the experimental setup to keep the ceramic powder inside the flow-through reactor. A peristaltic pump continuously exchanged the solution within the reactor. A flow rate of 0.15 mL · min^{-1} was set and monitored regularly before sampling. The leachant entered the reactor at the bottom near the ceramic powder and left at the top of the reactor. Due to the expected low dissolution rates [99] stirring was not applied for this experimental setup. During the experiments, samples of the outflow solution were taken regularly for chemical analyses of Nd and Zr, filtered through ultrafilters (10,000 Da, Advantec) and prepared for ICP-MS analyses. Prior to sampling, each filter was flushed with 6 mL of the effluent which were discarded before the final filtration step took place. This type of experiments was typically run for 80 days. For the ICP-MS measurements, the samples were acidified by adding 1 vol% HNO_3 suprapur®.

For dynamic experiments at temperatures above 100 °C, a hydrothermal flow through reactor was designed with Parr Instrument Company and implemented at IEK-6 (Figure 22). The experimental setup consisted of a reactor vessel (Parr; V = 50 mL), a high pressure liquid chromatography pump (Wagner) and a computer controlled pressure valve. Dynamic dissolution experiments were carried out at a temperature of 110 °C with HNO_3 as leachant.

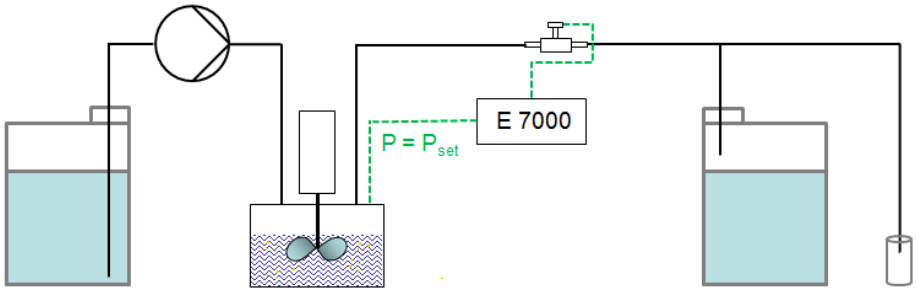

Figure 22: Sketch of a dynamic dissolution experimental setup for T > 100 °C. The solution is pumped via a liquid chromatography pump into a pressurised reactor. The flow rate is regulated by a pressure gauge that communicates with the reactor via a controller E 7000. The outflow is collected in a can bottle and or sampled every now and then to analyse the elemental release.

Prior to the start of the experiment a primary pressure was adjusted. Inside the reactor vessel was equipped with a pressure gauge, an externally driven stirring system and a thermocouple. The pressure gauge was connected to a controller (E 7000) and computer system which regulated the outflow of the reactor via the pressure valve. The outflow of the reactor was filtered through a Ti cylinder frit with a pore size of 2 µm and an in-line Ti-filter with 0.5 µm pore size to avoid the loss of fines. All parts that were in contact with the leachant were made of polyether ether ketone (PEEK), polytetrafluoroethylene (PTFE) or Ti to avoid corrosion. Within this setup the solution is stirred to ensure a homogenisation of the dissolution medium, because the fresh solution does not enter the reactor at the bottom as it was the case for the lower temperature setup which assured a homogenisation.

To start the dissolution experiment, 1 g of the respective powder sample and 35 mL of 0.1 n HNO_3 were placed inside the reaction vessel. The reactor was pressurised with Ar to 5 bar and heated to 110 °C. The reactor was continuously stirred at a low stirring rate of 100 rpm to keep the solution homogeneous. During the experiment the pressure was kept constant by pumping fresh solution into the reactor at pump rates of 0.5 to 0.6 ml · min^{-1} and continuously releasing solution through the pressure valve. This type of experiments was run for 30 d. Samples were taken, filtered and analysed in the same way as for the experiments at 70 and 90 °C. All experimental parameters are summarised in Table 3.

Table 3: Overview of the experimental conditions for all experiments.

Name (-)	Nd_2O_3 (mol%)	Crystal structure (-)	Temperature (°C)	c(HCl) (mol · L^{-1})	Experimental setup (-)
SF-117	33.3	Pyrochlore	70	0.10	PFA reactor
SF-121	33.3	Pyrochlore	90	0.01	PFA reactor
SF-98	33.3	Pyrochlore	90	0.10	PFA reactor
SF-119	33.3	Pyrochlore	90	1.00	PFA reactor
SF-125	33.3	Pyrochlore	110	0.10	Ti reactor, HNO_3
SF-89	12.9	Defect fluorite	90	0.1	PFA reactor
SF-118	15.6	Defect fluorite	70	0.10	PFA reactor
SF-122	15.6	Defect fluorite	90	0.01	PFA reactor
SF-123	15.6	Defect fluorite	90	0.10	PFA reactor
SF-120	15.6	Defect fluorite	90	1.00	PFA reactor
SF-131	15.6	Defect fluorite	110	0.10	Ti reactor, HNO_3
SF-91	17.6	Defect fluorite	90	0.10	PFA reactor
SF-124	22.0	Pyrochlore	90	0.10	PFA reactor
SF-92	25.0	Pyrochlore	90	0.10	PFA reactor
SF-94	35.1	Pyrochlore	90	0.10	PFA reactor

4.3. Analytical methods

Within this chapter all applied characterisation techniques with the corresponding equipment are given.

4.3.1 XRD

Within this work a D8 Advance with a *θ-θ* geometry and a D4 Endeavour with a *θ-2θ* geometry (CuK_α, λ = 0.15406 nm) from Bruker AXS GmbH were used to characterise the crystal structure of the samples. In general the samples were finely ground and prepared on a plastic slit sample holder. The surface of the powder was smoothed with the help of a glass wafer. In case of limited amounts of the prepared samples, a small amount was ground under acetone. The finely ground sample was prepared with the help of an Eppendorf pipette on a monocrystalline silicon wafer. Part of the pellets was directly mounted on a plastic sample and XRD data were recorded from the pellet. The height was adjusted by mounting the sample with plasticine to a plastic sample holder. The XRD pattern were recorded in the region between 10 – 90 or 10 – 130°. Usually a step width of 0.02 degree and a dwell time of

5 sec for every step were applied. The XRD pattern were analysed with version 1.11g of the “Match!” software (Crystal Impact).
The Pu-pyrochlore samples were measured with a Nonius PDS 120 INEL powder diffractometer with a 120° curved position sensitive detector.

4.3.2 FIB

The focused ion beam (FIB) NVision 40 from Zeiss was used to prepare a thin lamella for TEM measurements out of a bulk material. The device was equipped with a chamber Everhardt Thornley SE detector and an in-lense SE detector. Here, a lamella was cut out of a powdered sample which was prepared under a microscope. The powder was fixed on an Al sample holder with conductive silver and coated with carbon. To protect the region of interest against beam damage an approximately 2 µm thick carbon layer was deposited, which is highlighted by the arrow in Figure 23a.
All milling steps were carried out at 30 kV. The final low kV polishing step was conducted at 5 kV.
Two trapezoids of about 20 µm in width, 20 µm in depth and about 10 µm in height were defined to remove the material in front and behind the lamella. The material was removed by a gallium ion beam which followed the trapezoids in the direction of the arrows (Figure 23b) with a milling current of 13 nA. Within the next step, two rectangles of 20 µm width, 20 µm depth and 1.03 µm height were defined and positioned closer to the lamella for an additional thinning process. The milling current for these rectangles was 1.5 nA. Figure 23c shows the tilted lamella which was prepared to be cut clear by a “u-cut” at 700 pA. For the lift-out process a manipulator needle is fixed to the lamella by carbon deposition (Figure 23d). The next step was to cut the lamella clear, move it to the TEM grid and mount it at the TEM grid by carbon deposition (Figure 23e). After removing the needle from the lamella by cutting it off, the lamella was thinned with 150 pA at the middle part of the lamella from the front and backside. To reduce beam damage by the Ga-ion beam, the milling current was subsequently reduced to 40 pA. The final step was the low kV polishing at 50 pA to remove amorphous parts of the surface which were caused by the ion beam acting on the surface. The thinned lamella was transparent for the electron beam at 20 kV. The thickness is less than 300 µm and the grain boundaries became visible as it is shown in Figure 23f.

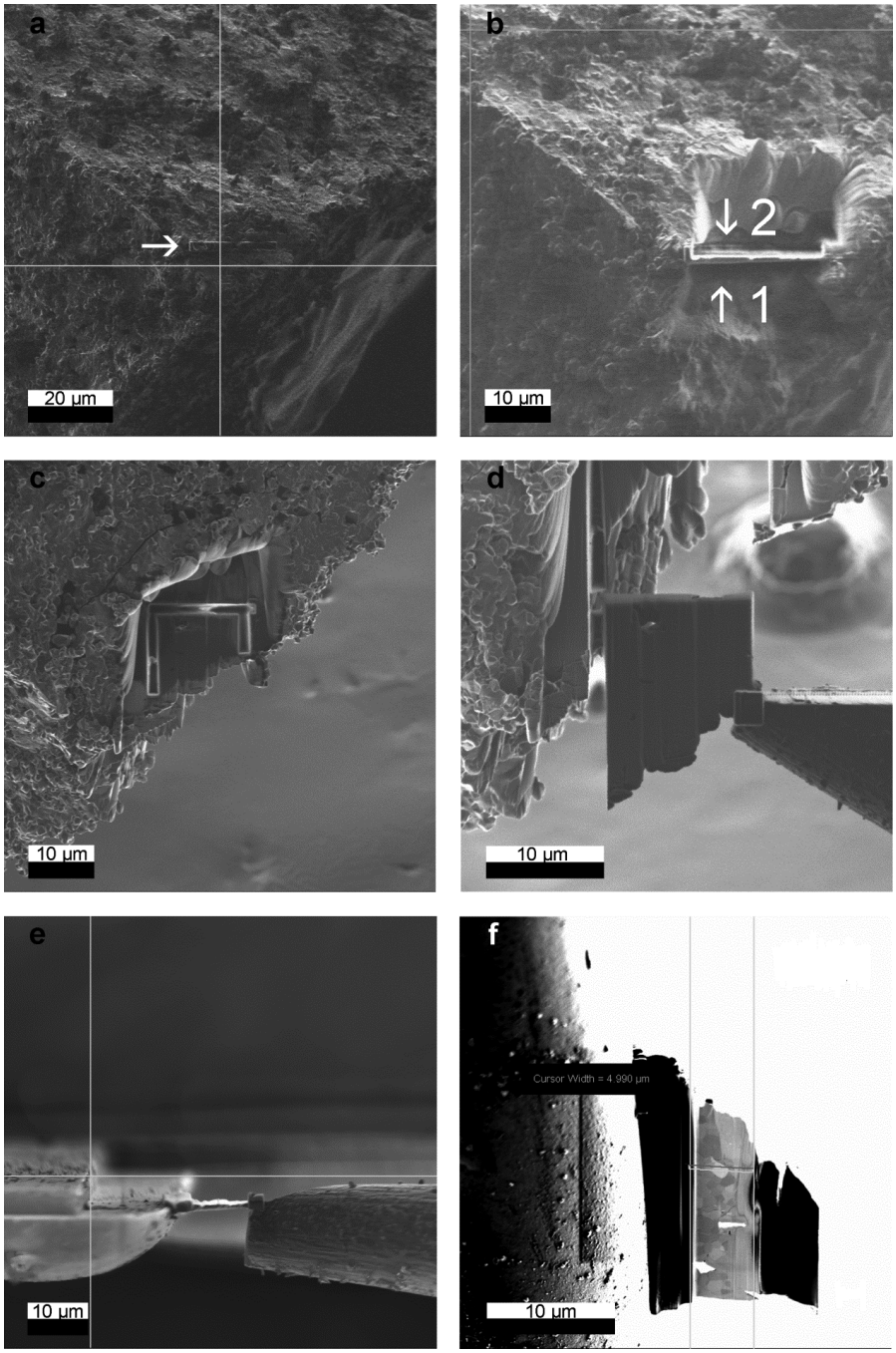

Figure 23: Preparation of a FIB lamella of a $Nd_2Zr_2O_7$ pyrochlore after dissolution: (a) carbon deposition to protect the surface; (b) clearance cutting; (c) "u-cut"; (d) lift out with micromanipulator; (e) fixation of the lamella to the TEM sample holder and (f) final lamella.

4.3.3 Electron microscopy

SEM and EDX - The SEM analyses were performed with a Quanta 200F from FEI which is equipped with a field emission cathode. The EDX detector is from EDAX company.
To analyse the samples by SEM and EDX they were prepared on sticky carbon pads which were glued to an aluminium sample holder. The SEM analysis was carried out under low vacuum. Therefore a coating of the samples was not necessary.

The Pu-pyrochlore pellet was measured with a JEOL 6490 LV. The pellet was coated with Au-Pd and fixed to an aluminium stub with conductive silver.

TEM - Electron diffraction pattern were acquired with a Philips EM420T microscope which operated at 120 kV with a camera length either being 480 mm or 660 mm. The EDX measurements were performed with a LINK Analytical eXL system (Oxford Instruments).
All samples which were characterised by TEM were obtained from fine fractions of the corresponding chemical compositions with a particle size below 50 µm. The powder was dispersed in acetone and set into an ultrasonic bath. After the sedimentation of the coarse fraction a spatula-point of the suspension was transferred into an agate mortar and was ground thoroughly under acetone. The suspension was dispersed one more time and several droplets were deposited at a TEM grid.

From the stoichiometric pyrochlore an electron beam transparent lamella (20 kV) was prepared with a FIB (section 4.3.1) and mounted on a TEM grid (Figure 24).

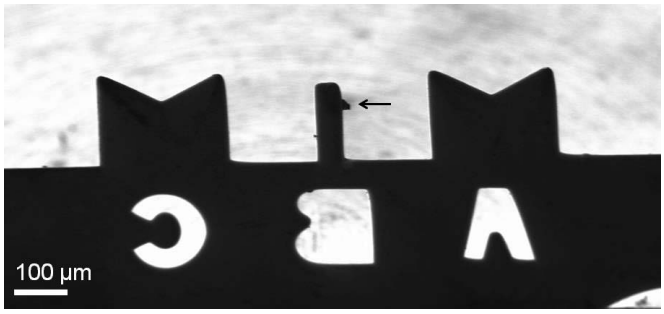

Figure 24: FIB lamella (indicated by the arrow) of a stoichiometric pyrochlore fixed to a TEM grid.

For the electron diffraction measurement the TEM grid was mounted on a specimen holder and inserted into the TEM.

An overview of all samples which were characterised by TEM is given below in Table 4.

Table 4: Overview of Nd_2O_3-ZrO_2 samples which were characterised by TEM.

Name	Nd_2O_3 content (mol%)	Chemical composition	Crystal structure*	Sample
SF-98	33.3	$Nd_2Zr_2O_7$	Pyrochlore	FIB lamella
SF-85	25.0	$Nd_2Zr_2O_7$	Pyrochlore	Powder
SF-83	15.6	$Nd_{0.94}Zr_2O_7$	Defect fluorite	Powder

* according to powder XRD measurements.

4.3.4 TRLFS

The experimental setup for TRLFS measurements consists of a pulsed excimer pumped dye laser. The required excitation energy is adjusted by a pair of cuvettes with a dye which is passed by the laser beam. The first cuvette is the oscillator whereas the second one is the amplifier. A wavemeter is used to monitor the adjusted wavelength. Before the laser is directed to the sample it passes a polarizing filter. For a better resolution of the emission spectra the sample is cooled to a temperature below 20 K in a vacuum chamber. The emitted fluorescence signal is detected with an optical multichannel analyser that consists of a polychromator with 300, 600 and 1200 lines/mm gratings and an intensified gated photodiode array. Figure 25 shows the Cm fluorescence signal of a $La_2Zr_2O_7$ pyrochlore sample.

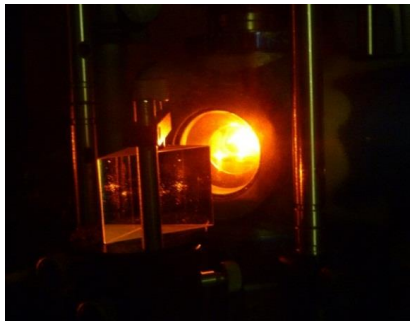

Figure 25: Cm fluorescence of a $La_2Zr_2O_7$ sample after direct excitation.

QUI was used as dye for the UV excitation measurements at 394 nm for europium and 396.6 nm for curium. Rhodamine 6G and Rhodamine B were used as dyes for the direct excitation spectra for europium and curium, respectively. The wavemeter Toptica WS7 allowed to adjust the wavelength with an accuracy $>10^{-5}$ nm. A thin layer of the powdered sample was prepared on a copper sample holder by a small amount of grease and mounted within the experimental setup.

4.3.5 BET

The surface area of the powders was determined via N_2-BET with a singlepoint Areameter (Ströhlein). About 1 g of each powder was used to determine the specific surface area via adsorption of the N_2 molecules.

4.3.6 Elemental analysis of aqueous solutions

Two different techniques were used for the analysis of aqueous concentrations of Nd, Zr, La and Eu. Inductively coupled plasma atomic emission spectrometry (ICP-OES) was used to determine the metal concentrations of stock solutions prior to the synthesis of ceramics. Inductively coupled plasma mass spectrometry (ICP-MS) was used for the macroscopic dissolution experiments. Due to the low release rates especially of Zr a method with a higher sensitivity for Nd and Zr than ICP-OES was needed to determine their aqueous concentrations.

ICP-MS measurements were performed with an Elan 6100 DRC which was developed by Perkin Elmer and SCIEX. The ICP-MS samples were diluted with suprapure water to a concentration of 1 – 10 ppb. The samples were acidified with 1 % HNO_3 suprapure.

ICP-OES measurements were performed with the ICAP6500 Duo from Thermo Scientific.

5 Results & discussion

Three main aspects of pyrochlores as potential nuclear waste forms were addressed in this study: (1) phase stability field of pyrochlore and consequence of non-stoichiometry, (2) structural uptake of radionuclides and (3) chemical stability and effect of phase transformation to defect fluorite.

5.1. Phase stability field of pyrochlore and consequence of non-stoichiometry

The structural changes due to the non-stoichiometry and implementation of mixed cationic sites were studied using XRD and TEM. XRD was used to study the long-range order and average structure of ZrO_2-Nd_2O_3 ceramics whereas TEM and TRLFS (in section 5.2.1) are techniques devoted to the local environment.

5.1.1 Powder diffraction: from stoichiometric pyrochlore to defect fluorite

Here, the structural transition from the stoichiometric pyrochlore to the defect fluorite structure is discussed as a consequence of mixed Nd and Zr occupancy of either the A or the B position within the pyrochlore. Figure 26a shows four representative powder XRD pattern of the samples with 18.6, 23.1, 33.3 and 43.7 mol% Nd_2O_3. All pattern were indexed as it is shown for a sample with the pyrochlore crystal structure (blue pattern) and for a sample where the defect fluorite and the pyrochlore crystal structure coexist (black pattern). The subscript P denotes pyrochlore whereas DF indicates samples with the defect fluorite structure.

Figure 26b – e show the (662) pyrochlore and (331) defect fluorite reflexes with the corresponding Gaussian fit functions. Figure 26b and e suggest the presence of two phases in the 18.6 and 43.7 mol% Nd_2O_3 samples. For the sample with the excess of Nd this is clearer, because the miscibility gap is much broader at this end of the pyrochlore solid solution than it is at the end with a Nd-deficit. Therefore, it is much more difficult to distinguish between the two phases at the lower Nd-content end. A systematic shift of the reflexes to smaller 2θ values can be observed for the samples with a higher Nd_2O_3 content (Figure 26a). This may be caused by the exchange of the smaller Zr^{4+} cation with the bigger Nd^{3+} cation and indicates a solid solution formation.

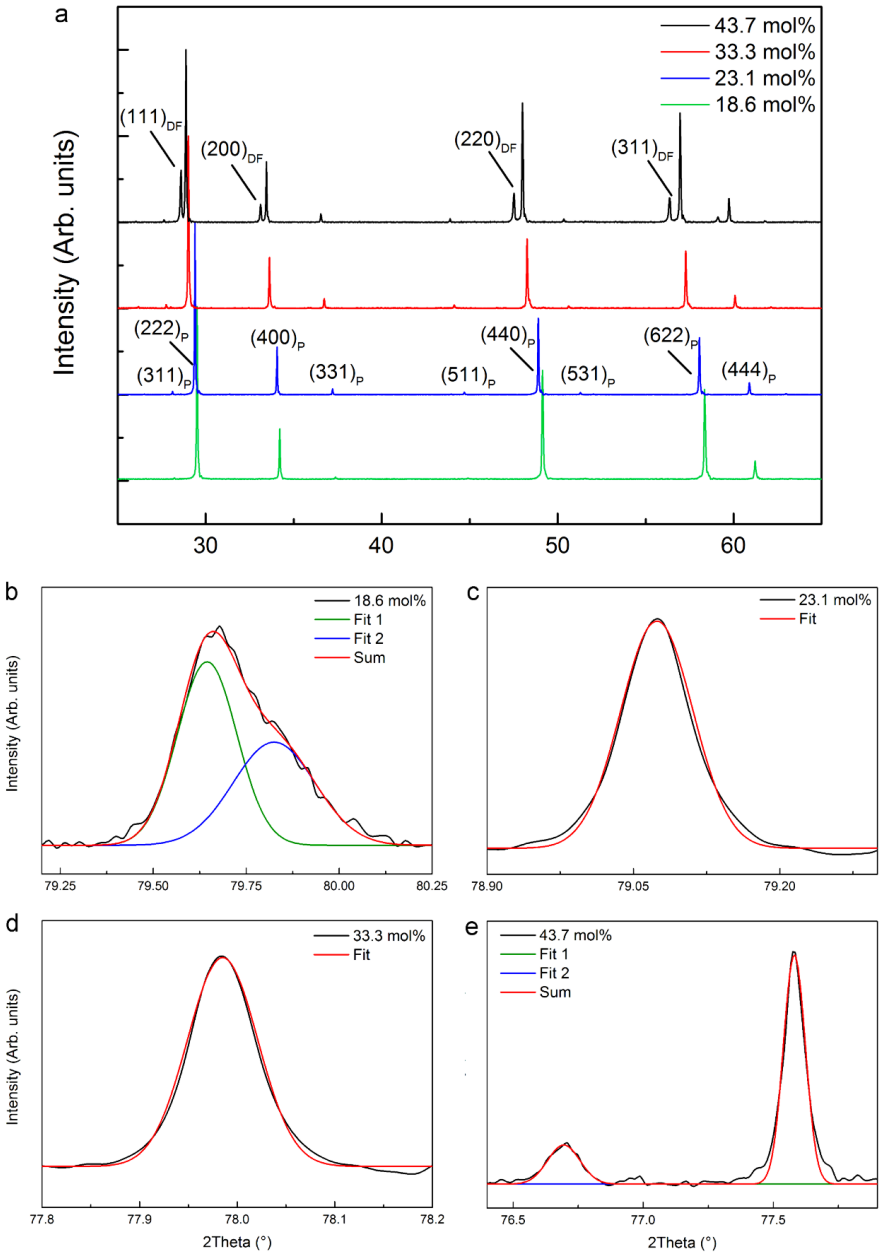

Figure 26: (a) Representative XRD pattern for four different chemical compositions in the Nd_2O_3 – ZrO_2 system with the pyrochlore or the pyrochlore and defect fluorite crystal structure. For a content of 18.6 mol% Nd_2O_3 (green) the defect fluorite and pyrochlore crystal structure coexist, whereas for 23.1 mol% Nd_2O_3 (blue) and 33.3 mol% Nd_2O_3 (red) single pyrochlore phases are obtained. For the sample with an excess of Nd (black curve) the pyrochlore and a defect fluorite structure coexist. For each of the four chemical composition of (a) in (b-e) the (662) pyrochlore and the (331) defect fluorite reflex are plotted with the corresponding Gaussian fit functions.

Lattice parameter and stability region of pyrochlore - In a first step the lattice parameter of the different samples was determined by the Nelson-Riley function (chapter 2.3.2). Figure 27 exemplarily shows the Nelson-Riley plot of a stoichiometric $Nd_2Zr_2O_7$ pyrochlore sample from which the lattice parameter is derived by linear regression.

Figure 28 shows the lattice parameter of the synthesised phases as a function of the Nd_2O_3 content. The filled red symbols correspond to samples which were synthesised within this work and sintered at 1600 °C for at least 5 h. The defect fluorite and pyrochlore crystal structure are very similar to each other (section 2.3.1). Therefore the lattice parameter was multiplied by two for samples with the defect fluorite structure in Figure 28 for a better comparison with the samples which have adopted the pyrochlore crystal structure. For the five compositions with 23.1, 25.0, 30.1, 33.3 and 35.1 mol% Nd_2O_3 a single phase material with the pyrochlore crystal structure was obtained. The lattice parameters are in good accordance with the literature data, except for the stoichiometric pyrochlore from Strakhov [100] which has a larger lattice parameter compared to the results of this work. The linear increase of the lattice parameter follows Vegard's law as the smaller Zr^{4+} cation is substituted by the bigger Nd^{3+} cation.

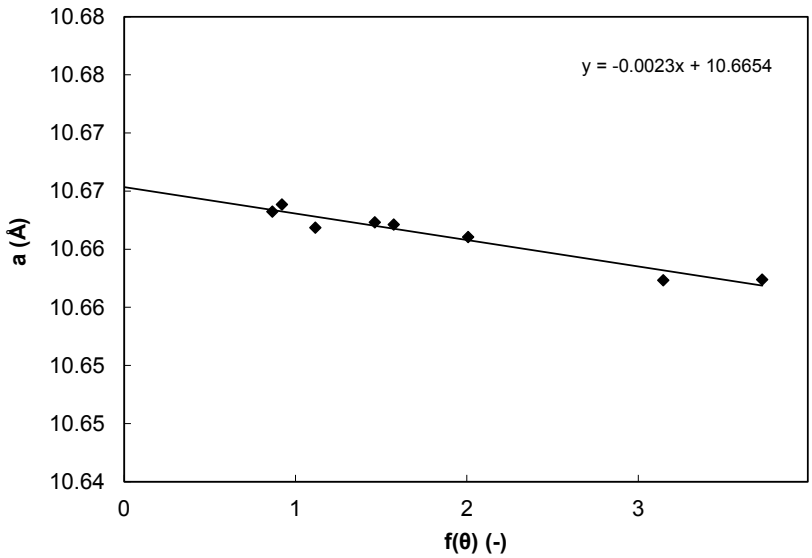

Figure 27: Nelson-Riley plot of a stoichiometric $Nd_2Zr_2O_7$ pyrochlore.

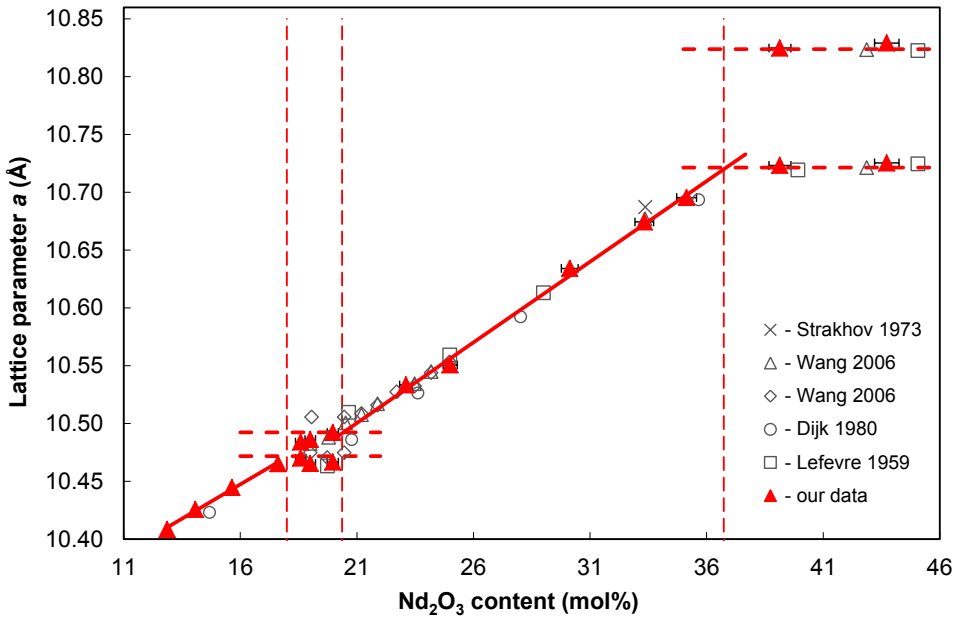

Figure 28: Lattice parameter *a* for various chemical compositions. The lattice parameters of the defect fluorite structure were multiplied by two for a better comparison with the pyrochlore samples. The vertical dashed lines indicate the phase boundaries of the pyrochlore crystal structure, as it was determined from the here synthesised samples which were sintered at 1600 °C for at least 5 h. The error in the direction of the axis of ordinates is within the size of the symbols.

The phase boundaries for the pyrochlore crystal structure were determined by the intersection of a linear fit function of the pyrochlore lattice parameters *a* with the line for the defect fluorite and pyrochlore samples in the miscibility gap for samples with either a Nd-deficit or an excess of Nd_2O_3 compared to the stoichiometric pyrochlore. A pyrochlore solid solution formation can be obtained in the range of 20.4 – 36.7 mol% Nd_2O_3. The phase boundaries are shown as vertical dashed lines in Figure 28. However, the slope of the defect fluorite samples with a Nd-deficit and the slope describing the pyrochlore region are equal within the limit of error (Figure 28). This might indicate, that there is no real miscibility gap but a rather gradual transition from the pyrochlore to the defect fluorite. This idea of a continuous transition between the pyrochlore and fluorite structure was recently proposed by Payne et al. [101]. A continuous transition of the pyrochlore to the defect fluorite was reported currently by Zhang et al. [102] on the basis of X-ray absorption near edge structure (XANES) data for compositional changes in $Y_2Sn_{2-x}Zr_xO_7$. Their XRD results match the above presented findings from powder diffraction which clarifies the need for several techniques taking different length scales into account to evolve a comprehensive structural understanding.

Detailed analysis of the pyrochlore XRD pattern – With the Hall-Williamson method which was introduced in section 2.3.2 the crystallite size and the lattice distortion was derived from the XRD pattern. Figure 29 shows the Hall-Williamson plot for three different samples. The first two samples (red) have both a content of 30 mol% Nd_2O_3 but different sintering durations. These two samples only differ in the crystallite size and a longer sintering duration leads to larger crystallite sizes (solid red triangles, S2). The slope of these lines is equal indicating that the sintering duration has no influence on the lattice distortion.

Additionally a sample with 39 mol% Nd_2O_3 content is plotted in Figure 29 (blue). This sample has an excess of Nd compared to the stoichiometric pyrochlore and besides the pyrochlore (solid blue triangles) the defect fluorite structure (open blue triangles) coexists. The linear fit functions of the pyrochlore as well as the defect fluorite both have steeper slopes than the ones of the 30 mol% Nd_2O_3 sample.

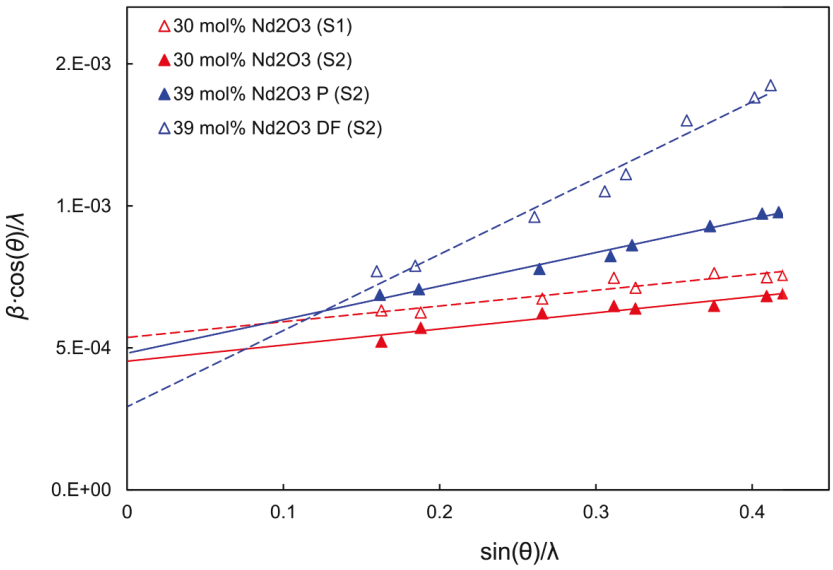

Figure 29: Hall-Williamson plot for three different samples. The samples with 30 mol% Nd_2O_3 differ in their sintering procedure and S1 corresponds to a sintering duration of 5 h at 1600 °C whereas S2 had a second sintering cycle of 10 h which gives an overall sintering duration of 15 h at 1600 °C (chapter 4.1.4). The sample with 39 mol% Nd_2O_3 was sintered for 15 h at 1600 °C and the defect fluorite and pyrochlore phase coexist.

Therefore, the lattice distortion of this sample is higher than observed for the 30 mol% sample. Moreover, the lattice distortion of the defect fluorite sample is nearly two times the value of the pyrochlore sample. The crystallite size for the defect fluorite sample is also much larger than for the pyrochlore sample. The changes in the crystallite size and the lattice distortion dependent on the chemical composition and the sintering duration S1 and S2 are summarised below.

Table 5: Crystallite size and lattice distortions derived with the Hall-Williamson method for samples with the pyrochlore crystal structure and samples where the defect fluorite and pyrochlore crystal structure coexist. The crystallite size and lattice distortions are compared for two different sintering durations at 1600 °C S1 and S2 (described in section 4.1.4).

		Sintering procedure S1		Sintering procedure S2	
Nd_2O_3 content (mol%)	Crystal structure	L (nm)	ε (%)	L (nm)	ε (%)
18.6	Defect fluorite	235 ± 27	0.043 ± 0.004	317 ± 40	0.040 ± 0.004
18.6	Pyrochlore	237 ± 18	0.038 ± 0.002	324 ± 42	0.038 ± 0.003
23.1	Pyrochlore	228 ± 12	0.027 ± 0.002	266 ± 13	0.025 ± 0.002
25.0	Pyrochlore	231 ± 10	0.024 ± 0.003	270 ± 7	0.020 ± 0.002
30.1	Pyrochlore	186 ± 10	0.014 ± 0.002	221 ± 10	0.014 ± 0.002
33	Pyrochlore	158 ± 7	0.008 ± 0.002	165 ± 9	0.011 ± 0.003
35.1	Pyrochlore	179 ± 9	0.017 ± 0.003	207 ± 7	0.016 ± 0.001
39.1	Pyrochlore	177 ± 10	0.022 ± 0.003	208 ± 8	0.030 ± 0.002
39.1	Defect fluorite	158 ± 10	0.035 ± 0.004	342 ± 55	0.067 ± 0.004

Additional annealing leads in any case to an increasing crystallite size.

Figure 30 depicts a detailed analysis of the XRD pattern.

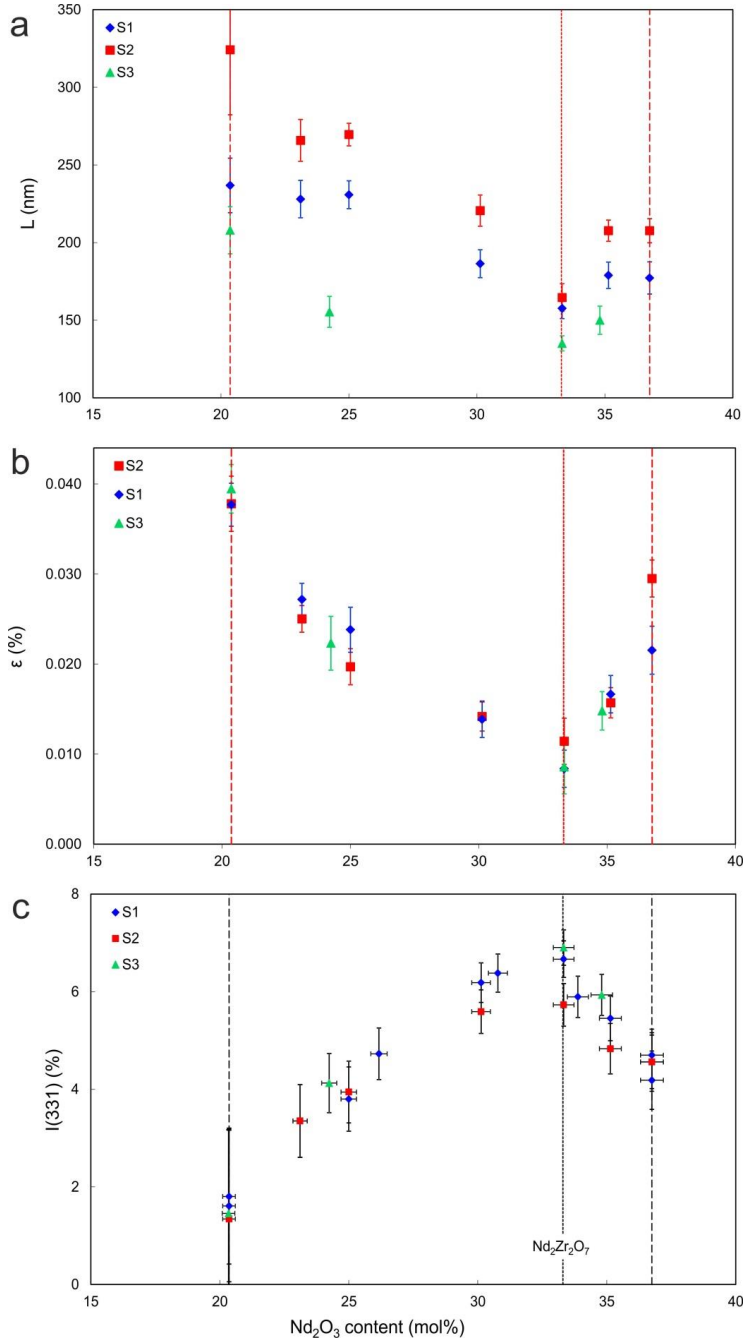

Figure 30: Detailed analysis of the powder XRD pattern: (a) dependence of the crystallite size L, (b) lattice distortions ε and (c) intensity of the (331) superstructure reflex on the chemical composition in the pyrochlore range. S1 (blue), S2 (red) and S3 (green) correspond to the different sintering procedures as described in the experimental part in section 4.1.4. The dashed lines indicate the pyrochlore phase boundaries.

As already mentioned in Table 5 the crystallite size is dependent on the sintering duration or rather the sintering procedure (Figure 30a). The general trend is consistent among all applied sintering procedures S1, S2 and S3. The crystallite size *L* shows a minimum in the case of a stoichiometric $Nd_2Zr_2O_7$ pyrochlore. Comparing Figure 30a and b the crystallite size increases with an increasing level of lattice distortions $<\varepsilon^2>^{0.5}$. Apparently, the occurrence of the microdeformations in the material promotes the growth of the domains. In contrast to *L* the values of the lattice distortions do not depend on the sintering procedures and these values are equal within the limits of the experimental error at fixed sample compositions. The lattice distortions dependence on the Nd_2O_3 content has a minimum of 0.01 % at the stoichiometric pyrochlore $Nd_2Zr_2O_7$. The level of $<\varepsilon^2>^{0.5}$ increases significantly with moving off the $Nd_2Zr_2O_7$ composition and was found to be ~ 0.04 % and ~ 0.025 % for the left and right pyrochlore phase boundaries, respectively. Apparently, the value of lattice distortions is greatly determined by the Nd_2O_3 content or the non-stoichiometry of the samples (Figure 30b).

Within the literature the positional parameter *x* is traditionally used as indicator of the pyrochlore structure stability [103-105]. The pyrochlore crystal structure can be fully described with the lattice parameter *a* and the positional parameter *x* which defines the position of the 48f oxygen due to the symmetric constraints of the structure. The additional ordering of the vacancies within the pyrochlore crystal structure compared to the defect fluorite causes further planes of reflection resulting in the superstructure reflexes for the pyrochlore. It was observed that the intensity of the superstructure reflections strongly depend on the Nd_2O_3 content.

For a detailed analysis of the pyrochlore phase stability field, here the $(331)_P$ reflex was chosen as indicator because it has no overlap with other reflexes and the highest intensity of all detected superstructure reflexes. The $(331)_P$ intensity was normalised to the strongest pyrochlore reflex intensity $(222)_P$. The $(331)_P$ reflex intensity as a function of the Nd_2O_3 content is presented in Figure 30c. The highest (331) intensity is observed for the stoichiometric pyrochlore $Nd_2Zr_2O_7$ (Figure 30c). The reflex intensities of samples with the same chemical composition but different sintering procedures are identical within the limit of error. Therefore, the (331) intensity is independent on the sintering procedure. Approaching the phase boundaries of the pyrochlore structure the (331) intensity decreases. This intensity decrease is not symmetrical to both sides of the stoichiometric pyrochlore. For the region with a Nd-deficit a less steep decrease for the intensity is observed than for the region with an excess of Nd. For the phase boundary of the pyrochlore with a Nd-deficit the intensity decreases to 1.6 % whereas the intensity for the phase boundary of the Nd- enriched pyrochlore decreases only to 4.5 %. These values are mean intensities for the various applied sintering conditions for the chemical composition at the two phase boundaries. The

less steep decrease of the samples with a Nd-deficit could indicate that a lattice compression may be easier than an expansion of the crystal lattice.

The dependence of the lattice distortions (Figure 30b) and the (331) intensity (Figure 30c) on the chemical composition are inverted with respect to the axis of ordinates. The correlation between these two parameters is shown in Figure 31. The non-symmetric dependence of the lattice distortions and the (331) intensity on the Nd_2O_3 content can be explained in this way: The lattice distortions $<\varepsilon^2>^{0.5}$ are mean-squared values and therefore always positive, whereas they do not reflect the direction of the deformation. The transition of the pyrochlore to the defect fluorite structure takes place at high levels of microdeformations (Figure 30b). Replacing part of the neodymium with the cation radius equal 1.109 Å [106] by the zirconium cation with the smaller radius 0.72 Å at the B position and 0.84 Å within an eightfold coordination as it is expected at the A position [106] leads to a compression of the crystal lattice. Correspondingly, the substitution of Zr^{4+} by Nd^{3+} at the B position leads to tensile stress within the crystal lattice.

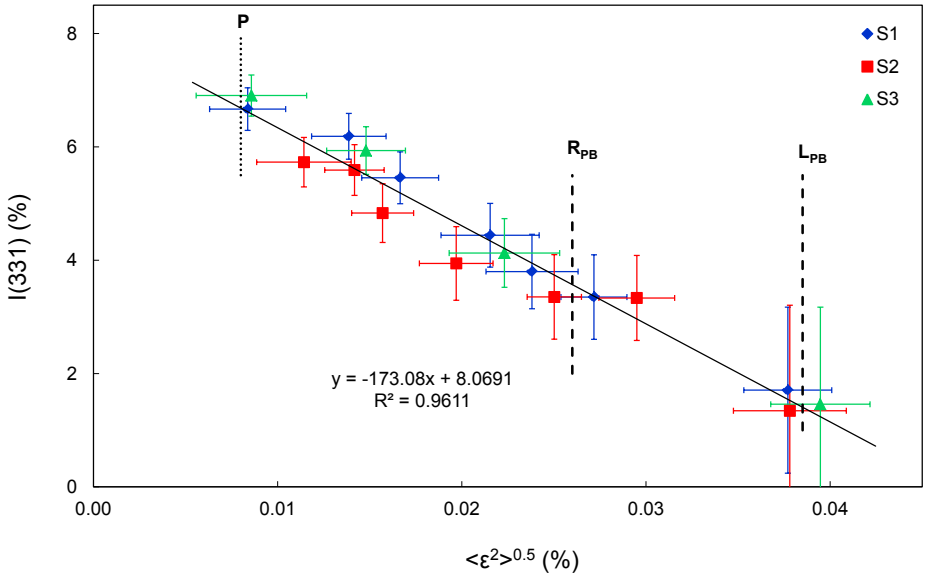

Figure 31: Correlation of the (331) intensity with the lattice distortion for various chemical compositions. The dotted line indexed as "P" corresponds to the stoichiometric pyrochlore. The dashed lines indexed "R_{PB}" and "L_{PB}" correspond to the left and right phase boundaries for the pyrochlore crystal structure in a Nd_2O_3-ZrO_2 system for a sintering temperature of 1600 °C.

The lattice distortions for the non-stoichiometric compositions with a Nd-deficit exhibit a less steep slope compared to the ones with surplus neodymium. Therefore, the crystal lattice seems to be more tolerant towards compressive stress, than to tensile stress and the region of the pyrochlore phase stability to the left from the stoichiometric composition $Nd_2Zr_2O_7$ is more elongated than to the right site.

5.1.2 The antisite exchange model – a first attempt to describe the non-stoichiometric pyrochlores

The structural changes of a stoichiometric pyrochlore to the non-stoichiometric pyrochlores as consequence of mixed Nd and Zr occupancy of the A or B site is described with the help of the antisite cation exchange model. The chemical composition of the ZrO_2 - Nd_2O_3 system can be expressed via:

$$\chi Nd_2O_3 + (1-\chi)ZrO_2 \rightleftharpoons Nd_{2\chi}Zr_{1-\chi}O_{2+\chi} \tag{28}$$

where χ is the mole fraction of the neodymiumoxide.

In case of the stoichiometric composition $Nd_2Zr_2O_7$, the number of cations with the coordination number eight (neodymium) and six (zirconium) for the A and B position are equal. For non-stoichiometric compositions to the left side of the $Nd_2Zr_2O_7$ an Zr excess exists and $\chi < 0.333$.

The antisite exchange model of the cations is a first attempt to describe these non-stoichiometric pyrochlores. Within this model the excess Zr cations are assumed to occupy the A position. The substitution of Nd by Zr is accompanied by a change of the coordination number for these Zr^{4+} cations from six to eight, which is the typical coordination number of the A position. Taking the occupancy of the A and B site into account the formula of the chemical composition (28) can be re-written as:

$$^{VIII}\left(Nd_{2\chi}Zr_{y1}\right)^{VI}\left(Zr_{1-\chi-y1}\right)O_{2+\chi} \tag{29}$$

where χ is the mole fraction of the neodymiumoxide and y1 the excess Zr amount compared to a stoichiometric pyrochlore. Assuming an equal occupancy of the A and B position leads to the following expression:

$$^{VIII}\left(Nd_{4\chi}Zr_{1-3\chi}\right)^{VI}\left(Zr_{1+\chi}\right)O_{2\chi+4} \tag{30}$$

The effective ionic radius r_{eff}(A) of the A site is calculated by the sum of the respective ionic radii for each cation present at the A position with the coordination number eight in the proportions given above (30):

$$r_{eff}(A) = \frac{4\chi}{1+\chi}\,{}^{VIII}r\left(Nd^{3+}\right) + \frac{1-3\chi}{1+\chi}\,{}^{VIII}r\left(Zr^{4+}\right) \tag{31}$$

Here, the effective radius for the left phase boundary of the pyrochlore crystal structure is calculated. The mole fraction of the Nd was determined to be $\chi = 0.204$ (section 5.1.1).

$$r_{eff}(A) = \frac{4\cdot 0.204}{1+0.204}\cdot 1.109\,\text{Å} + \frac{1-3\cdot 0.204}{1+0.204}0.84\,\text{Å} = 1.102\,\text{Å} \tag{32}$$

For the left region from the stoichiometric pyrochlore the B position is fully occupied by Zr cations with the coordination number six and therefore constant:

$$r(B) = {}^{VI}r\left(Zr^{4+}\right) = 0.72\,\text{Å} \tag{33}$$

The non-stoichiometric pyrochlore compositions with a neodymium excess ($\chi > 0.333$) accommodate the surplus neodymium at the B position. In this case, the coordination number of these neodymium cations decreases from eight to six for the neodymium at the B position. The formula of the chemical composition (28) can be re-written as:

$${}^{VIII}\left(Nd_{2\chi-y2}\right)\,{}^{VI}\left(Nd_{y2}Zr_{1-\chi}\right)O_{\chi+2} \tag{34}$$

where χ is the mole fraction of the neodymiumoxide and y2 the excess Nd amount compared to a stoichiometric $Nd_2Zr_2O_7$ pyrochlore. Assuming equal occupancy of the cationic A and B sites equation (34) can be converted to:

$${}^{VIII}\left(Nd_{\chi+1}\right)\,{}^{VI}\left(Nd_{3\chi-1}Zr_{2-2\chi}\right)O_{2\chi+4} \tag{35}$$

For these compositions, the A site is fully occupied by Nd cations with the coordination number eight.

$$r(A) = {}^{VIII}r\left(Nd^{3+}\right) = 1.109\ \text{Å} \tag{36}$$

For the cations on the B site the effective cation radius r_{eff}(B) can be expressed as the sum of the respective ionic radii of Zr and Nd cations with the coordination number six taking their content on the B position into account:

$$r_{eff}(B) = \frac{3\chi - 1}{1+\chi}\,{}^{VI}r\left(Nd^{3+}\right) + \frac{2(1-\chi)}{1+\chi}\,{}^{VI}r\left(Zr^{4+}\right) \tag{37}$$

The effective ionic radius of the B position at the right phase boundary of the pyrochlore is calculated below:

$$r_{eff}(B) = \frac{3\cdot 0.367 - 1}{1 + 0.367}\cdot 0.983\ \text{Å} + \frac{2\cdot(1-0.367)}{1+0.367}\cdot 0.72\ \text{Å} = 0.74\ \text{Å} \tag{38}$$

Figure 32a shows the effective ionic radii for the A and B position r_{eff}(A) and r_{eff}(B) for the different chemical compositions in the stability field of pyrochlore. The dashed vertical lines indicate the phase boundaries of the pyrochlore stability field and were experimentally determined as described in section 5.1.1. The depicted effective ionic radii at the phase boundaries were calculated in equations (32) and (38). The line of the effective ionic radius for the A position r_{eff}(A) to the left site of the stoichiometric pyrochlore is less steep than the line of the effective ionic radii at the B position r_{eff}(B) for the compositions with an excess of neodymium.

On the basis of the antisite exchange model the ratio of the ionic radii or rather effective ionic radii $r_{eff}(A)/r_{eff}(B)$ of the different chemical compositions are shown (Figure 32b). This empirical model correlates with the trend of the (331) intensity for a change in the chemical composition (Figure 30c). The slope of the non-stoichiometric pyrochlores with a neodymium deficit compared to the stoichiometric $Nd_2Zr_2O_7$ pyrochlore is less steep than for the region with a surplus of neodymium. This indicates that the compression of the crystal lattice seems to be easier than an expansion. It is important to keep in mind, that the antisite cationic exchange model is an empirical model which described the average structure which was also the case for the (331) intensity of the powder XRD pattern.

To gain insight into the local structure a different technique such as time resolved laser fluorescence spectroscopy or electron diffraction needs to be applied to a series of samples with different chemical compositions. TEM might be a suitable technique to probe if the

transformation of the pyrochlore to the stoichiometric pyrochlore to the defect fluorite exhibits a preferential direction or rather proceeds in the same way along all spatial directions.

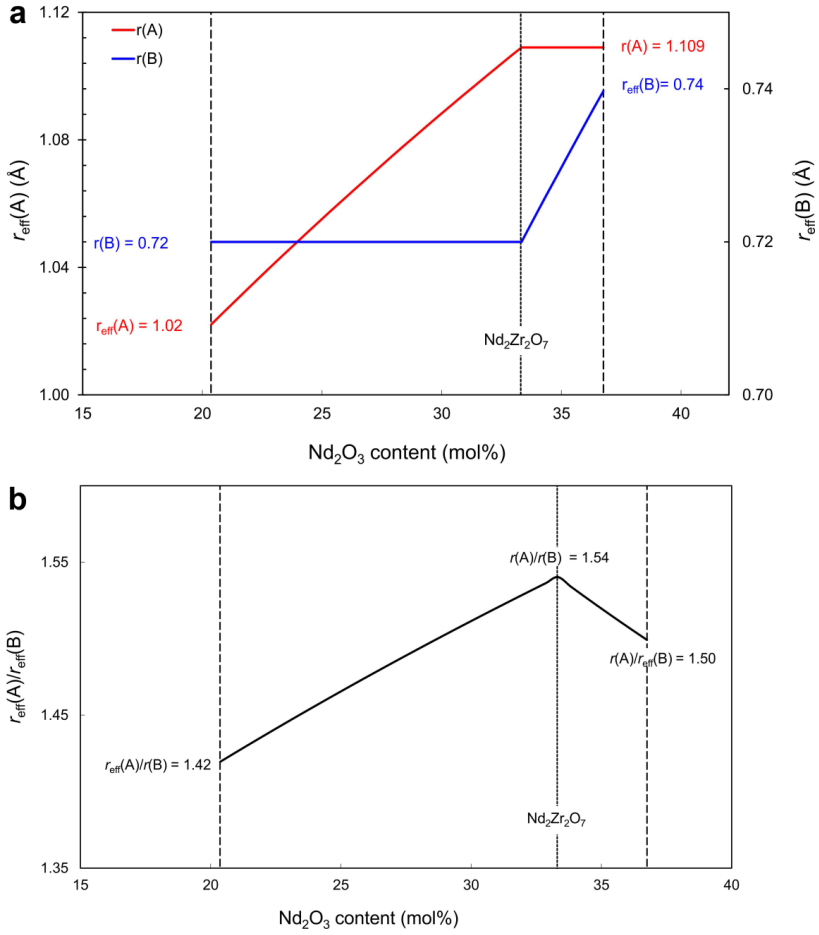

Figure 32: (a) Radii of the A (red) and B (blue) position and effective radii of the A and B position dependent on the chemical composition. The straight line of the A site with a Nd-deficit and of the B site with an excess of Nd correspond to the Nd^{3+} and Zr^{4+} radii in an eightfold or sixfold coordination, respectively. The effective radii were calculated on the basis of the antisite exchange model. (b) Dependence of the relative ionic radii $r_{eff}(A)/r_{eff}(B)$ on the chemical composition of the non-stoichiometric pyrochlores. The dotted line corresponds to the stoichiometric $Nd_2Zr_2O_7$ pyrochlore whereas the dashed lines indicate the phase boundaries of the pyrochlore stability field as they were determined in this work for a sintering temperature of 1600 °C (section 5.1.1).

5.1.3 Electron diffraction at ZrO_2 - Nd_2O_3 ceramics with the pyrochlore and defect fluorite crystal structure

The structural change from a stoichiometric pyrochlore to the defect fluorite was analysed in detail by TEM and electron diffraction at local sites of the sample. Therefore a stoichiometric pyrochlore, a pyrochlore with a slight Nd-deficit (25.0 mol% Nd_2O_3) and a defect fluorite sample with a content of 15.6 mol% Nd_2O_3 were characterised by electron diffraction (Figure 33). For all three samples electron diffraction pattern were recorded along the [110], [112] and [100] zone axes. In accordance to the work by Reid et al. [107] all diffraction spots were labelled G_F and indexed by the defect fluorite structure, which is indicated by the subscript F.

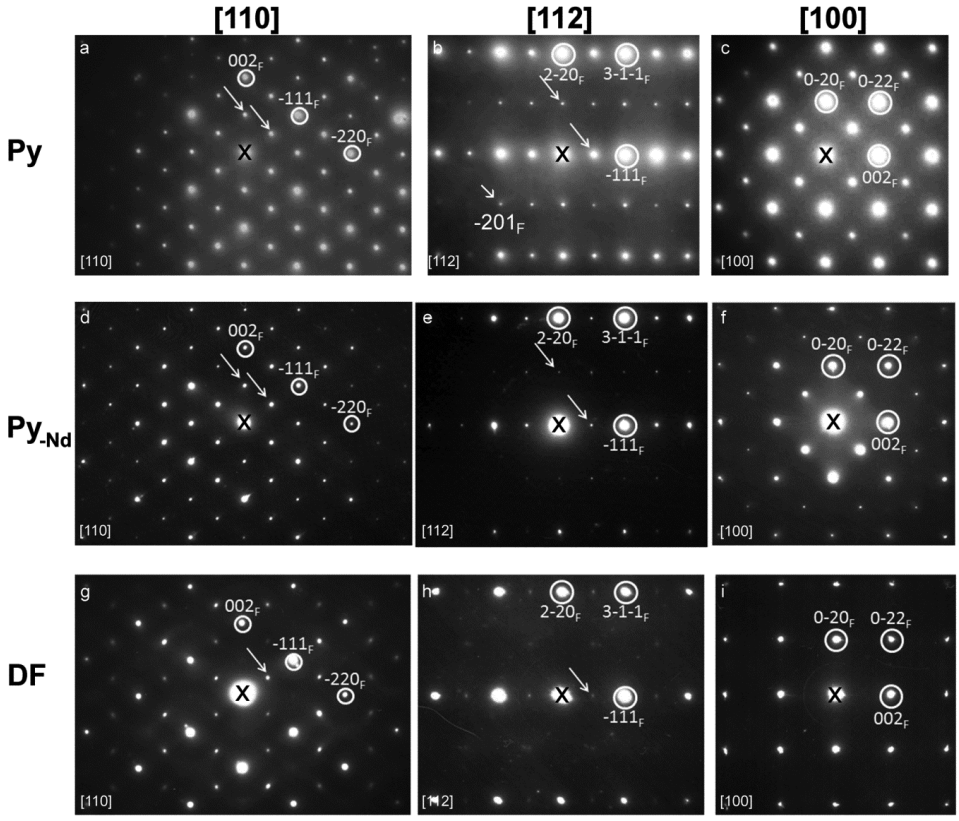

Figure 33: (a-c) Electron diffraction pattern along the [110], [112] and [110] zone axes of a stoichiometric pyrochlore, (d-f) a pyrochlore sample with 25.0 mol% Nd_2O_3 and (g-i) a defect fluorite sample with 15.6 mol% Nd_2O_3.

For a stoichiometric pyrochlore (Figure 33a - c) besides the typical electron diffraction pattern along the [110] axis (Figure 33a) a diffraction spot $G_F \pm ½ (002)_F$ is present. This diffraction spot neither belongs to the pyrochlore nor to the defect fluorite structure. It is most likely caused by a break of the symmetry in the pyrochlore crystal structure due to cation or anion disorder. A cationic disorder process could be evoked by a partial swap of Nd and Zr cations. Anionic disorder could be induced by a fractional occupancy of the normally vacant 8a site in the ideal stoichiometric pyrochlore by oxygen. The oxygen could either move from an occupied 48f or 8b site to the 8a site. The degree of disorder causing the $G_F \pm ½ (002)_F$ diffraction spot is most likely attributed to anionic disorder, because oxygen would be easier to move to an already vacant site whereas the movement of two cations for a cationic swap seems less favourable from an energetic point of view. Moreover, partial 8a occupancy inserts a negatively charged ion into the tetrahedral site formed of four positively charged Zr-sites which seems to be electrostatically reasonable. Preliminary results of quantum-mechanic calculations by Piotr Kowalski [108] indicated lower defect formation energies of an oxygen vacancy formation due to the movement of an oxygen to a usually vacant 8a site than the formation of a cationic swap. This would be consistent with the findings of Ubic et al. [109] who reported a small degree of anionic disorder by electron and neutron diffraction data for a stoichiometric $Nd_2Hf_2O_7$ pyrochlore.

The diffraction pattern along the [112] zone axis (Figure 33b) show all typical pyrochlore diffraction spots. Additionally the forbidden $G_F \pm ½ (201)_F$ diffraction spots are present. The reason for these diffraction spots remain unclear and will be part of future combined experimental and theoretical electron diffraction studies on the $ZrO_2 – Nd_2O_3$ system. The pattern along the [100] axis (Figure 33c) are consistent with the theoretical pyrochlore diffraction images. Generally the pyrochlore superstructure reflexes are less intense than the reflexes of the defect fluorite substructure.

The electron diffraction pattern of a pyrochlore with a slight Nd-deficit are shown in Figure 33d – f. Along the [110] axis (Figure 33d) the same diffraction pattern are present whereas a decrease in intensity becomes obvious compared to the stoichiometric pyrochlore pattern (Figure 33a). The $G_F \pm ½ (002)_F$ diffraction spot is again present as well as the $G_F \pm ½ (111)_F$. The latter diffraction spot comprises of Nd and Zr contributions [110]. A characterisation along the [112] zone axis (Figure 33e) still shows the typical spot pattern of a pyrochlore, whereas the superstructure reflections are much weaker than it was the case for the stoichiometric pyrochlore. Compared to the stoichiometric pyrochlore a part of the Nd^{3+} cations was replaced by the Zr^{4+} cations within this sample. The change in intensity might also be caused due to the different scattering factors of both elements which is part of the structure factor. In general a decrease in the cation and anion order is expected to lead to

weaker diffraction spots. The intensity decrease was also found along the [100] axis (Figure 33f).

The diffraction pattern along the [110] zone axis of a defect fluorite sample with 15.6 mol% Nd_2O_3 (Figure 33g) differ from the above discussed spot pattern of the pyrochlores. The superstructure reflexes $G_F \pm ½ (111)_F$ are still present probably because of the retention of cationic order. The $G_F \pm ½ (002)_F$ reflexes along the [110] zone axis are no longer present within this defect fluorite sample. In [112] direction (Figure 33h) the superstructure diffraction spots of pyrochlore are hardly present any longer. Along the [100] zone axis (Figure 33i) the spot pattern correspond to a defect fluorite structure and no superstructure reflections are present.

The change of brightness and intensity up to the complete absence of superstructure diffraction spots was shown to be a gradual process which occurs differently along the diverse zone axes starting from a stoichiometric pyrochlore and moving forward to a defect fluorite sample according to the powder XRD measurements. The evolution of these changes indicates a continuous transition of the pyrochlore to the defect fluorite structure.

Besides the electron diffraction pattern bright field and dark field images were taken of the FIB lamella of the stoichiometric pyrochlore .The BF image of part of the stoichiometric pyrochlore lamella showed mottled grains (Figure 34).

Figure 34: BF image of a grain of the stoichiometric pyrochlore lamella. This grain was characterised by EDX and is referred to as grain 2 in Table 6.

Table 6: Zr/Nd ratios for six different grains of a stoichiometric pyrochlore. At grain 1 and 2 the Zr/Nd ratio was measured at several positions. The Zr/Nd ratio depicts the ratio of intensity of the Zr L_α line and Nd L_α line.

Location	Zr/Nd ratio (-)
Grain 1, grain boundary	1.14
Grain 1, center	1.19
Grain 2, grain boundary	1.63
Grain 2, 1/3 from the grain boundary away	1.68
Grain 2, 2/3 from the grain boundary away	1.35
Grain 2, center	1.33
Grain 3	1.20
Grain 4	1.15
Grain 5	0.98
Grain 6	0.91

This may be taken as an indication for chemical inhomogeneity of the grain. Therefore several grains were probed by EDX and the resulting Zr/Nd ratios are given in Table 6. The Zr/Nd ratio was built from the intensity of the Zr L_α line at 2.042 keV and the Nd L_α line at 5.229 keV. Theoretically the ratio should be unity for a stoichiometric pyrochlore. However, between different grains the ratio has a relatively large variety between 0.91 and 1.68 Zr/Nd. For grain 1 and grain 2 the chemical composition was probed at the grain boundary and in the center of the grain to look for a Zr- or Nd-enriched zone at the outer part of the grain. The Zr/Nd ratios prove that there is no systematic enrichment of one sort of cation at the outer sphere of the grains and the chemical variation lies within the general fluctuations.

5.2. Radionuclide uptake

5.2.1 Structural investigation of Ln, An-pyrochlores by TRLFS

In contrast to powder XRD which is a bulk method, Raman, X-ray absorption fine structure (XAFS) and luminescence spectroscopy are techniques to gain insight into the local structure of crystalline materials. To identify which cationic site of a pyrochlore is adopted by the actinide, TRLFS is an ideal method, because the emission spectra give information of the direct environment of the probed dopant. Here, Cm and Eu as actinide surrogate were used in the $Ln_2Zr_2O_7$ system. Neodymium is substituted by lanthanum, because Nd was found to quench the fluorescence signal.

All discussed TRLFS results are published in Holliday, Finkeldei et al. (2013) [111].

Europium doped defect fluorite - After UV excitation of the Eu doped defect fluorite sample the presence of two $^5D_0 \rightarrow {}^7F_0$ bands around 576 nm and 580 nm indicated the presence of more than one Eu species (Figure 35a). To study both species separately, direct excitation spectra were recorded (Figure 35b). For the species excited at 579.6 nm the $^5D_0 \rightarrow {}^7F_1$ transition showed a threefold splitting and the $^5D_0 \rightarrow {}^7F_2$ transition a fivefold splitting, which is indicated by the vertical lines in Figure 35.

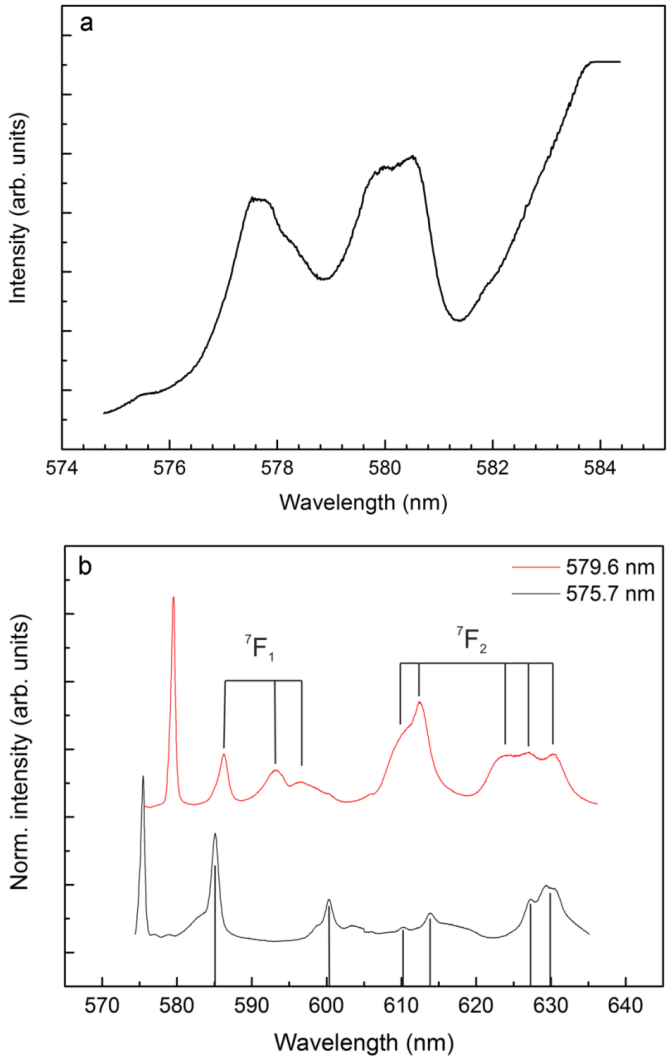

Figure 35: (a) Emission spectrum after UV excitation of a Eu doped $La_2Zr_2O_7$ defect fluorite sample; (b) emission spectra after direct excitation to the $^5D_0$ band. The major species is shown in red whereas the minor species is shown in black.

This is the maximum allowed splitting. This splitting indicates a low symmetry for the Eu environment. However, for the defect fluorite structure it is not possible to analyse if this splitting corresponds to an Eu species at an interstitial of low symmetry or at a regular lattice place with vacancies in the close surrounding. The fluorescence lifetime was detected to be relatively short at 1 ms. This lifetime corresponds to less than one water molecule in the direct surrounding of the Eu species according to Horrocks' equation [45]. Due to the sintering temperature of 1000 °C and the sintering duration the Eu was expected to be incorporated into the crystal structure. Therefore the lifetime and the absence of water molecules are consistent with the expectations for this sample and do not indicate the formation of a sorption species. The minor species within the defect fluorite sample shows less splitting than the major species. A rough quantification of the portions for the major and minor species can be derived from the fitted UV lifetime measurements. Approximately 5 % of the Eu corresponds to the minor phase excited at ~576 nm, which is described in detail in the section about the Eu pyrochlore samples. This species had a lifetime of 3.6 ms.

Europium doped pyrochlore - The Eu doped $La_2Zr_2O_7$ sample with the pyrochlore crystal structure was studied by UV excitation. A lifetime measurement from the UV excitation is shown in Figure 36a. The non-linear decay indicates the presence of more than one Eu species, as it was the case for the defect fluorite sample. The UV lifetime measurement was attributed to about 30 % of Eu for the minor species at 578.7 nm.

A direct excitation of the major Eu species to the $^5D_0$ band at 575.6 nm is shown in Figure 36b (solid line). This species had a two- and fourfold splitting for the $^5D_0 \rightarrow {}^7F_1$ and $^5D_0 \rightarrow {}^7F_2$ transition, respectively. The lifetime was measured to be 4.0 ms. The minor species of the defect fluorite sample is shown as dashed line in Figure 36b and shows exactly the same splitting. Moreover, the lifetime was 3.6 ms which is the same within the experimental error as for the major Eu species in the pyrochlore.

Eu is expected to have adopted the 16d site in the pyrochlore crystal structure. An assignment of the splitting to the symmetry by the Görller-Wallrand Binnemans table [112] is not possible here, because isocentric point groups like D_{3d} present at a 16d position are not included in this table. However, the observed two- and fourfold splitting for the Eu species after direct excitation in the pyrochlore are consistent with the results of Hirayama [113]. Within his article he attributed these splittings to the D_{3d} symmetry as present at the A position of the pyrochlore. The suppression of the F_2 transition is also consistent with a centrosymmetric symmetry. This confirms the localization of the major Eu species at the A position in the pyrochlore crystal structure.

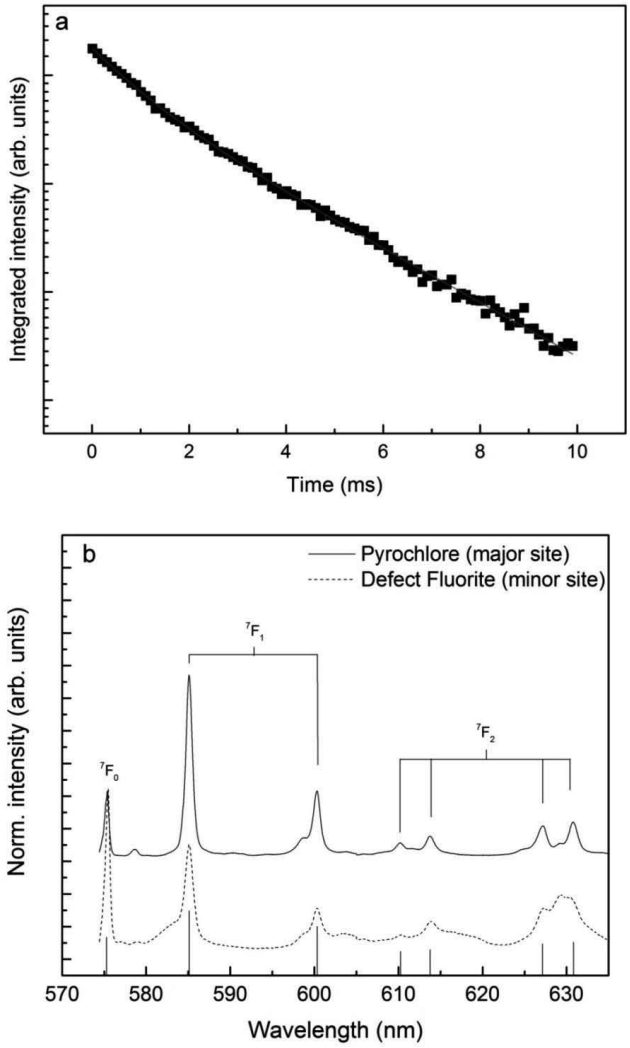

Figure 36: (a) UV lifetime measurement of Eu doped $La_2Zr_2O_7$ with the pyrochlore crystal structure. The red line shows the bi-exponential fit of the experimental data (black). (b) Emission spectra after direct excitation of Eu to the $^5D_0$ band. The solid line shows the emission spectra of the major species in the pyrochlore sample whereas the dashed line shows the emission spectra of the minor Eu species in the defect fluorite $La_2Zr_2O_7$ sample.

For the minor Eu species no separated emission spectra after direct excitation could be recorded. The reason might be the appearance of energy transfer processes with the major species. However, the lifetime of the minor species was determined to be 1.1 ms. This is identical to the major species in the defect fluorite.

In summary a small part of the Eu in the pyrochlore sample has not adopted the pyrochlore environment. Instead this Eu species has retained the defect fluorite environment. The lifetime is also consistent with the lifetime of the major Eu species in the defect fluorite sample; however, this species is not well defined due to the random oxygen vacancies in the nearest neighbour environment. The same can be found for a minor species in the defect fluorite structure, which has already adopted the pyrochlore environment. In the XRD measurements the samples were phase pure and no indications of these findings were present, whereas the TEM results match these observations.

Curium doped defect fluorite - One of the advantages of Cm is the very high sensitivity of TRLFS for this element. Therefore only trace amounts were needed in the $La_2Zr_2O_7$ samples. The measurements of these samples expand the TRLFS studies to actinide bearing compounds. This is an important step for ceramics which may find application as nuclear waste forms.

The UV excitation at 396.6 nm showed at a first glance two broad peaks around 634 nm and 639 nm (Figure 37a, black spectrum). With a higher grating of 1200 l/mm (red spectrum) the first broad peak deconvoluted to a triplet. These peaks are highly bathochromic shifted. Usually fluorescence bands of Cm after UV excitation are expected in the region between 595 – 615 nm. Contributions of any impurities which might cause this drastic shift can be excluded, because chemicals of high purity were used for the synthesis of the measured samples. The emission spectrum after UV excitation of the pyrochlore sample is shown for comparison in Figure 37b.

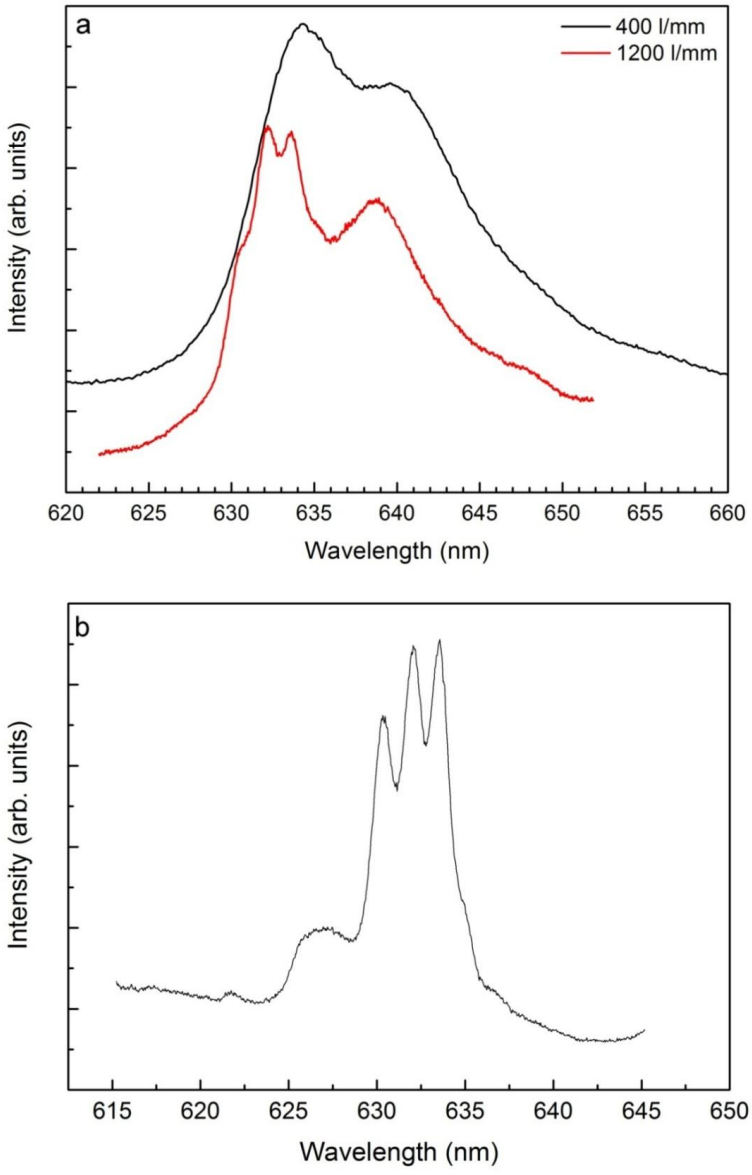

Figure 37: (a) Emission spectra of Cm doped $La_2Zr_2O_7$ sample with the defect fluorite structure. The black spectrum was recorded with a 400 l/mm grating whereas the red one was recorded with a higher grating of 1200 l/mm; (b) UV excitation spectrum for the pyrochlore sample.

To probe the different Cm species direct excitation spectra were recorded. The direct excitation spectrum with an excitation wavelength of 636.5 nm is shown in Figure 38, which led to a narrow peak. Further direct excitation spectra were taken at excitation wavelength around 636.5 nm. All resulted in a narrow single peak, similar to the one shown for 636.5 nm. Within a fluorite structure the cationic position would be eightfold coordinated. For the defect fluorite structure part of the oxygen is substituted by oxygen vacancies which are introduced randomly. This leads to various similar cationic positions which are very likely to cause this multitude of similar single peaks. The lifetime of the representative Cm species at 636.5 nm was measured to be 0.38 ms.

The triplet was directly excited at every site 630.5 nm, 632.4 nm and 633.4 nm. All emission spectra were the same. This can be taken as a evidence for the presence of just one Cm species with a threefold splitting. Additionally the lifetime measurements resulted in the same lifetimes of 1.1 ms for each peak. Therefore, the triplet was the result of the ground state splitting of the $^8S_{7/2}$ level. This was found to be the minor species with a Cm fraction of about 35 % in the defect fluorite. The triplet confirmed the replacement of La^{3+} by Cm^{3+}, because a splitting of the $^8S_{7/2}$ ground state which is less than fourfold is only caused by the presence of isocentric symmetry [47] as it is the case for the 16d site in the pyrochlore.

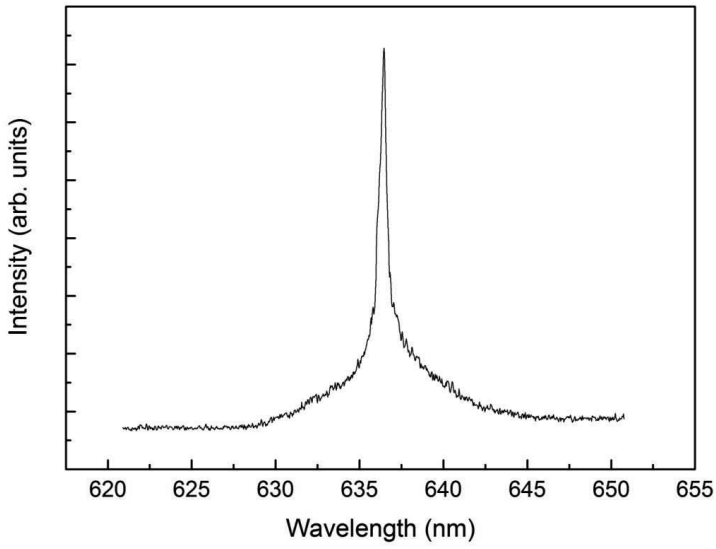

Figure 38: Emission spectrum of the major Cm species after direct excitation to the $^6D_{7/2}$ band in $La_2Zr_2O_7$ with the defect fluorite crystal structure.

Curium doped pyrochlore - The UV excitation spectrum for the pyrochlore sample is shown in Figure 37b. The same triplet is present as it was the case for the defect fluorite sample. Moreover, the broad peak is observed, but shifted to a smaller wavelength. To support the idea that the triplet was caused by the ground state splitting of the $^8S_{7/2}$ direct excitation measurements were performed at every peak of the triplet. The corresponding emission spectra are shown in Figure 39. Exciting at every peak led to the same emission spectrum for each site. The tip on top of the excited triplet site is an artifact (laser peak) due to an insufficient gate delay.

Lifetime measurements of the Cm fluorescence after direct excitation are depicted in Figure 40. Each site of the triplet showed the same lifetimes of 1.0 ms. The broad peak at 625.9 nm overlaps with the triplet and has a small contribution to the fluorescence lifetime of the triplet which explains the slight deviation from a mono-exponential decay. Approximately 85 % of the Cm shows the triplet splitting is attributed to the pyrochlore environment. The minor Cm species itself had a very short lifetime of 0.16 ms.

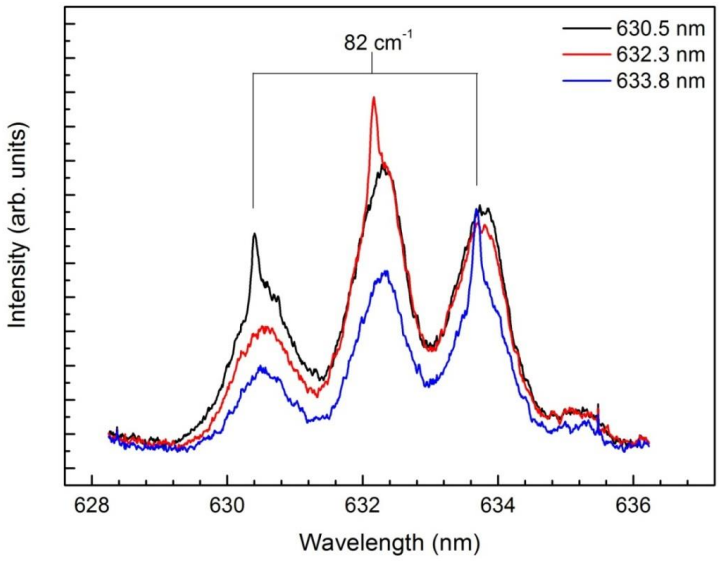

Figure 39: Fluorescence spectra of the triplet after direct excitation at each peak of the triplet. The tips on top of the excited triplet site can be attributed to a laser peak.

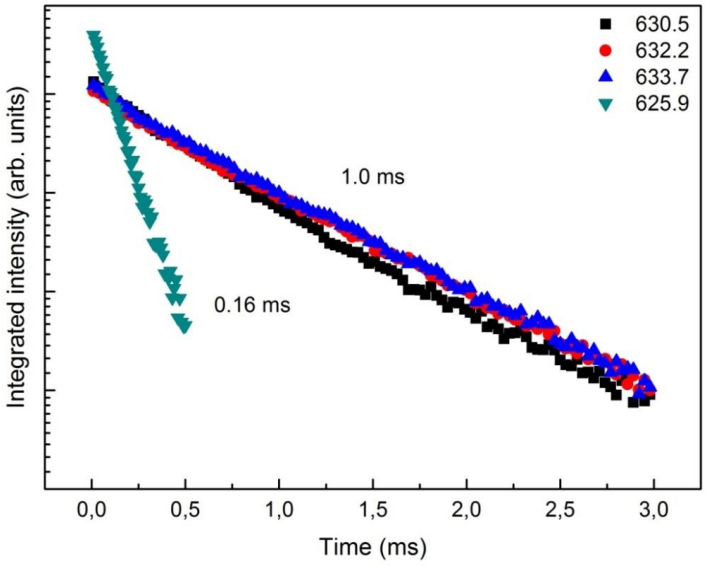

Figure 40: Lifetime measurements of Cm doped $La_2Zr_2O_7$ with the pyrochlore crystal structure. The longer fluorescence lifetime of 1.0 ms corresponds to the triplet with the peaks at 630.5 nm, 632.3 nm and 633.7 nm. The shorter lifetime is observed for the minor Cm species.

According to the Kimura equation [46] this corresponds with the presence of 3.2 water molecules in the first coordination sphere. This differs from the calculations for this species in the defect fluorite sample. The pyrochlore sample was heated to a higher temperature than the defect fluorite sample. This short lifetime might therefore be explained by an energy transfer process rather than the presence of water molecules. All positions, lifetimes and number of water molecules for the TRLFS measurements are listed in the appendix in Table 14.

The Cm fluorescence spectra confirmed the results from the Eu doped $La_2Zr_2O_7$ defect fluorite and pyrochlore samples. In both cases two species were observed in the pyrochlore and the defect fluorite structure. The major species that occured in the pyrochlore structure is already obtained as minor species in the defect fluorite samples. Vice versa the major species of the defect fluorite structure is retained as a minor species in the sample with the pyrochlore crystal structure.

ZrO_2 based pyrochlores are expected to undergo a phase transition as a consequence of radiation damage. Due to the possibility to distinguish between the species in the two different crystal structures, TRLFS might be developed to become a tool for the quantification of radiation damage for these pyrochlores with a high sensitivity.

5.2.2 Structural uptake of Pu-239

The $Pu(NO_3)_4$ was dissolved in 1 M HNO_3 as a first step, prior to precipitation of the hydroxides. Toth et al. [50] report the presence of a Pu(IV) species if 0.05 mol/L $Pu(NO_3)_4$ are dissolved in 0.11 M HNO_3. Due to disproportionation reactions they found further Pu species to be present in the solution. Calculations of the thermodynamic equilibrium Pu species with GEMS using the NAGRA-PSI database [95] were carried out according to the experimental conditions of Pu-syn-1 and Pu-syn-2 in the presence of 1 kg water. The results indicated the presence of an aqueous plutonyl species PuO_2^{2+} as predominant. It has to be considered, that the GEMS calculations can only predict the thermodynamic equilibrium but not include any kinetic effects of the reaction.

Clark et al. describe in their chapter about Plutonium [114] that in contact with oxygen Pu(IV) is thermodynamically unstable. However, the rate for this reaction is found to be negligible [114]. Glazyrin et al. [115] report the slow oxidation of Pu(IV) to Pu(VI) in 1-5 M HNO_3 at 90 °C. Here, the Pu solutions were freshly prepared for each synthesis. Therefore the presence of Pu(VI) is unlikely.

The disproportionation reaction of Pu(IV) in acidic solutions is given by:

$$3Pu^{4+} + 2H_2O \rightleftharpoons 2Pu^{3+} + PuO_2^{2+} + 4H^+ \quad (39)$$

The disproportionation reaction depends on the fourth order of $[H^+]$ and is implausible under strong acidic conditions. There was no experimental observation reported on the disproportionation of Pu(IV) under strong acidic conditions [114].

Here, the dissolution of $Pu(NO_3)_4$ in 1 M HNO_3 at room temperature is assumed to result in a Pu(IV) solution. However, the oxidation state in solution is not thought to be critical for the final oxidation state of Pu in the pyrochlore ceramic, due to sintering under reducing conditions.

In the first and second synthesis approaches, Pu-syn-1 and Pu-syn-2, the plutonium hydroxides were precipitated prior to the Zr and Nd hydroxides (Figure 41a). The coprecipitation of Nd and Zr hydroxides was already described in detail in section 2.2.1 and transferred to these synthesis routes. A prior precipitation of the plutonium hydroxide was carried out to study this formation separately.

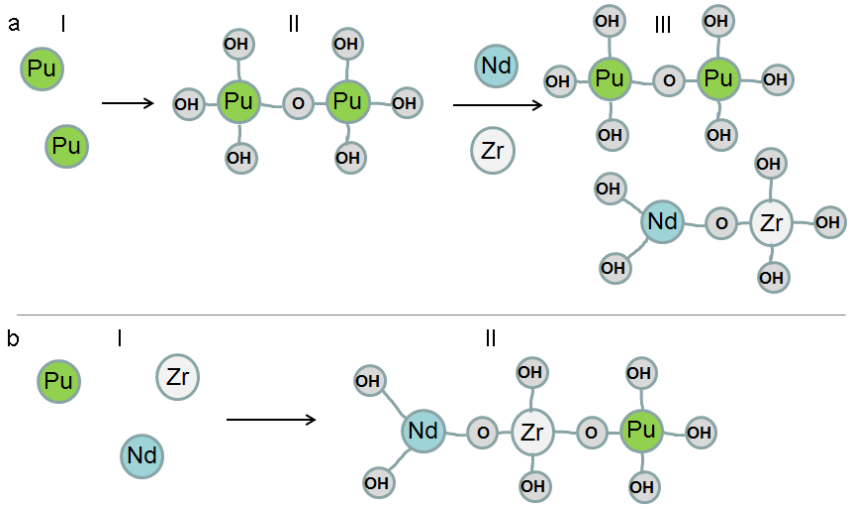

Figure 41: Schematic precipitation mechanism of (a) plutonium hydroxide formation and adjacent coprecipitation of Nd- and Zr-hydroxides; (b) coprecipitation of Pu-, Nd- and Zr-hydroxides leading to a mixed precipitate of all cations at the atomic scale.

The dissolution of the green solid $Pu(NO_3)_4 \cdot 5H_2O$ in nitric acid led to a dark green solution. Due to the dark colour the presence of a remaining solid was not seen, which could be PuO_2. The dissolution of $Pu(NO_3)_4 \cdot 5H_2O$ is expected to result in a Pu(IV) solution which has usually a brownish colour. A formation of a plutonium nitrate complex could also be possible which has a green colour [53]. Within the first synthesis Pu-syn-1 the calcination step was carried out under argon atmosphere. The crystallisation of PuO_2 within an oxalate precipitation route is given in the literature in the temperature range of 500 – 800 °C [116]. As the crystallisation of PuO_2 might already start at the here applied calcination conditions of 600 °C, within the second synthesis Pu-syn-2, the calcination was carried out at reducing conditions like the sintering step. The precipitation of these synthesis routes is schematically shown in Figure 41a. Again the possibility of the formation of two different precipitates arises as it was the case for the pure ZrO_2 - Nd_2O_3 pyrochlores in section 2.2.1. As Pu hydroxides have a strong tendency to form PuO_2 the presence of a separated Pu precipitate might facilitate the crystallisation of PuO_2 in a cubic crystal structure. Once the plutonium dioxide is formed it will most likely not be reduced during the sintering step to Pu(III) and be uptaken within the pyrochlore crystal structure as it is very stable in the cubic phase.

Therefore the synthesis route was enhanced to a coprecipitation of all three hydroxides (Figure 41b) within the Pu-syn-3 approach. Prior to the precipitation the solution of Pu, Nd, and Zr in nitric acid was homogenised. This approach might enable the formation of a coprecipitate of Pu-, Nd- and Zr-hydroxides which has a homogeneous distribution of the different cations at the molecular level.

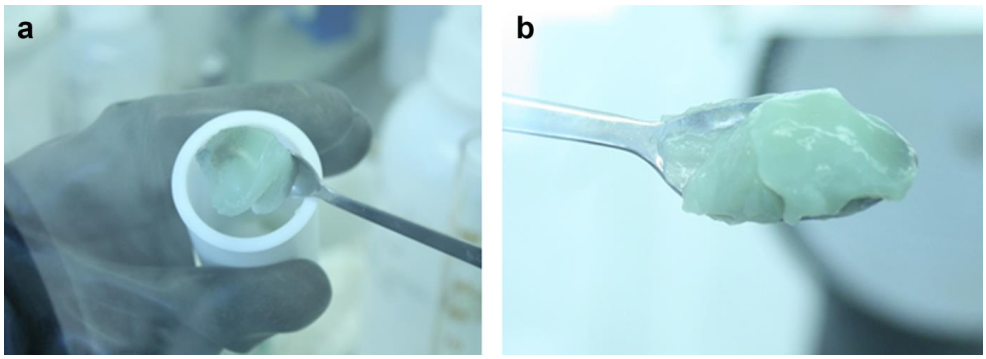

Figure 42: Precipitate of Pu-, Nd- and Zr-hydroxides within the synthesis route Pu-syn-1: (a) the fresh precipitate shows dark green spots corresponding to Pu-hydroxide; (b) whereas a homogenisation took place after several washing steps.

Within the synthesis routes Pu-syn-1 and Pu-syn-2 (chapter 4.1.7) where a prior precipitation of $Pu(OH)_4$ took place the precipitate was inhomogeneously coloured and dark green spots of the Pu-hydroxides were visible (Figure 42a). During the washing steps with deionised water a homogenisation of the precipitate is achieved leading to a uniformly greenish coloured precipitate (Figure 42b). The homogenisation might have not taken place at a molecular level. Therefore the precipitates may retain separated just as after precipitation as it was shown in Figure 41a. The presence of heterogeneous precipitates could promote the formation of PuO_2 from the Pu precipitate during the sintering process.

Therefore within Pu-syn-3 the simultaneous coprecipitation of all three hydroxides was forced according to Figure 41b. When the clear Pu solution with c(Pu) = 0.01 mol/L in 1 mol HNO_3 was added to the acidified metal salt mixture prior to the precipitation of the hydroxides, no premature precipitation occurred which indicates that no Pu polymer was formed. In contrast to Pu-syn-1 and Pu-syn-2 the undissolved impurity of the starting Pu composition was separated within the Pu-syn-3 approach. This separation within Pu-syn-3 will most probably lead to a single phase pyrochlore due to the absence of any impurities. In the following section the XRD results of the different compositions and the three different synthesis routes will be discussed.

Within the first synthesis route Pu-syn-1, a pellet with a Pu content of 5 mol% resulting in a $Nd_{1.9}Pu_{0.1}Zr_2O_7$ (Table 2) was synthesised. After 10 h of sintering at 1450 °C under argon atmosphere (Table 15) the upper side of the pellet was greyish whereas the bottom side was black. The grey colour might be caused by an oxygen deficit due to sintering in an argon glove box. The XRD pattern at the grey side of the pellet indicated the formation of a pyrochlore phase.

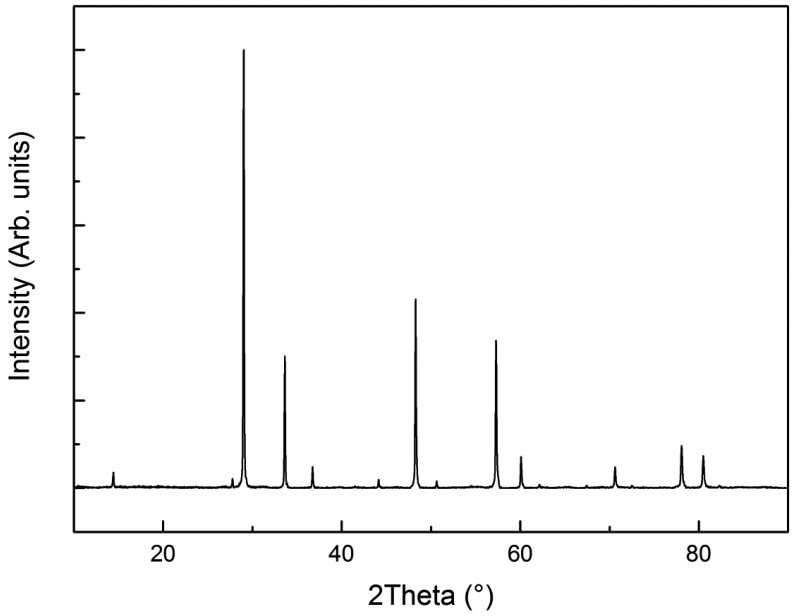

Figure 43: XRD pattern of $Nd_{1.9}Pu_{0.1}Zr_2O_7$ which was synthesised by Pu-syn-1 (details see chapter 4.1.7) after 25 h sintering at 1450 °C. The sample was powdered for the XRD measurement.

The pellet SF-71-P1 was ground and repressed to homogenise the powder. After an additional sintering step of 15 h at 1450 °C the repressed pellet had a bluish colour and the XRD pattern showed the pyrochlore crystal structure (Figure 43).

The calcination step in argon at 600 °C could have already led to the formation of cubic PuO_2. The corresponding reflexes of PuO_2 are adjacent to the pyrochlore reflexes, which makes it difficult to probe the presence of a minor PuO_2 phase by XRD.

Within the next synthesis route Pu-syn-2 the calcination was already carried out under reducing atmosphere to start the reduction process to Pu(III) and avoid a possible PuO_2 formation. Moreover, the Pu content was increased to 10 mol% resulting in a $Nd_{1.8}Pu_{0.2}Zr_2O_7$ (Table 2). Within the synthesis Pu-syn-2 the sintering duration was extended to 80 h, because the kinetics of the reduction to Pu(III) as well as the structural uptake are not known. The pellet SF-74-P2 had a homogeneous green colour at the upper side and the curved surface area after the sintering process and it was characterised by XRD. The XRD pattern showed the pyrochlore crystal structure. Due to the possible formation of PuO_2 which has an olive green colour, within the third approach Pu-syn-3 (chapter 4.1.7) the simultaneous coprecipitation of all hydroxides was forced. Two pellets were pressed and both sintered for 80 h to reduce the plutonium to Pu(III). The pellet was ground and the powder characterised

by XRD. The pattern showed the pyrochlore crystal structure. After repressing the powder into pellet shape and additional sintering this pellet was used for SEM characterisations.

Within an eightfold coordination and in the oxidation state +III the radius of plutonium r(Pu^{3+}) = 1.123 Å [117] is larger than the radius of neodymium r(Nd^{3+}) = 1.109 Å in an eightfold coordination. An uptake of plutonium at the A position of the pyrochlore should therefore lead to a shift of the XRD pattern to smaller 2Theta angles due to the lattice expansion. In Figure 44 a magnification of the (222) pyrochlore reflex is shown. A shift of this reflex with a Pu content of 5 mol% is observed compared to the pure $Nd_2Zr_2O_7$ (black).

However no difference in the position of the (222) reflex is observed for the two different synthesis routes of $Nd_{1.9}Pu_{0.1}Zr_2O_7$ Pu-syn-1 and Pu-syn-3. This could indicate that the synthesis route Pu-syn-1 was already successful without any PuO_2 formation. The pattern of the 10 mol% Pu composition $Nd_{1.8}Pu_{0.2}Zr_2O_7$ (green) show a further shift to smaller diffraction angles. Besides this main reflex a second reflex at a higher angle is present which is located at 2Theta = 28.65. On the one hand this could indicate the presence of crystalline PuO_2.

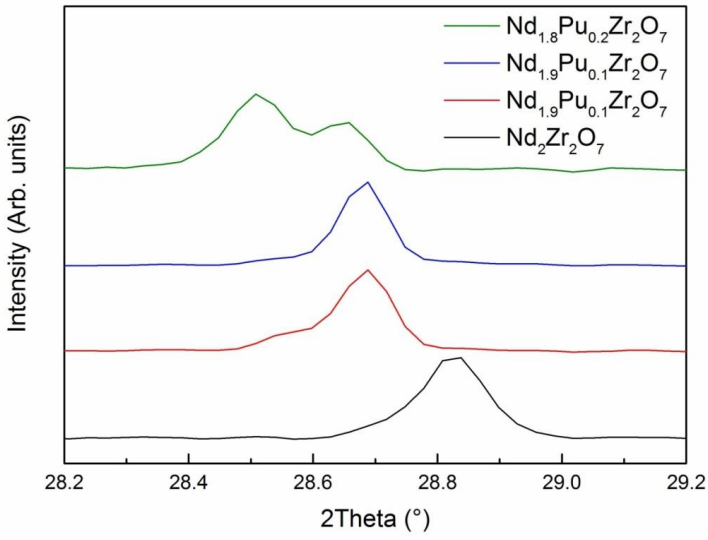

Figure 44: Magnification of the (222) pyrochlore reflex for a pure $Nd_2Zr_2O_7$ pyrochlore which was measured in pellet shape (black), $Nd_{1.9}Pu_{0.1}Zr_2O_7$ which was synthesised according to Pu-syn-1 and powdered for the XRD measurement (red), $Nd_{1.9}Pu_{0.1}Zr_2O_7$ which was synthesised according to the procedure Pu-syn-3 and also powdered for the XRD measurement (blue). The XRD pattern of $Nd_{1.8}Pu_{0.2}Zr_2O_7$ which was synthesised via Pu-syn-2 (green) was in pellet shape for the measurement.

On the other hand this could also indicate the presence of a second pyrochlore with a different Pu/Nd ratio. For the latter case two reflexes would be expected for all pyrochlore reflexes. However it is not this clear as it was the case for the (222) reflex and for most pyrochlore reflexes only a shoulder can be seen. It has to be considered that some XRD measurements were carried out at pellets, which could also be responsible for the observed shift of the reflexes. Nevertheless, the pattern indicate that the synthesis of Pu-pyrochlores has been carried out successfully.

The pellet SF-77-P1 of the most promising synthesis route was further characterised by SEM and EDX. The secondary electron (SE) image of the whole pellet was taken to get an overview about the pellet surface and the four spots which were investigated by EDX are labelled in Figure 45. The overview of pellet SF-71-P1 shows a homogeneous pellet. To gain deeper insight if Pu is distributed homogeneously an EDX mapping of the whole pellet was carried out (Figure 46). The element mappings in Figure 46b - d show a homogeneous distribution of Pu, Zr and Nd.

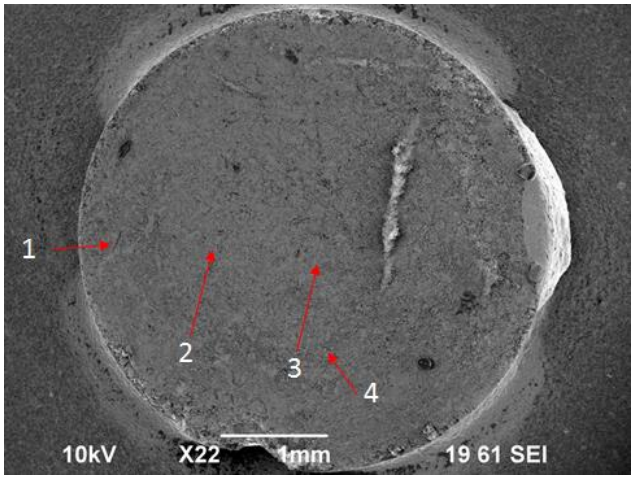

Figure 45: SE image of the coated pellet SF-77-P1 with the stoichiometry $Nd_{1.9}Pu_{0.1}Zr_2O_7$, where the places of interest are labelled.

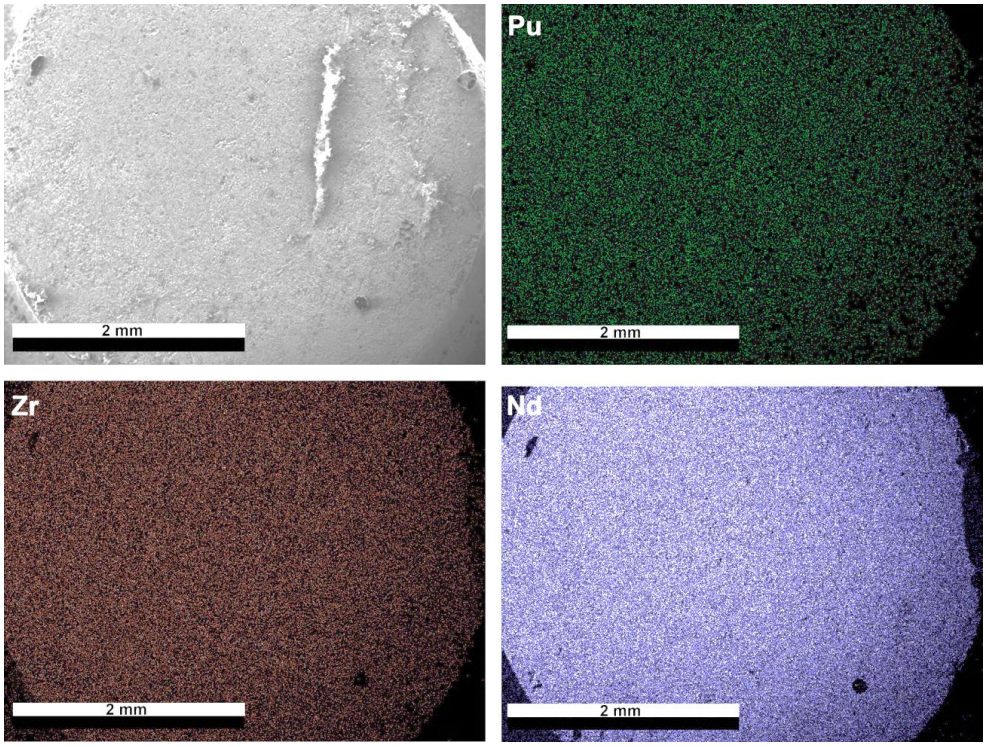

Figure 46: Overview of the pellet and EDX mapping for Pu (green), Zr (red) and Nd (blue) at the pellet surface. In total 20 frames were collected for the EDX mapping.

For further insight into the elemental distribution EDX spectra were recorded at four spots of interest. Figure 47 shows an EDX measurement of the Pu M-line of the the four different locations at the pellet. The measured mean value is about 5.50 weight% Pu, which is slightly higher than the calculated value of 4.03 weight% for the composition $Nd_{1.9}Pu_{0.1}Zr_2O_7$. In the EDX spectrum it can be seen, that Plutonium is distributed homogeneously for the locations 1 to 3, within the limit of error. Location 4 represents a particle with a diameter of about 40 µm in a cavity (Figure 48d). The amount of Plutonium at this location is measured to be 8.50 weight%. This value is one and a half times higher than for the locations 1 – 3.

Therefore the microstructure of the four locations was characterised in more detail. Figure 48a-c shows location 1 at three different magnifications. The sample is composed of grains between 1 – 5 µm (Figure 48c). The pellet is highly porous and the surface is covered with small grains. This may be caused by the grinding of the pellet and the relatively short sintering time of 5 h after the repressing. The differences in brightness between the smaller grains on top of the surface and the bigger “sintering bodies” can be explained as result of the difference of charging.

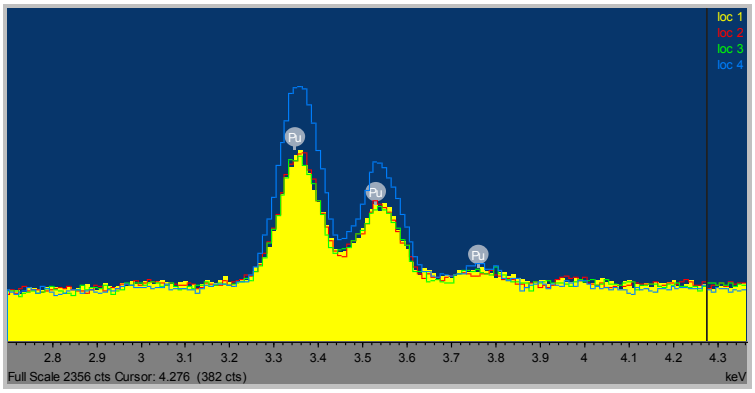

Figure 47: EDX measurement of the Pu M-line in a $Nd_{1.9}Pu_{0.1}Zr_2O_7$ pellet at four different locations of the pellet.

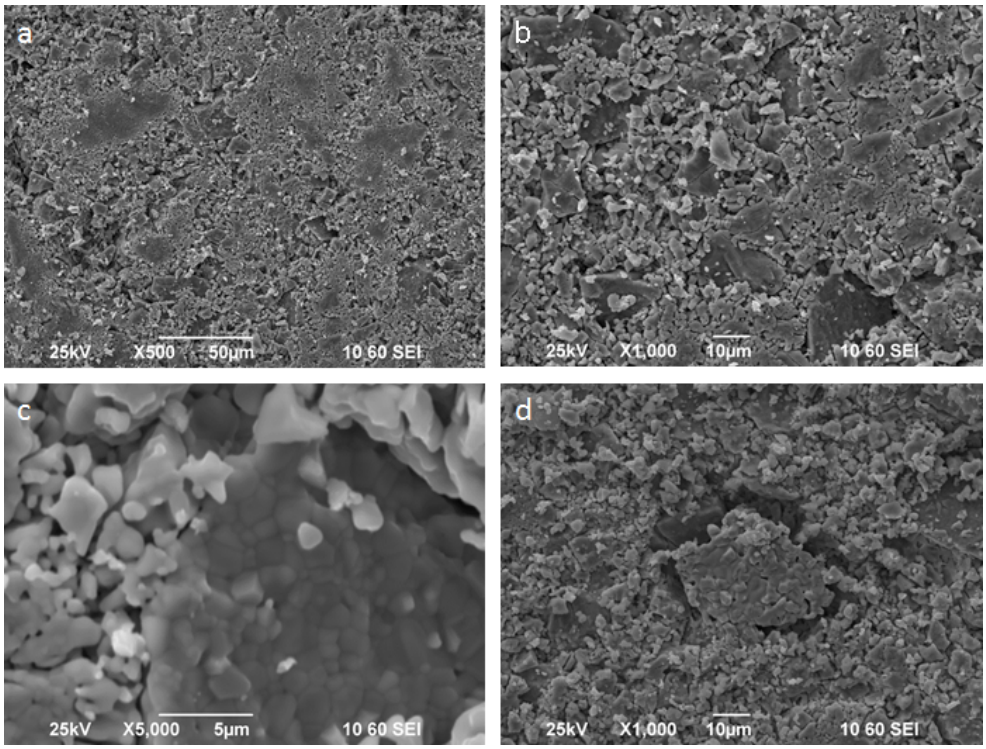

Figure 48: (a-c) SE images of location 1 with different magnifications; (d) shows a magnification of location 4.

No peculiarity was observed at the surface of the pellet, which would indicate the presence of a second phase in the pellet. The SE image of location 4 (Figure 48d) looks like the surrounding of the pellet and therefore, does not indicate the presence of a second phase.

All applied characterisation techniques indicate the formation of a Pu-pyrochlore whereas the oxidation state is not accessible with these methods. From the applied synthesis routes three different scenarios for the charge and position of Pu within the pyrochlore could result:

(1) According to Nästren [24] Pu(IV) is reduced to Pu(III) during the thermal treatment while/before the pyrochlore crystal structure is formed. This would lead to Pu(III) in an eightfold coordination at the A position within the pyrochlore.
(2) The kinetics of the pyrochlore crystallisation process may be faster than the reduction of Pu(IV) to Pu(III). Therefore, the pyrochlore structure would be built and Pu(IV) could occupy the A or B position. The reduction to Pu(III) could lead to an exchange of the Pu from the B to the A position but doesn't necessarily have to occur.
(3) The reducing conditions may not be adequate to reduce Pu(IV) to Pu(III) during the thermal treatment. In this case Pu(IV) would occupy the A or B position, but a mixed occupancy of both sides would also be possible.

To resolve these questions a proposal for EXAFS measurements was successfully submitted to the ANKA-INE beamline. With the help of XANES and EXAFS measurements it will be possible to figure out which of the three above mentioned ways the synthesis route worked and to test the presence of a minor PuO_2 phase.

5.3. Dissolution kinetics

A systematic study of the dissolution kinetics of ZrO_2 – Nd_2O_3 ceramics was carried out in the acidic pH range. The influence of classical parameters such as temperature and pH as well as the effect of the phase transformation of pyrochlore to defect fluorite were examined and might allow the derivation of a source term for a potential nuclear waste form in a deep geological repository. The results presented below were published in Finkeldei et al. (2014) [118] and Finkeldei et al. (2014) [119].

5.3.1 Batch Dissolution experiments

The dissolution kinetics of a stoichiometric pyrochlore were determined via a batch experiment (Figure 49a). The initial and final batch dissolution rates of the pyrochlore were determined according to equation (26) from the pre-leaching experiment as well as from the initial (day 1-14) and final stages (after day 14) of the batch dissolution experiment. The Nd-based pyrochlore dissolution rate decreased from the pre-leaching experiment ($4 \cdot 10^{-5}$ g m^{-2} d^{-1}) through the initial phase of the batch dissolution experiment ($3 \cdot 10^{-5}$ g m^{-2} d^{-1}) to a final batch dissolution rate of $2 \cdot 10^{-5}$ g m^{-2} d^{-1} (see Table 16).

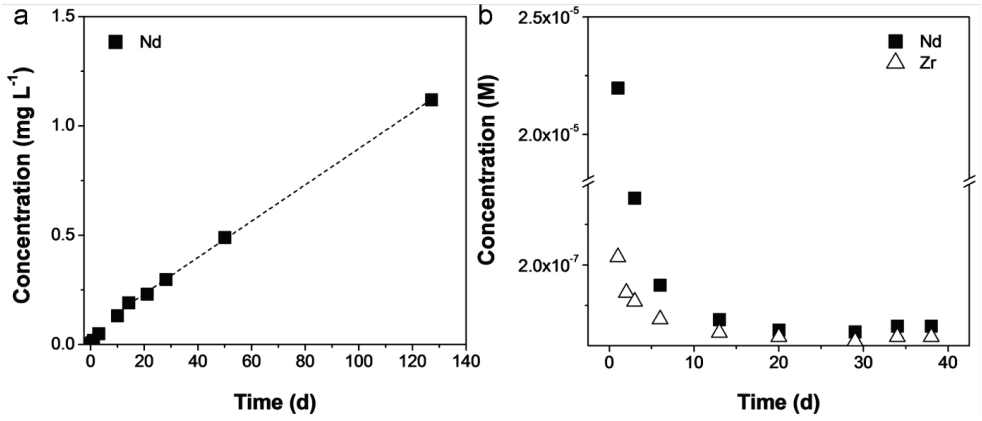

Figure 49: (a) Evolution of the Nd-concentration with time in a batch dissolution experiment with $Nd_2Zr_2O_7$ (pyrochlore). (b) Temporal evolution of the Nd- and Zr-concentrations in a stoichiometric pyrochlore during a dynamic dissolution experiment. Error is in both cases in the same range as the symbol size.

These rates are in good accordance with the dissolution rates of Kamizono et al. [120] for La-Zr pyrochlores. Due to the continuous decrease of the dissolution rate, a pre-leaching appears not to be necessary. However, the quality of the obtained data is higher due to the resetting of the Nd-concentration by exchanging the dissolution medium after the pre-leaching. Zr-based dissolution rates could not be measured from batch experiments due to limitations of available solution and adsorption of Zr on the ultrafilters.

To ensure that the measured dissolution rates are not solubility controlled the deviation from thermodynamic equilibrium were calculated with the GEM-Selektor package (section 5.3.6) [86-87, 121].

For more advanced studies of the dissolution kinetics including Zr-based dissolution rates the focus was laid on dynamic dissolution experiments. However, batch dissolution experiments are favourable to determine dissolution rates of actinide bearing pyrochlores. Due to the good accordance with the dissolution rates from dynamic dissolution experiments (Table 16), batch experiments were proven to determine reasonable rates for the dissolution of ZrO_2 – Nd_2O_3 pyrochlores.

5.3.2 Temporal evolution and stoichiometry of dynamic dissolution experiments

The temporal evolution of Nd- and Zr-concentrations of all realised dissolution experiments followed the typical trend of dynamic dissolution experiments with silicates and oxides as described in the literature [56, 73, 78]. At the beginning of the dissolution experiment high initial rates were observed, which decrease with time until a steady state was reached, which

is exemplarily shown for a non-stoichiometric 25mol% Nd_2O_3 pyrochlore (Figure 50). In the literature [56, 78, 84, 122-124] the high initial rates are explained by (1) high-energy surface sites and (2) the enhanced dissolution of fine particles. A change in the dissolution mechanism e.g. from the dissolution at grain boundaries to the dissolution on steps, kinks and etch pits on the grain surfaces (section 2.4.2) could also account for the enhanced initial rates [74].

How fast the steady state is reached was dependent on the particular experimental conditions. Here, the experiments at 110 °C and $c(H^+)$ = 0.1 mol/L achieved the steady state of the Zr release after 10 - 20 days. For an experiment at 70 °C it took approximately 10 days longer to reach the steady state. Several experiments showed an oscillating Nd-release after reaching the steady state (Table 17). This could suggest the presence of two different Nd-release mechanisms. Therefore, in Table 17 not an average rate but the two boundary values are depicted for these experiments.

Figure 50 shows a highly incongruent dissolution with a preferential Nd release, which is representative for all dissolution experiments within this study. The discrepancy of several orders of magnitude between the Nd and Zr release in the initial stage of the experiment becomes smaller over time i.e. a congruent dissolution is approached. The observed incongruent dissolution at the initial phase is typical for mixed oxides [56, 125-126]. For some minerals especially with layered structures e.g. the brucite-like octahedral layer of clay minerals versus the TOT (tetrahedral – octahedral – tetrahedral) layer, these different structural units are in charge of the incongruent dissolution [73].

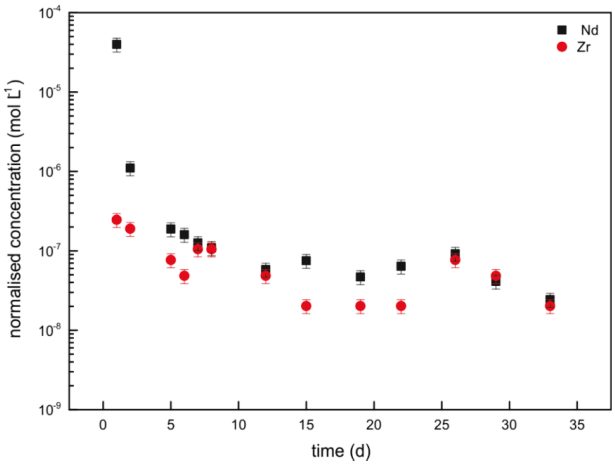

Figure 50: Temporal evolution of normalised Nd and Zr release concentrations from a pyrochlore (25 mol% Nd_2O_3) dissolution experiment at 90 °C in 0.1 n HCl. The Nd and Zr concentrations are normalised to the pyrochlore composition.

In the case of ZrO_2 - Nd_2O_3 pyrochlore and defect-fluorite, differences in the Zr-O and Nd-O bonding strengths may be partly responsible for the higher initial release rate of Nd. Within the pyrochlore the Nd is eightfold coordinated by six oxygen at the X- and two oxygen at the Y –position, whereas the A - Y distance is somewhat shorter than the A - X distance. The Zr cation is only sixfold coordinated by oxygen at the X-position (section 2.3.1). The higher coordination number of the neodymium causes a longer and therefore weaker Nd – O bond than the Zr – O bond. To strengthen this phenomenological explanation for a preferential Nd release the calculation of the activation energy for the detachment of Zr and Nd from the ideal pyrochlore surface is under preparation.

The change in the chemical composition that is accompanied by a structural change from pyrochlore to defect fluorite causes a disorder of the cations and anion vacancies. This results in a change of the bond lengths which become more similar for the different cations, because within the defect fluorite structure there is no longer a differentiation between two cationic positions. However the higher and favoured Nd release at the beginning of the dissolution experiments is valid for all dissolution experiments. Therefore, the bonding strength can only contribute to the observed behaviour. The degree of covalency of the Nd-O and Zr-O bonds, the cationic charge as well as the electronegativity may also be responsible for the observed preferential Nd release. Additionally aspects concerning the whole crystal structure of the minerals such as the location of the anion vacancies most likely play also an important role concerning the dissolution behaviour. Thermodynamic reasons could also be responsible for the incongruent release of Nd and Zr. These are discussed in section 5.3.6.

Since the powders used for the experiments are polycrystalline ceramics, surface inhomogeneities due to sintering cannot be excluded. Such inhomogeneities have been observed for other multioxides leading to an enrichment of one cation in a surface layer of a few nanometers which may then lead to incongruent dissolution [125]. Szenknect et al. [125] published a model consisting of three steps to explain the initial incongruent dissolution of Cerium (IV)-Neodymium(III) oxides which becomes congruent at a later steady state. They attributed the different dissolution phases to the evolving microstructure during the dissolution experiments.

5.3.3 Effect of chemical composition and non-stoichiometry of the dissolution rate

The influence of the chemical composition which involves a change in the crystal structure has been studied for seven different samples (Table 17). The samples with 12.9, 15.6 and 17.6 mol% Nd_2O_3 had a defect fluorite crystal structure whereas the 22.0, 25.0, 33.3 and 35.1 mol% Nd_2O_3 were pyrochlores. For all compositions a highly incongruent initial dissolution was observed. The initial Zr-based rates of the defect fluorite samples are very

similar within the limit of error (Figure 51a). For the pyrochlores an increase of the initial Zr-based rate correlates with an Nd-enrichment. In general the initial Zr-based rates (Figure 51a) are very similar to the Zr-based steady state rates (Figure 51 b) for all chemical compositions.

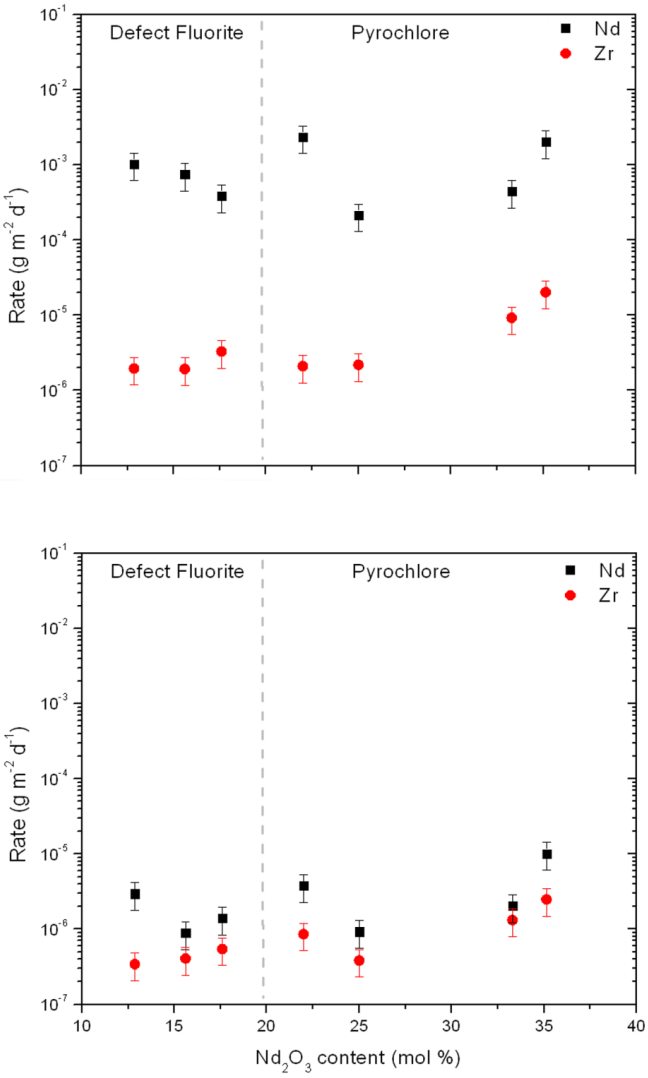

Figure 51: Nd (black) and Zr (red) based dissolution rates of pyrochlore and defect fluorite powders for seven different chemical compositions: (a) dissolution rates for the initial phase and (b) average steady state dissolution rates. All data are collected under the same experimental conditions: 90 °C and c(HCl) = 0.1 n.

In the ideal case of dissolution the dissolution rates of Nd and Zr would be equal. The incongruent dissolution could be explained in two ways:

(1) the dissolution rates of Nd and Zr are equal, but Zr is directly precipitated which leads to the lower Zr dissolution rate measured by ICP-MS,

(2) the dissolution of Zr is effectively lower than the dissolution of Nd.

Precipitation of a secondary phase - For the first case heterogeneous and homogeneous crystal growth of a secondary phase need to be considered. In case of a homogeneous crystal growth at some point the nucleation of ZrO_2 would start and baddeleyite formation would be observed in the solution. Thermodynamic calculations were carried out and are discussed in detail in section 5.3.6.

Heterogeneous crystal growth would lead to the formation of a baddeleyite layer at the ceramic surface. The lower Nd dissolution rate could be due to the secondary phase inhibiting or hindering the dissolution process.

Lower release of Zr compared to Nd - The second case could be explained by the two following scenarios. Zr might indeed be dissolved slower than Nd. This could possibly be due to a weaker oxygen – neodymium bonding strength as it was already mentioned in section 5.3.2. A preferential Nd dissolution would lead to a Zr enriched layer at the water mineral interface, because this is the area where the dissolution takes place. A formation of such a Zr enriched layer at the mineral surface could be probed by GI-XRD. The approximation of the Nd steady state rate to the Zr steady state dissolution rate could be caused by a limited accessibility of Nd which can only be overcome by Zr dissolution. However it might not be possible to differentiate which scenario originated such a secondary phase formation by GI-XRD.

The strong decrease of the Nd-release rate with time (Figure 51a and b), leads to a congruent or close to congruent dissolution. Therefore the Zr-release may dominate the steady state rate. However, Figure 51 does not show a systematic trend of the dissolution rate due to the phase transformation from the defect fluorite to the pyrochlore induced by changes of the Nd/Zr ratio. Only a slight increase of the steady state Nd-based rates approaching the pyrochlore phase boundaries was found. In general the dissolution rates of the pyrochlore samples are lightly higher compared to the defect fluorite samples.

The dependence of the Nd- and Zr-based dissolution rates on the chemical composition show a similar trend as the lattice distortions ε (Figure 30b) in the pyrochlore stability field. An increase of stress and strain seems to promote a higher dissolution rate.

Due to radiation damage Zr-based pyrochlores are known to undergo a phase transformation to the defect fluorite structure. The discussed results on the dissolution rates dependent on the change of the crystal structure showed that a radiation damage induced phase transition to the defect fluorite will most probably lead to dissolution rates which are within the same order of magnitude as the ones of the original pyrochlore.

5.3.4 pH dependence of the dissolution rate

As it was already described in section 2.4.2 the presence of hydroxyl groups or protons affects the dissolution kinetics. In this work the focus was set to study the $c(H^+)$ influence for a selected defect fluorite and pyrochlore sample. The defect fluorite sample had a Nd_2O_3 content of 15.6 mol% and for the pyrochlore the stoichiometric $Nd_2Zr_2O_7$ composition was chosen. Both samples were located in the middle of the corresponding stability field (Figure 28) to exclude any influence by coming close to the phase boundaries. In Figure 52 the dissolution rate is plotted versus $c(H^+)$. The proton concentration was experimentally verified by titration. Calculations with GEMS-PSI indicated a deviation from pH = 0, 1 and 2 by less than 0.1 logarithmic units for the given temperatures. The Nd- and Zr-based dissolution rates of the defect fluorite (Figure 52a) and pyrochlore (Figure 52b) followed a linear trend for the $c(H^+)$ dependence. Regardless of the crystal structure the dissolution rate increased with increasing proton concentration. The slope of the pH dependent release as a function of log(Rate) was -0.56 and -0.51 for the Nd- and Zr-based rates of the defect fluorite. Within the pyrochlore sample a slightly stronger pH dependence for the Zr-based rate was found than for the Nd-based dissolution rate, with slopes of -0.67 and -0.43 respectively. The range of n = 0.43 - 0.67 for the Nd- and Zr-based dissolution rates of both samples is similar to many natural minerals such as silicates where cation exchange and breaking of metal-oxygen bonding was identified as the rate controlling step in the pH-regions below the point of zero charge [58, 64]. Therefore a similar mechanism might control the dissolution of ZrO_2 - Nd_2O_3 ceramics. The very similar slopes for the Nd- and Zr-based rates may also indicate a similar process for the release of both cations. As described in section 2.4.2 a minimum of the dissolution rate commonly occurs around the point of zero charge which for many oxides was observed in the near neutral pH range. Therefore, an extrapolation from the presented data to the near neutral pH region which is of interest for a deep geological repository should be possible.

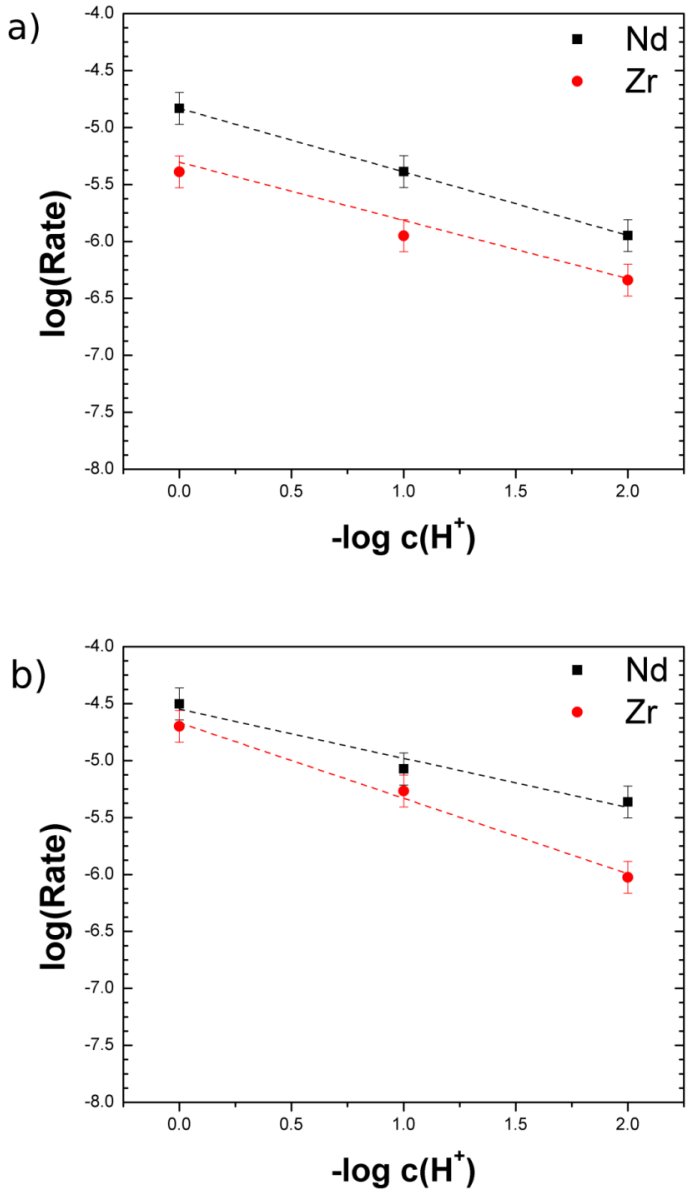

Figure 52: (a) Relationship of log(Rate) and the proton concentration for a defect fluorite (15.6 mol% Nd_2O_3); with a slope for the Nd-based rate of -0.56; and -0.51 for the Zr-based rate and (b) a stoichiometric pyrochlore with a slope for the Nd-based rate of -0.43; and -0.67 for the Zr-based rate.

5.3.5 Effect of temperature

To study the effect of temperature the samples with the same chemical compositions and crystal structure were chosen as for the pH dependence to allow a comparison of these two parameters. The dissolution studies were conducted at 70 °C, 90 °C and 110 °C. In chapter 5.3.2 the Zr-release was shown to control the steady state dissolution rates. Therefore, only the Zr-based dissolution rates are depicted in Figure 53. The dissolution rates obtained for the pyrochlore are higher than for the defect fluorite (Figure 53) as it was already found in chapter 5.3.3.

Assuming a linear dependence of the dissolution rate on the temperature the activation energies can be derived according to the classical Arrhenius approach (section 2.4.2). The activation energy of the pyrochlore sample Ea(Zr-based pyrochlore) = 47 kJ/mol indicates a surface controlled dissolution mechanism. The activation energy determined for the defect fluorite is lower Ea = 28 kJ/mol but still indicating a surface controlled dissolution mechanism. These values are comparable with published activation energies. Claparede et al. [20] derived activation energies for fluorite type oxides e.g. ThO_2, CeO_2 and PuO_2 to be in the range between 20 and 37 kJ/mol. Kamizono et al. [120] reported dissolution rates of La-Zr-based pyrochlores obtained in deionised water and at different temperatures. From their data an activation energy of about 40 kJ/mol can be estimated.

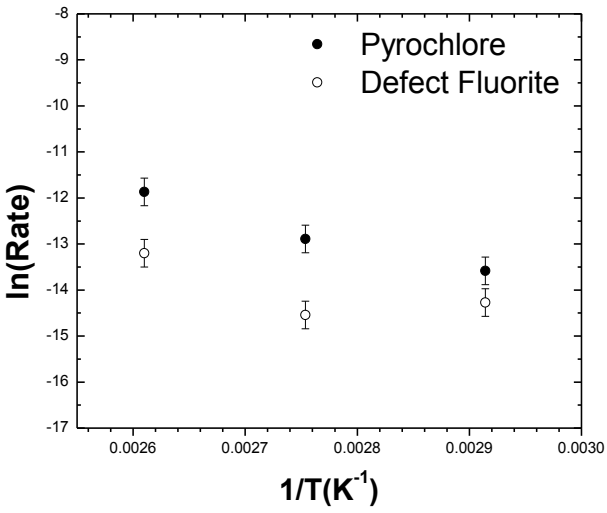

Figure 53: Arrhenius plot of the temperature dependence of Zr-based dissolution rates for a defect fluorite (15.6 mol% Nd_2O_3, open symbols) and pyrochlore (33.3 mol% Nd_2O_3, solid symbols) powdered ceramic.

The Arrhenius approach assumes a single dissolution mechanism which stays the same all through the temperature range of interest. Here, a linear description of the dissolution rate on the temperature may not be completely sufficient especially for the defect fluorite sample. The idea of a complex system of several potentially interacting dissolution mechanisms for the ZrO_2 – Nd_2O_3 ceramics will be discussed in chapter 5.3.7.

5.3.6 Deviation from thermodynamic equilibrium

Two approaches were followed to calculate the deviation from thermodynamic equilibrium at the experimental conditions of 90 °C and pH ~ 1 (Table 7 and Table 8). The first recipe in Table 7 assumes the complete dissolution of $Nd_2Zr_2O_7$. The calculations should figure out if saturation effects may occur which may influence the pyrochlore dissolution rate.

Table 7: System definition used for GEM-Selektor calculation of the complete dissolution of $Nd_2Zr_2O_7$ pyrochlore.

Parameter	Value
H_2O	1000 g
$Nd_2Zr_2O_7$	0.1 g
HCl	0.1 moles
Temperature	90 ^oC
Pressure	1 bar

The second approach dealt with the possible formation of secondary phases and the corresponding over- or undersaturation in the aqueous phase at typical steady state conditions. Therefore Table 8 contains the experimentally determined Nd and Zr concentrations from the dynamic dissolution experiments.

Table 8: System definition for GEM-Selektor interpretation of results of dynamic dissolution experiments with $Nd_2Zr_2O_7$ pyrochlore from dynamic dissolution experiments.

Parameter	Value
H_2O	1000 g
Nd	5.80×10^{-8} moles
Zr	3.80×10^{-8} moles
HCl	0.1 moles
Temperature	90 ^oC
Pressure	1 bar

Assuming the total dissolution of 0.1 g of $Nd_2Zr_2O_7$ in acidic solution at 90 °C led to the theoretical values of 3.43×10^{-4} and 7.04×10^{-11} mol · kg^{-1} molalities of Nd and Zr, respectively (Table 9). These calculations suggest an incongruent dissolution of a stoichiometric pyrochlore which would be accompanied by the formation and precipitation of a secondary phase. From a thermodynamic point of view ZrO_2 in baddeleyite modification would be the stable phase at the predominant conditions. The value 7.04×10^{-11} mol · kg^{-1} (Table 9) corresponds to the aqueous solubility of ZrO_2 at T = 90 °C and pH = 1.128. The value 3.43×10^{-4} mol · kg^{-1} corresponds to the total amount of Nd in 0.1 g of $Nd_2Zr_2O_7$ assuming a complete dissolution.

Table 9: Thermodynamic modelling results of $Nd_2Zr_2O_7$ pyrochlore dissolution in a batch from which no reactants* are removed.

mNd$_{aq}$ (mol · kg^{-1})	mZr$_{aq}$ (mol · kg^{-1})	pH	Solids (mol) ZrO_2(cr)
3.43×10^{-4}	7.04×10^{-11}	1.128	3.43×10^{-4}

*reactants are: Nd_2O_3(cr), $Nd(OH)_3$(cr), $Zr(OH)_4$(am), ZrO_2(cr).

These calculations indicate a complete transformation of $Nd_2Zr_2O_7$ to baddeleyite, but this is only valid for a closed system in which none of the reactants are exchanged. Within the dynamic experiments the aqueous solution is constantly removed which could explain why no baddeleyite formation was observed in the SEM analysis of the samples.

The aim of the second recipe was a prediction of the aqueous composition at the conditions of the dynamic dissolution experiments and the outflow concentrations of Nd and Zr were used (Nd = $5.80 \cdot 10^{-8}$ and Zr = $3.80 \cdot 10^{-8}$ mol · kg^{-1}; Table 8). The thermodynamic calculations resulted in Nd and Zr concentrations in the aqueous phase of 5.18×10^{-8} and 7.17×10^{-11} mol · kg^{-1}, respectively (Table 10) at a pH = 1.12. Due to a higher Zr concentration in the outflow solution a supersaturation of ZrO_2 seems to be probable which would cause a baddeleyite precipitation.

Table 10: Results of thermodynamic modelling based on averaged typical Nd and Zr aqueous concentrations in outlet solutions of experiments at 90 °C and pH ~1.

mNd$_{aq}$ [mol · kg^{-1}]	mZr$_{aq}$ [mol · kg^{-1}]	pH	Solids [mol] ZrO_2(cr)
5.80×10^{-8}	7.17×10^{-11}	1.123	2.19×10^{-8}

With the help of the saturation index (*SI*) the deviation of the solid-liquid system from the thermodynamic equilibrium can be expressed numerically:

$$SI = \log(IAP / K_{SP}) \tag{40}$$

The ion activity product (*IAP*) corresponds to the calculated ion activity product in solution and K_{SP} to the solubility product [127]. The previous calculations predicted a possible precipitation of ZrO_2. Therefore the saturation index for ZrO_2 was estimated and the dissolution of this secondary phase could be expressed via:

$$ZrO_{2(cr)} + 2H_2O_{(l)} = Zr^{4+} + 4\,OH^- \tag{41}$$

The ZrO_2 solubility product $K_{SP}(ZrO_2)$ is written as product of the aqueous activities of Zr^{4+} and OH^- species at equilibrium:

$$K_{SP}(ZrO_2) = \left\{Zr^{4+}\right\} \cdot \left\{OH^-\right\}^4 \tag{42}$$

For the calculation of the *IAP* of the solution the baddeleyite formation is suppressed and the aqueous species and activities of the zirconium- and hydroxide-ion are rather determined from the measured composition in the aqueous phase. Table 11 shows the computed aqueous activities for the case that baddeleyite formation is suppressed as well as the case where baddeleyite is in equilibrium with the aqueous solution. These aqueous activities where calculated from $K_{SP}(ZrO_2)$, $IAP(ZrO_2)$ and *SI* of ZrO_2(cr) in the dynamic dissolution experiment.

Table 11: Estimated values of activities for Zr^{4+} and OH^- aqueous species, solubility product ($K_{SP}(ZrO_2)$), ionic activity product ($IAP(ZrO_2)$) of ZrO_2(cr) and saturation index (SI) of ZrO_2(cr) at conditions of the dynamic dissolution experiment (T = 90 °C and P = 1 bar).

ZrO_2(cr) is not precipitating			ZrO_2(cr) in equilibrium with aqueous solution			SI
$\{Zr^{4+}\}$	$\{OH^-\}$	$IAP(ZrO_2)$	$\{Zr^{4+}\}$	$\{OH^-\}$	$K_{SP}(ZrO_2)$	
$4.61 \cdot 10^{-12}$	$4.97 \cdot 10^{-12}$	$2.81 \cdot 10^{-57}$	$1.04 \cdot 10^{-14}$	$4.97 \cdot 10^{-12}$	$6.35 \cdot 10^{-60}$	2.65

Table 11 shows a supersaturation index for ZrO_2 of 2.65 which indicates a significant oversaturation. ZrO_2 can either crystallise in a monoclinic or cubic modification. The solubility of both modifications at room temperature was studied in dissolution experiments with a duration of 250 days at room temperature and pH = 9 by Pouchon [128-129]. Short time experiments in the acidic pH regime were done by Kovalenko and Bagdasarov [130]. Sheka and Pevzner [131] performed dissolution experiments for 45 days in the alkaline regime (pH = 13 - 14). Bilinski et al. [132] studied the opposite approach by performing precipitation experiments from strongly oversaturated solutions in the acidic regime (pH = 1.5 – 6.5).

Curti and Degueldre [133] derived a pH dependent solubility curve for ZrO_2(cr) – H_2O with the dissociation constants selected by Baes and Mesmer [134]. This curve could fit all the experimentally obtained dissolution results. However the solubility curve could not satisfactory fit the measured Zr concentrations of Bilinskis precipitation experiments. Curti and Degueldre accounted the presence of ZrO_2 polymers therefore which precipitate in a condensation reaction of the dissolved polymers. This depolymerisation step into a crystalline anhydrous oxide is a very slow process and the equilibrium between ZrO_2 and aqueous media is hardly achievable. In the case of dissolution studies with $Nd_2Zr_2O_7$ the similar effect of slow depolymerisation cannot be neglected, i.e. ZrO_2 may not precipitate within the time scale of the experiments due to kinetic reasons.

However, experimental observations indicated that the aqueous solutions taken during the experiments are stable for several months. No relevant concentration differences could be detected for solutions measured immediately after sampling and several weeks later. The formation of a secondary phase at the mineral surface could also not be detected by SEM. However, such a secondary phase formation at the mineral surface may be very thin and not homogeneously distributed at the surface and therefore probably not detectable by SEM. GI-XRD is a highly sensitive technique to changes at the surface of a monolith and will be used in future studies to monitor the presence of potential secondary phases.

5.3.7 From the macroscopic to the microscopic scale

The microstructure can play a key role concerning the dissolution kinetics [74, 125, 135]. To gain insight how the dissolution proceeds a complementary microscopic study was carried out. As a first attempt all ceramic powders were characterised prior and after the dissolution experiments by SEM in the low vacuum mode at 0.6 mbar. In the following section the SEM results of one defect fluorite and one pyrochlore sample will be exemplarily examined in detail. Additionally the porosity effect on the microstructural changes is studied by comparison of two stoichiometric pyrochlores.

Figure 54a and b show a defect fluorite sample with 12.9 mol% Nd_2O_3 prior to the dissolution experiment. The microstructure is characterised by its well-developed microstructure with straight, well-defined grain boundaries which are typical for all defect fluorite samples in this work. The intragranular porosity is relatively low. Typically the defect fluorite ceramics show a primary grain size between 5 - 10 µm. The starting material exhibited a preferential formation of intergranular pores. A comparison of Figure 54a and c, whereas the latter image corresponds to the powder after the dissolution, show that the structure of the 100 – 180 µm particles remained the same. The magnification of the specimen after dissolution in Figure 57d indicates a preferential dissolution at the triple junctions and grain boundaries. Defect densities are known to accumulate at the grain boundaries, which will most probably be the same for the characterised ceramics. This promotes the preferential dissolution at the grain boundaries in comparison to the bulk material. A preferential Nd-release due to a Nd-enrichment at the grain boundaries which are favourable dissolution sites, could be excluded by TEM and EDX measurements (section 5.1.3).

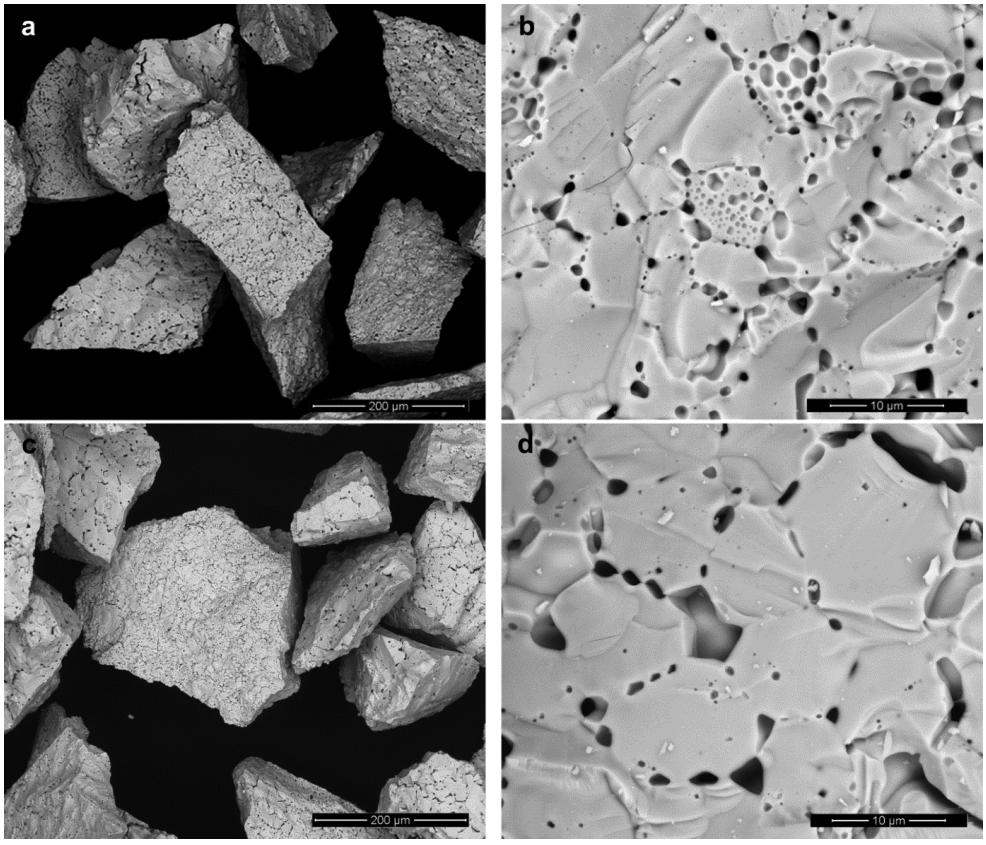

Figure 54: SEM images of the 100-180 µm size fraction of a 12.9 mol% Nd_2O_3 defect fluorite powder. Pictures (a) and (b) are taken previous to the dissolution experiment at (a) a lower and (b) higher magnification. (c) shows the powder after the dissolution experiment while picture (d) is taken again at a higher magnification. All images are taken in the low vacuum mode.

Lüttge et al. [74] have discussed the difference between the specific surface area and the reactive surface sites due to the different activation energies of e.g. kink sites, grain boundaries and edges.

Looking at the pyrochlore samples, a change in the microstructure becomes visible. Compared to the defect fluorite sample the primary grains of the pyrochlore samples are much smaller. Therefore, using the same amount of a defect fluorite sample and a pyrochlore might also lead to a higher dissolution rate of the pyrochlore samples, because there is a higher concentration of grain boundaries which are the reactive sites for dissolution. This could explain the higher dissolution rates in the stability field of the pyrochlore compared to the defect fluorite samples in section 5.3.3 (Figure 51).

First the pyrochlore that was synthesised via the same procedure as the defect fluorite will be discussed before a second pyrochlore sample is analysed microscopically which was synthesised via precipitation with gaseous ammonia according to section 4.1.2.

Figure 55a and b show a higher porosity of the pyrochlore powder than it was obtained for the defect fluorite (Figure 54a, b). The 100 – 180 µm particles consist of dense agglomerates of primary grains which are 1 -2 µm in size. The microstructure dramatically changed due to the dissolution for 82 days in 0.1 M HCl at 90 °C. As dissolution proceeded small amounts of the ceramic disintegrated which led to the presence of a fraction with a grain size of 1 - 2 µm (Figure 55c, d). For the defect fluorite samples a preferential dissolution at the grain boundaries was already observed. The dissolution mechanism acting on the pyrochlore grain boundaries harmed the pyrochlore grain boundaries more heavily which most probably led to disintegration of the microstructure.

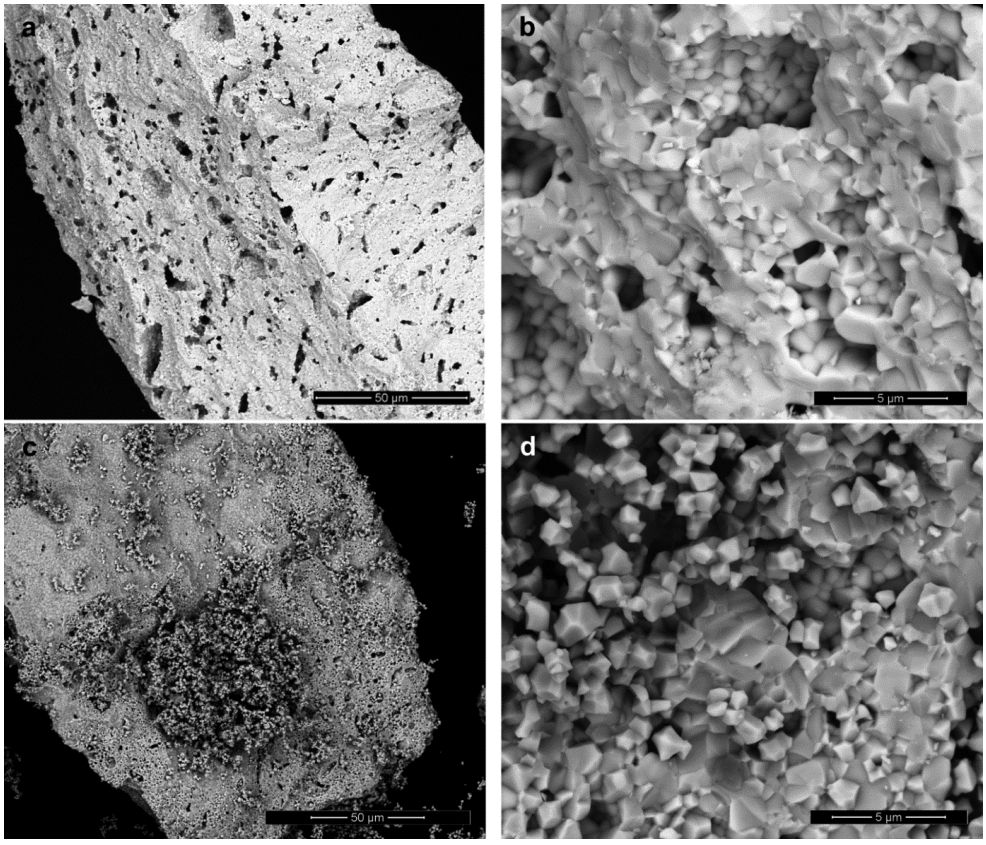

Figure 55: SEM images of the 100-180 µm fraction of the $Nd_2Zr_2O_7$ powder (PY-1) (a, b) previous to the dissolution experiment at (a) a lower and (b) higher magnification and (c, d) after the dissolution experiment at (c) a lower and (d) a higher magnification.

The weak nature of grain boundaries is in the recent literature often assigned to chemical inhomogeneities at the grain boundaries and the formation of leached layers. Chemical inhomogeneities may be introduced during the sintering procedure and could result e.g. in a Nd enrichment at pores and grain boundaries [136-138]. Especially in the initial stage of the experiment a preferential Nd-release was found. An Nd enrichment at the grain boundaries which are the favoured dissolution sites would give an explanation for these findings. Whereas the formation of leached layers could be generated due to a weaker binding energy between Nd-O compared to Zr-O. A model for this kind of incongruent dissolution has been proposed by Szenknect et al. (2012) [125].

The thermodynamic calculations in section 5.3.6 suggested a supersaturation of ZrO_2 during the experiment. However no precipitation of a separate ZrO_2 phases was found during the experiment. The incongruent Zr and Nd release may also be due to a partial transformation of pyrochlore to ZrO_2 or $Zr(OH)_4$ at the surface.

In all above described scenarios a weakening of the grain boundaries will occur at some point, leading to the disintegration. As it is shown in Figure 55d the disintegration comes along with the supply of fresh surfaces which may then dominate the dissolution kinetics. The preferential dissolution at grain boundaries and pores will repeat itself at the newly accessible sites, resulting in a preferential Nd release. This could also explain the oscillations in the Nd release in some experiments at a time where the Zr release had already reached the steady state (Table 17). All above mentioned mechanisms can lead to the incongruent dissolution of the ZrO_2 - Nd_2O_3 ceramics which makes it impossible to identify the dissolution mechanism on the base of these SEM images. Due to the high porosity of the ceramic powder prior to the dissolution experiment the specific surface area was already dominated by the surface area of the primary grains. Therefore, no significant increase of the specific surface area was expected as a consequence of the disintegration. Additionally the single grains should show a lower dissolution rate because they do not offer grain boundaries any longer which are the main sites for the dissolution process to take place. Finally no strong impact on the dissolution rate is expected by this not very reactive fine fraction.

To study the effect of porosity on the dissolution the porous pyrochlore sample (Figure 55) was compared with a second sample of the same chemical but different microstructural character. Figure 56a and b show pyrochlore grains of much less porosity while the primary grains are about the same size as it was the case for the pyrochlore of higher porosity (Figure 56c and Figure 55c). In contrast to PY-1, the texture of the denser pyrochlore PY-2 is composed of a homogeneous network of the primary grains. For this sample the dissolution experiment did not lead to a disintegration but the grains are rather intact (Figure 56c, d).

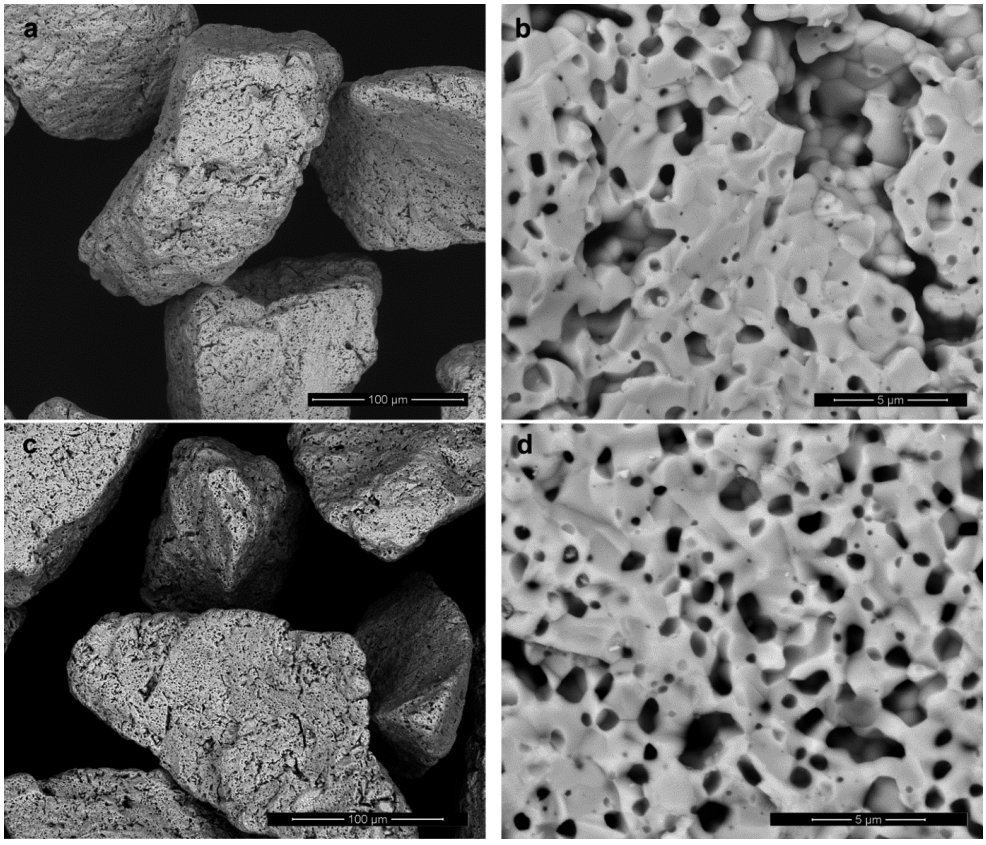

Figure 56: SEM images of the 100-180 µm fraction of a $Nd_2Zr_2O_7$ powder (PY-2) (a, b) previous to the dissolution experiment at (a) a lower and (b) a higher magnification. Images (c) and (d) depict the powder after the dissolution experiment. This sample has been prepared by a different synthesis route (section 4.1.2) compared to the samples in Figure 55.

Table 12 summarises the normalised Nd and Zr dissolution rates of the two stoichiometric pyrochlores which differ in their degrees of porosity. The dissolution rates for the pyrochlore with a higher porosity are by a factor of 2 – 3 higher compared to the less porous pyrochlore. The less stable microstructure possesses more directly accessible grain boundaries for the dissolution. This led to a higher density of reactive surface sites at the total surface area.

Table 12: Normalised Nd- and Zr-based dissolution rates of two stoichiometric pyrochlores with a different degree of porosity. PY-1 was synthesised with liquid ammonia and PY-2 with gaseous ammonia as precipitating agent.

Pyrochlore sample	Rate (Nd) $[g \cdot m^{-2} \cdot d^{-1}]$	Rate (Zr) $[g \cdot m^{-2} \cdot d^{-1}]$
PY-1	$4 \cdot 10^{-6}$	$3 \cdot 10^{-6}$
PY-2	$2 \cdot 10^{-6}$	$1 \cdot 10^{-6}$

Microscopic dissolution study on a pyrochlore monolith - To study the progression of the dissolution at the ceramic surface in more detail a long-term dissolution experiment at a $Nd_2Zr_2O_7$ monolith was performed. These measurements were carried out at the ICSM in Marcoule. The polished surface of the pellet was characterised by SEM prior to the dissolution experiment, after 20, 39, 62, 84, 253, 613, 991 and 1092 hours.

Figure 57 shows the pellet after 20 h (a, b) and 39 h (c, d) of dissolution with the same detail in the magnifications. The scratches at the pellet surface are due to the polishing step prior to dissolution. The SEM images clearly indicate highly heterogeneous dissolution behaviour. Especially in Figure 57c it becomes visible, that several regions of the surface participate heavily in the dissolution process whereas others retain unchanged. Moreover, the dissolution seems to start preferentially and fast at triple points. Once they are opened they do not evolute further and the dissolution stops at these sites. This is clearly indicated by the magnifications in Figure 57b and d. Within Figure 57b steps have been developed due to the dissolution process. However, these steps are not the starting point for the dissolution to proceed as it could be expected. In contrast, the dissolution proceeds by opening of new triple points.

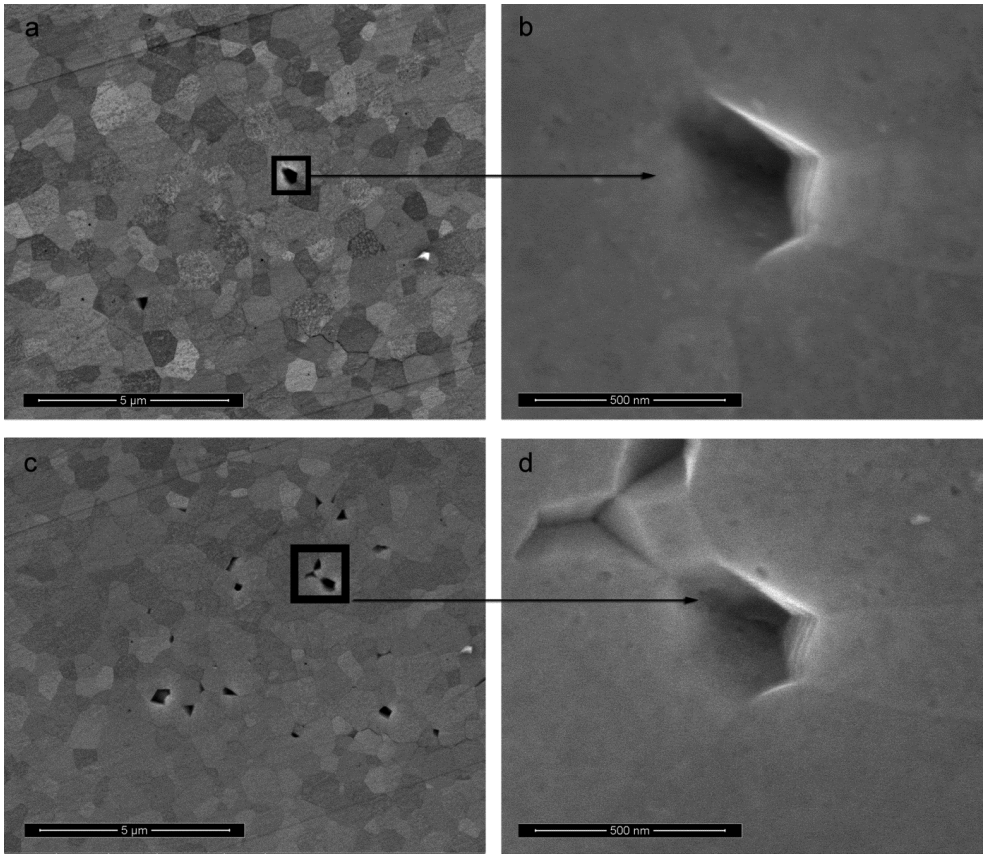

Figure 57: SEM images at the surface of a pyrochlore monolith after (a) 20 h of dissolution and (c) 39 hours of dissolution in 4 M HCl at 90 °C. Images (b) and (d) show magnifications of the same spot at the monolithic surface after 20 h and 39 h of dissolution, respectively.

With the progression of the dissolution process the grain boundaries are more and more attacked which leads to a rounding of the grain boundaries themselves as particularly visible in Figure 58c. Figure 58b shows the same spot of the sample as in Figure 57b and d and it becomes visible that the dissolution stops at a certain point. It is unclear whether the encircled area in Figure 58b was caused by the dissolution at a triple junction or is the result of the disintegration of a grain. Figure 58a and c show that individual grains are pulled out of the surface when the dissolution process proceeds. Due to the dissolution at the grain boundaries of grain "1" from Figure 58b the grain loses its contact to the surrounding grains at a certain time. Therefore grain "1" can be pulled out of the surface, which is indicated by the arrow and Figure 58c shows the presence of additional porosity at the layer below grain "1". At a later stage of the experiment this process will lead to the disintegration as shown for the $Nd_2Zr_2O_7$ pyrochlore in Figure 55c and d.

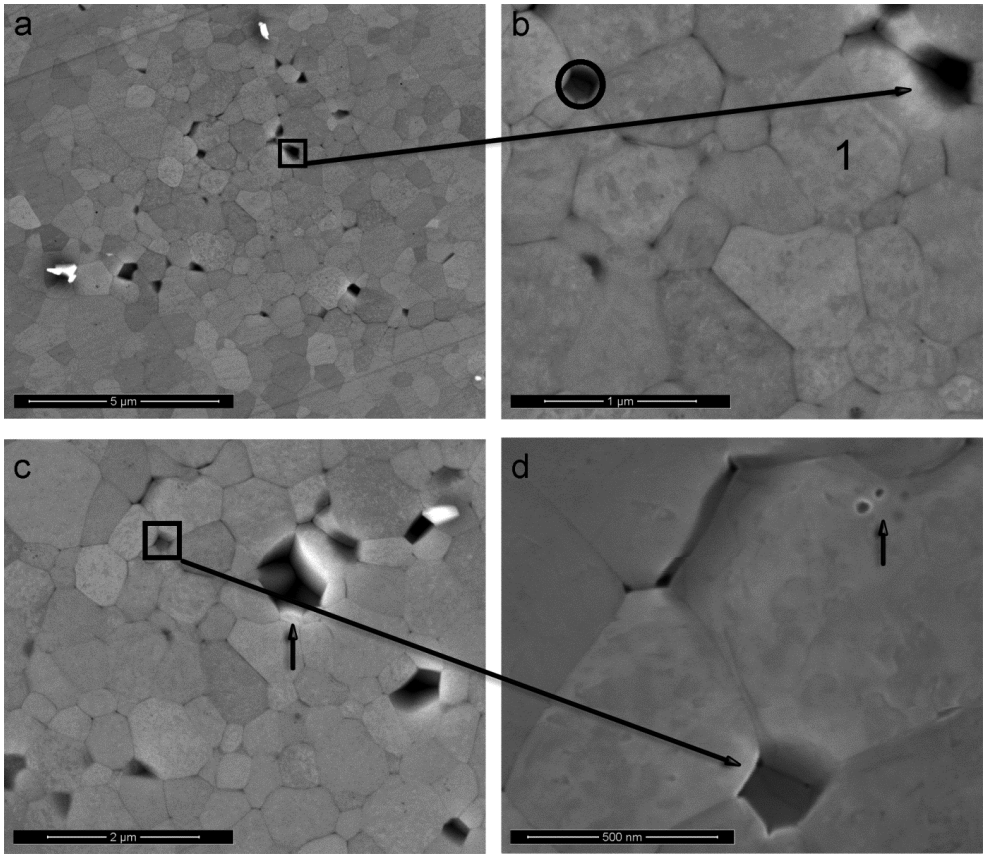

Figure 58: SEM images at the surface of a pyrochlore monolith (a, b) after 253 h of dissolution and (c, d) 613 hours of dissolution in 4 M HCl at 90 °C.

Additionally the evolution of etch pits (Figure 58d, arrow) becomes clearly visible after 613 h of dissolution. Image d also shows the highly incongruent surface of the single grains where it stays unclear from the SEM images if this is due to chemical inhomogeneities or rather surface roughness as a consequence of the propagating dissolution mechanism. Figure 59 depicts SEM images after 1092 h of dissolution in two different magnifications. From image a the heterogeneity of the surface to dissolution becomes visible.

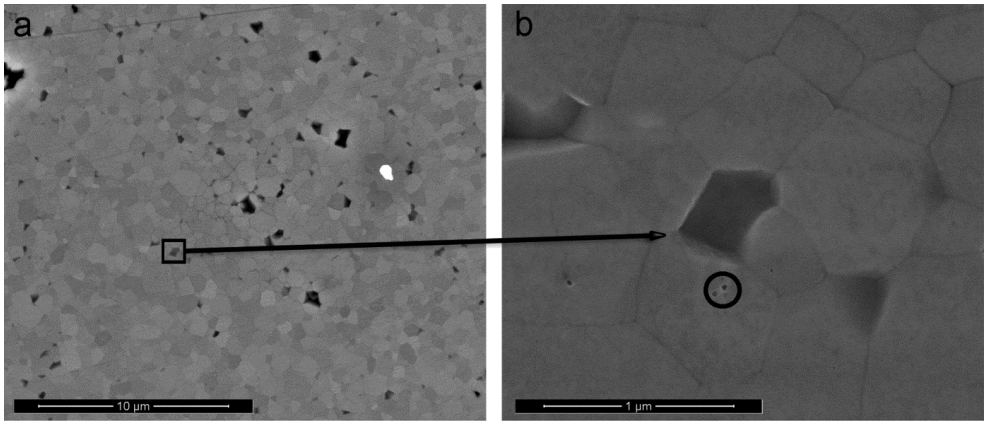

Figure 59: SEM images at the surface of a pyrochlore monolith after 1092 h of dissolution in 4 M HCl at 90 °C.

The magnification (b) proves the presence of different kinds of dissolution processes which are opening of the triple junctions, dissolution at the grain boundaries, pulling out of single grains whereas etch pits are also present (Figure 59b, encircled). The sequence of the SEM images from Figure 57 to Figure 59 show the temporal evolution of the surface due to the dissolution processes and identified different sites of the dissolution. The dissolution of ZrO_2 – Nd_2O_3 ceramics occurs by a complex interaction of different dissolution mechanisms at various sites. Each process might have its own activation energy. Therefore, the Arrhenius approach (section 5.3.5) may not be appropriate for the prediction of the dissolution rate as a function of temperature in this type of system.

Vertical scanning interferometry - The VSI measurements were carried out in cooperation with the University of Bremen. The strength of a vertical scanning interferometer is the huge variability of the field of view which enables the user to decide whether the observations made at a high magnification are representative for the sample or not. Prior to the dissolution half of the pellet surface was coated with a thin gold layer (Figure 60). The coating helps to orientate at the pellet surface and remeasure the same area after different dissolution time intervals. Moreover, the gold coating provides a reference surface to monitor the overall surface retreat of the pellet.

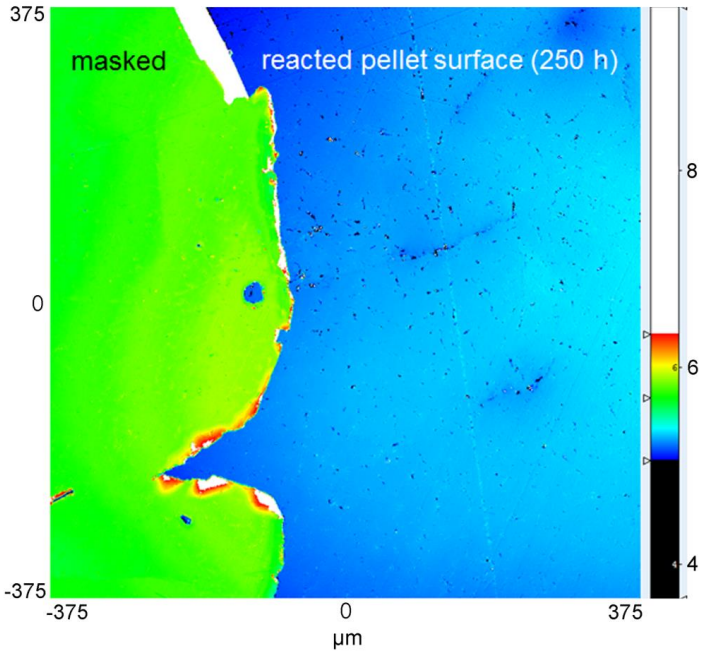

Figure 60: Pellet surface of a $Nd_2Zr_2O_7$ ceramic (blue) which is coated partly with a gold layer (green) after 250 h of dissolution. Due to technical reasons the gold mask has partly detached from the pellet surface.

Figure 61 shows a $Nd_2Zr_2O_7$ pellet after 40 h (a) and after 336 h (b) of dissolution at a low magnification. The surface of the monolith is dominated by scratches from the polishing procedure. The green features in Figure 61b indicate that the monolith surface is not perfectly flat. Therefore the middle part of the pellet was analysed where the influence of the bending has a less strong impact than approaching the edges of the pellet. The VSI images show an inhomogeneous surface of the monolith which was already seen by the SEM images (Figure 58). The white areas correspond to vertical exaggerations of the z-direction on the surface of the monolith. These are most probably caused by the gold coating which was detached from the monolith surface with progressing dissolution due to technical reasons and deposited randomly at the pellet surface. Comparing both images it becomes obvious that the surface is stronger attacked after 336 h of dissolution which is reflected by the increase of yellow and green areas. The dissolution proceeds especially along the polishing scratches. A roughness analysis is therefore not reasonable, because it cannot reflect the change according to the predominant dissolution mechanisms of the pyrochlore pellet.

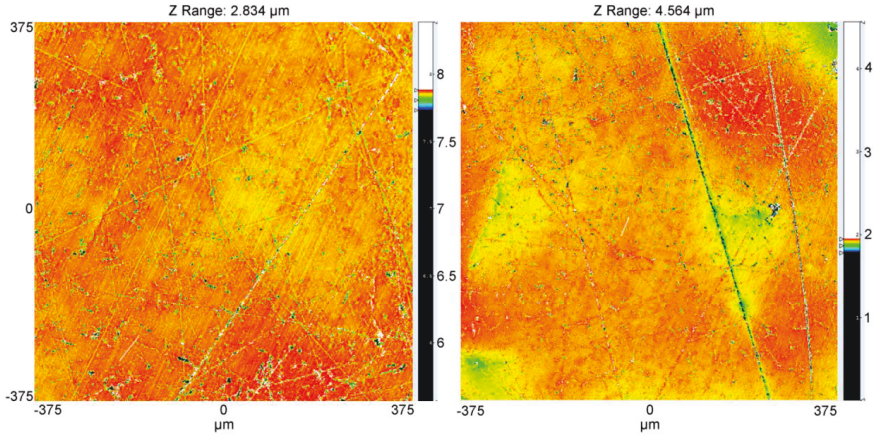

Figure 61: VSI image of a pyrochlore monolith sample (a) after 40 h of dissolution and (b) after 336 h of dissolution.

Figure 62 a shows the pellet surface after 40 h of dissolution. The green areas are about 1 µm in diameter, which correlates with the grain size of the pyrochlore samples as it could be seen in the SEM images (Figure 55b and Figure 56b).

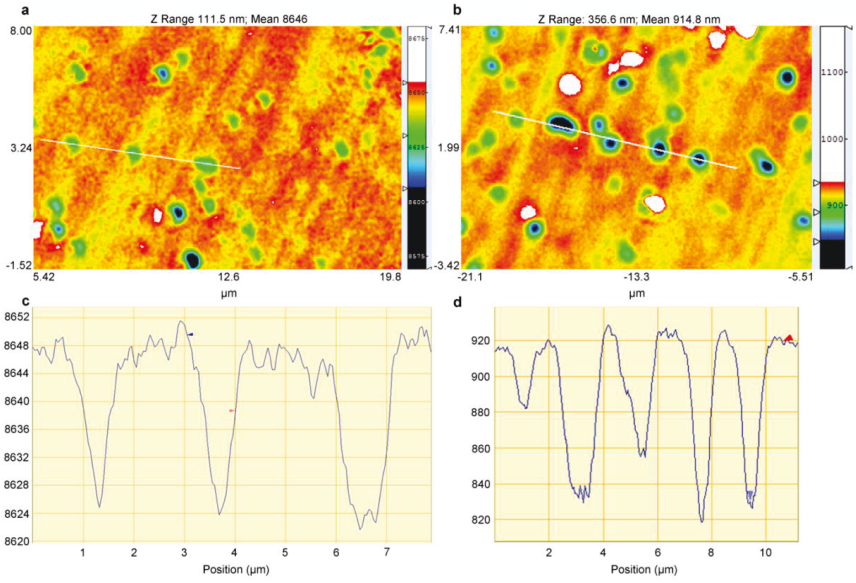

Figure 62: VSI image of a pyrochlore monolith surface (a) after 40 h and (b) 336 h of dissolution. Images (c) and (d) depict the depth profile corresponding to the white line drawn in the images above.

The depth profile shows a retreat of the grains of approximately 20 nm. Comparing 40 h of dissolution with 336 h of dissolution (Figure 62b) the frequency of the grains which are dissolving increases significantly. The number of grains which have retracted approximately 90 nm (black-blue areas) has also increased but there are also grains present which show a retraction of less than 60 nm. Most probably the grain retraction is a time dependent process. Why some grains start to dissolve earlier than others remains unclear so far. The mechanism of the dissolution of the grains clearly differs from the disintegration of the grains which was observed in the SEM studies. Figure 63a shows a much less attacked pellet surface after 40 h of dissolution compared to 336 h (b) of dissolution. The white rectangle in Figure 63b refers to the magnification in Figure 62b. From this image with a wider field of view it can be seen, that the detail of Figure 62 is representative for the whole pellet surface. Once again the heterogeneity of the dissolution at the pellet surface becomes obvious.

The VSI gives complementary information to the SEM, because the dissolution at the grain boundaries which could easily be observed by SEM cannot be seen in the VSI images. In contrast the VSI images make the dissolution at the grain surface itself visible.

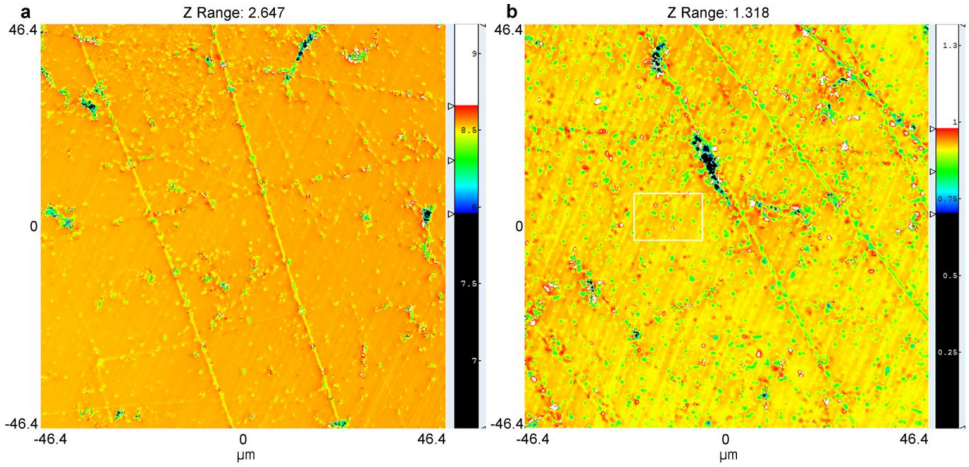

Figure 63: VSI image of a monolith pyrochlore (a) after 40 h and (b) 336 h of dissolution with a 92.8 µm field of view.

6 Conclusions and outlook

Within this study, three main aspects of zirconates with pyrochlore structure as potential nuclear waste form were examined, (1) phase stability field of pyrochlore and the consequences of non-stoichiometry, (2) structural uptake of radionuclides and (3) chemical stability and the effect of phase transformation to defect fluorite.

Phase stability field of pyrochlore and consequence of non-stoichiometry – A combined powder X-ray diffraction and TEM approach was chosen to define the phase boundaries of the pyrochlore stability field in the temperature range of 1400 to 1600 °C, which is the typical temperature regime for a ceramic formation. Based on XRD observation, pyrochlores exist in the compositional range between 20 and 37 mol% of Nd_2O_3. The phase boundary of pyrochlore on the low end of Nd_2O_3 is not well defined. A gradual transition from the pyrochlore to the defect fluorite is observed which can clearly be seen by the continuous trend of the lattice parameter through the complete compositional range from the stoichiometric pyrochlore to the defect fluorite. These findings are in good agreement with recent literature about the transition of pyrochlore to defect fluorite of similar and different chemical compositions [101-102]. On the Nd_2O_3 enriched end of the pyrochlore stability field, a two phase region of pyrochlore and defect fluorite clearly follows.

A detailed analysis of the XRD pattern supports the idea of a continuous phase transition as observed by the intensity change of the (331) pyrochlore superstructure reflex and the lattice distortion as a function of deviation from the stoichiometric pyrochlore composition. These parameters are directly accessible from XRD pattern. An antisite model of cationic ordering was applied to describe the average structures of the non-stoichiometric pyrochlores. The ratio of the effective cationic radii directly correlates with the (331) intensity.

Complementary TEM investigations were carried out to study the effect of the phase transformation on the local structure of pyrochlore and defect fluorite. Electron diffraction pattern along different zone axis of a stoichiometric pyrochlore already showed non-ideal pyrochlore diffraction pattern. Results of theoretical reflex calculations and preliminary quantum-mechanical calculation carried out by Piotr Kowalski indicate an energetically favoured anion disorder by occupying the usually vacant 8a site. With decreasing Nd_2O_3 content, a gradual transition from the stoichiometric to the non-stoichiometric pyrochlores to the defect fluorite was observed. This transformation is not uniform in all crystallographic directions and involves anionic and cationic disorder. However, even for the sample which was identified as defect fluorite by XRD, the transformation is incomplete and certain pyrochlore superstructure reflexes remain.

Structural uptake of radionuclides – The results of TRLFS on Eu and Cm doped $La_2Zr_2O_7$ pyrochlore showed a structural uptake of both cations at the A site of the pyrochlore and on a regular cation lattice site in defect fluorite. In addition, a minor species is present in the pyrochlore which was identified to be identical to the main species observed in the defect fluorite. Vice versa, the defect fluorite contains a minor species which has adapted the pyrochlore environment. This is in good agreement with the findings of TEM. Due to the different pyrochlore and defect fluorite species, TRLFS could be used as a tool to quantify radiation damage in ZrO_2 based pyrochlore nuclear waste forms.
In order to get closer to a real waste form Pu-pyrochlores were synthesised by a wet chemical synthesis route that was transferred from the inactive pyrochlores. Characterisation by XRD, SEM and EDX indicates a homogeneous structural uptake of Pu-239 into pyrochlore.

Chemical stability and effect of phase transformation to defect fluorite – A combined macroscopic and microscopic approach was followed to study the dissolution of ZrO_2 – Nd_2O_3 ceramics. Macroscopic dissolution rates in a range between 10^{-5} and 10^{-7} $gm^{-2}d^{-1}$ were determined as a function of temperature, pH and chemical composition following a dynamic and static experimental setup. Both experimental approaches are in good accordance. Typical for all experiments is a preferential release of Nd. This may be explained due to the insolubility of Zr which could eventually cause the transformation of metastable pyrochlore to the room temperature phase ZrO_2 instead of complete dissolution. This could lead to the formation of leached layers due to preferential dissolution of Nd.
The pH and temperature dependence of the dissolution rate is similar for both, defect fluorite and pyrochlore and in a similar range as observed for other oxides. The activation energies are typical for surface controlled dissolution. Only slight differences were determined in the macroscopic dissolution rates as a function of chemical composition, with an increase of the steady state dissolution rate close to the pyrochlore phase boundaries. Similar trends of structural properties e.g. strain and the dissolution rates as a function of the pyrochlore chemical composition were found.
Complementary microscopic observation using SEM and VSI on powder and monolith samples indicates a preferential dissolution at the grain boundaries. A temporal evolution of the surface reactivity was noted. The initial phase of dissolution is dominated by dissolution at triple junctions which then stops. In contrast to SEM, the observation with VSI indicates a surface retreat of individual grains. With time, the number of retreating grains increases as well as the number of reactive grain boundaries.
Extrapolating the macroscopic dissolution rates to the near neutral pH-range and room temperature relevant for nuclear waste disposal leads to very low dissolution rates in the

order of 10^{-10} $gm^{-2}d^{-1}$. Disintegration of the grains due to preferential dissolution at the grain boundaries would lead to an increase of the reactive surface area. However, the dissolution at the individual grain surfaces is lower than at the grain boundaries, which should compensate for the increase of the surface area.

As a result of the study presented here several open questions concerning the properties of zirconate based pyrochlore as potential nuclear waste form could be answered, which are related to the phase transition, radionuclide uptake and chemical stability.
ZrO_2 based pyrochlores are known to undergo a phase transition to defect fluorite as consequence of irradiation. This phase transformation to the less ordered, but still crystalline defect fluorite structure is gradual and proven to have no significant impact on the aqueous durability under acidic conditions. In addition to their high radiation tolerance ZrO_2 based pyrochlores are therefore expected to ensure high long-term durability even during the decay of embedded radionuclides. Moreover, the radionuclide uptake on well-defined lattice positions within the pyrochlore crystal structure was probed and a suitable synthesis route adapted to fabricate ZrO_2 based Pu-pyrochlore pellets with a Pu content considered to be realistic for a nuclear waste form. Extensive dissolution studies including variations of pH, temperature and chemical composition allowed an estimation of a dissolution rate in the order of 10^{-10} $gm^{-2}d^{-1}$ under repository relevant conditions. The combination of macroscopic and microscopic approaches allowed first insight into the dissolution mechanism of a systematic ZrO_2 – Nd_2O_3 pyrochlore series.

Outlook – The results presented in this work provide a solid basis for more detailed future studies. A well characterised suite of samples of the ZrO_2 – Nd_2O_3 pyrochlore series now can be used for a combined experimental and theoretical work. The combination of XRD, TEM and EXAFS data with atomistic simulations will enable an understanding on a truly molecular level of this order – disorder transition. Preliminary results of this approach have already proven to be useful during this study.
Another aspect will be a detailed, local analysis of the Pu site within the pyrochlore crystal structure and the Pu oxidation state using EXAFS and XANES. A successful proposal was submitted during this study to the INE beamline at the ANKA facility, Karlsruhe.
Dissolution studies are planned to be extended to the actinide bearing pyrochlores using the Pu-pyrochlore pellets synthesised within this work. A pre-requisite for a process understanding of the dissolution kinetics of the Pu-pyrochlore will be a thorough characterisation of these samples including a refined structural model.

7 Appendix

Table 13: Purity and supplier of the used chemicals.

Substance	Purity	Supplier
acetone	p.a.	Roth
ammonia	3.8	Messer Griesheim GmbH
liquid ammonia 25%	p.a.	Roth
argon	5.7	Praxair
acetic acid 96%	p.a.	Riedel de Haën
europium nitrate	99.9%	Alfa Aesar
urea	p.a.	Merck
hexamethylenetetramine	p. a.	Merck
hydrochloric acid 37%		Merck
lanthanum(III)nitrate hexahydrate	p.a.	Fluka analytical
neodymium(III)nitraet hexahydrate	99.9 %	Alfa Aesar
nitric acid 65%	p.a.	Merck
petroleum ether	p.a.	Roth
potassium hydroxide	p.a.	Merck
zirconyl chloride octahydrate	99.9 %	Alfa Aesar

Table 14: Position and fluorescence lifetime of Cm and Eu species within the defect fluorite and pyrochlore crystal structure. The number of water molecules in the first coordination sphere were calculated by the Horrocks and Kimura equation. Results are published in Holliday et al. (2013) [111].

Site	Structure	Position [nm]	Lifetime [ms]	Water
Eu (major)	Pyrochlore	575.6	4.0	-0.3
Cm (major)	Pyrochlore	632.0	1.0	-0.2
Eu (minor)	Defect fluorite	575.7	3.6	-0.3
Cm (minor)	Defect fluorite	632.0	1.1	-0.3
Eu (major)	Defect fluorite	579.6	1.0	0.4
Cm (major)	Defect fluorite	639.0	0.38	0.8
Eu (minor)	Pyrochlore	578.7	1.1	0.4
Cm (minor)	Pyrochlore	626.0	0.16	3.2

Table 15: Calcination and sintering duration for the different Pu-pyrochlores.

Sample	Mass (mg)	Calcination heating rate	Sintering duration	Sintering heating rate
SF-71-P1	292.9	300 °C/h	10 h & 15 h	200 °C/h
SF-74-P1	348.6	200 °C/h	25 h	200 °C/h
SF-74-P2	302.7	200 °C/h	80 h	100 °C/h (h), 200 °C/h (c)
SF-77-P1	80.9	100 °C/h (h), 200 °C/h (c)	80 h	100 °C//h (h), 200 °C/h (c)
			5 h	repressing after XRD same heating rates as previously
SF-77-P2	179.6		80 h	100 °C//h (h), 200 °C/h (c)

With (h) heating rate and (c) cooling rate.

Table 16: Normalised Zr- and Nd-based dissolution rates R of pyrochlore and defect fluorite in 0.1 mol/L HCl at 90 °C.

Nd_2O_3 content (mol%)	Crystal structure	Type of experiment		R(Nd) ($g \cdot m^{-2} \cdot d^{-1}$)	R(Zr) ($g \cdot m^{-2} \cdot d^{-1}$)
33.3	Pyrochlore	Batch	Initial	$3.26 \cdot 10^{-5}$	---
			Final	$1.95 \cdot 10^{-5}$	---
33.3	Pyrochlore	Dynamic	Initial	$9.15 \cdot 10^{-4}$	$6.85 \cdot 10^{-6}$
			Steady state	$8.37 \cdot 10^{-6}$	$3.76 \cdot 10^{-6}$
12.9	Defect fluorite	Dynamic	Initial	$3.68 \cdot 10^{-4}$	$2.83 \cdot 10^{-6}$
			Steady state	$6.27 \cdot 10^{-7}$	$1.00 \cdot 10^{-6}$

Table 17: Dissolution rates of pyrochlore and defect fluorite samples obtained at 90 °C and c(H^+) = 0.1n. This results are published in Finkeldei et al (2013) [118] and Finkeldei et al (2014) [119].

Nd_2O_3 (mol%)	Crystal structure	Initial rate (Nd) (g m^{-2} d^{-1})	Steady state $rate_{max}$ (Nd) (g m^{-2} d^{-1})	Steady state $rate_{min}$ (Nd) (g m^{-2} d^{-1})	Initial rate (Zr) (g m^{-2} d^{-1})	Steady state $rate_{max}$ (Zr) (g m^{-2} d^{-1})	Steady state $rate_{min}$ (Zr) (g m^{-2} d^{-1})
12.9	Defect Fluorite	1.0×10^{-3}	4.2×10^{-6}	1.1×10^{-6}	2.0×10^{-6}	5.0×10^{-7}	4.7×10^{-7}
15.6	Defect Fluorite	7.9×10^{-4}	6.5×10^{-6}	5.0×10^{-7}	1.9×10^{-6}	1.8×10^{-6}	6.7×10^{-7}
17.6	Defect Fluorite	3.9×10^{-4}	2.4×10^{-6}	1.3×10^{-6}	3.3×10^{-6}	6.9×10^{-7}	5.4×10^{-7}
22.0	Pyrochlore	2.4×10^{-3}	1.2×10^{-5}	2.4×10^{-6}	2.1×10^{-6}	1.0×10^{-6}	
25.0	Pyrochlore	2.2×10^{-4}	1.7×10^{-6}	8.3×10^{-7}	2.2×10^{-6}	1.0×10^{-6}	3.6×10^{-7}
33.3 (PY-2)	Pyrochlore	4.4×10^{-6}	2.0×10^{-6}		9.2×10^{-6}	1.3×10^{-6}	
33.3 (PY-1)	Pyrochlore	1.2×10^{-3}	4.4×10^{-6}		1.6×10^{-5}	2.9×10^{-6}	
35.1	Pyrochlore	2.0×10^{-3}	1.2×10^{-5}		2.0×10^{-5}	2.8×10^{-6}	

8 List of figures

9 List of tables

10 References

[1] Minhans, A.; Neles, J.; Schmidt, G. Endlagerung wärmeentwickelnder radioaktiver Abfälle in Deutschland, Anhang Entsorgungsstrategien, Darstellung und Bewertung von Alternativen zur Endlagerung; Anhang zu GRS-247; Öko Institut e.V., GRS; Braunschweig / Darmstadt; **2008**.

[2] Lumpkin, G.R. Ceramic waste forms for actinides. Elements **2006**, *2* (6), 365-372.

[3] Ringwood, A.E.; Kesson, S.E.; Ware, N.G.; Hibberson, W.; Major, A. Immobilisation of high level nuclear reactor wastes in SYNROC. Nature **1979**, *278* (5701), 219-223.

[4] Ringwood, A.E.; Kesson, S.E.; Reeve, K.D.; Levins, D.M.; Ramm, E.J. SYNROC. Chap. 4 in Radioactive waste forms for the future, Lutze, W.; Ewing, R.C., North-Holland: Amsterdam, p 778, **1988**.

[5] Ewing, R.C.; Weber, W.J.; Lian, J. Nuclear waste disposal-pyrochlore ($A_2B_2O_7$): nuclear waste form for the immobilization of plutonium and "minor" actinides. J. Appl. Phys. **2004**, *95*, 5949-5971.

[6] Lian, J.; Chen, J.; Wang, L.M.; Ewing, R.C.; Farmer, J.M.; Boatner, L.A.; Helean, K.B. Radiation-induced amorphization of rare-earth titanate pyrochlores. Physical Review B **2003**, *68* (13), 134107.

[7] Greneche, D.; Quiniou, B.; Boucher, L.; Delpech, M.; Gonzalez, E.; Alvalrez, F.; A.Cunado, M.; Serrano, G.; Cormenzana, J.L.; Kuckshinrichs, W.; Odoj, R.; von Lensa, W.; Wallenius, J.; Westlén, D.; Zimmermann, C.; Marivoet, J., RED-IMPACT impact of partitioning, transmutation and waste reduction technologies on the final nuclear waste disposal. Forschungszentrum Jülich GmbH: Jülich, **2008**; Vol. 15.

[8] Hamilton, L.H.; Scowcroft, B.; Ayers, M.H.; Bailey, V.A.; Carnesale, A.; Domenici, P.; Eisenhower, S.; Hagel, C.; Lash, J.; Macfarlane, A.M.; Meserve, R.A.; Moniz, E.J.; Peterson, P.; Rowe, J.; Sharp, P. Blue Ribbon Commission on America's Nuclear Future - report to the secretary of energy; Blue Ribbon Commission on America's Nuclear Future; **2012**.

[9] World Nuclear News UK government increases control of civil plutonium. http://www.world-nuclear-news.org/WR-UK-government-increases-control-of-civil-plutonium-03071401.html (accessed 03.09.2014).

[10] Donald, I.W.; Metcalfe, B.L.; Taylor, R.N.J. The immobilization of high level radioactive wastes using ceramics and glasses. J. Mater. Sci. **1997**, *32*, 5851-5887.

[11] Ewing, R.C.; Weber, W.J.; Lian, J. Nuclear waste disposal-pyrochlore ($A_2B_2O_7$): nuclear waste form for the immobilization of plutonium and "minor" actinides. Journal of Applied Physics **2004**, *95* (11), 5949-5971.

[12] Appel, D.; Baltes, B.; Bräuer, V.; Brewitz, W.; Duphorn, K.; Gömmel, R.; Haury, H.-J.; Ipsen, D.; Jentzsch, G.; Kreusch, J.; Kühn, K.; Lux, K.-H.; Sailer, M.; Thomauske, B. Auswahlverfahren für Endlagerstandorte, Empfehlungen des AkEnd - Arbeitskreis Auswahlverfahren Endlagerstandorte; Köln; **2002**.

[13] Mengel, K.; Röhlig, K.-J.; Geckeis, H. Endlagerung radioaktiver Abfälle. Chem. unserer Zeit **2012**, *46* (4), 208-217.

[14] OECD NEA Radioactive waste management programmes in OECD/NEA member countries united states; **2011**.

[15] Holleman, A.F.; Wiberg, E.; Wiberg, N., Lehrbuch der anorganischen Chemie. 91.-100., verb. und stark erw. ed.; Berlin: de Gruyter, **1985**; p 1067.

[16] Rouanet, A. Contribution to study of zirconium-oxides systems of lanthanides close to melting point. Revue Internationale Des Hautes Temperatures Et Des Refractaires **1971**, *8* (2), 161.

[17] Fabrichnaya, O.; Seifert, H.J. Assessment of thermodynamic functions in the ZrO_2–Nd_2O_3–Al_2O_3 system. Calphad **2008**, *32* (1), 142-151.

[18] Binnewies, M.; Jäckel, M.; Willner, H.; Rayner-Canham, G., Allgemeine und Anorganische Chemie. 1. ed.; Spektrum Akad. Verl.: München, **2004**.

[19] Hartmann, T.; Alaniz, A.J.; Antonio, D.J. Fabrication and properties of technetium-bearing pyrochlores and perovskites as potential waste forms. Procedia Chemistry **2012**, *7* (0), 622-628.

[20] Claparede, L.; Clavier, N.; Dacheux, N.; Mesbah, A.; Martinez, J.; Szenknect, S.; Moisy, P. Multiparametric dissolution of thorium–cerium dioxide solid solutions. Inorganic Chemistry **2011**, *50* (22), 11702-11714.

[21] Finkeldei, S. Darstellung und Charakterisierung ZrO_2 und ThO_2 basierter Keramiken für die nukleare Entsorgung. RWTH Aachen, **2011**.

[22] Chen, H.F.; Gao, Y.F.; Liu, Y.; Luo, H.J. Coprecipitation synthesis and thermal conductivity of $La_2Zr_2O_7$. Journal of Alloys and Compounds **2009**, *480* (2), 843-848.

[23] Schmidt, H.K. Anorganische Synthesemethoden Das Sol-Gel-Verfahren. Chemie in unserer Zeit **2001**, *3*, 176-184.

[24] Nästren, C.; Jardin, R.; Somers, J.; Walter, M.; Brendebach, B. Actinide incorporation in a zirconia based pyrochlore $(Nd_{1.8}An_{0.2})Zr_2O_{7+x}$ (An = Th, U, Np, Pu, Am). Journal of Solid State Chemistry **2009**, *182* (1), 1-7.

[25] Wiss, T.A.G.; Hiernaut, J.P.; Damen, P.M.G.; Lutique, S.; Fromknecht, R.; Weber, W.J. Helium behaviour in waste conditioning matrices during thermal annealing. Journal of Nuclear Materials **2006**, *352* (1-3), 202-208.

[26] Subramanian, M.A.; Aravamudan, G.; Rao, G.V.S. Oxide pyrochlores - a review. Progress in Solid State Chemistry **1983**, *15* (2), 55-143.

[27] Chakoumakos, B.C. Pyrochlore. in McGraw-Hill Yearbook of Science & Technology 1987, Parker, S.P., McGraw-Hill: New York, pp 393-395, **1987**.

[28] Hogarth, D.D. Classification and nomenclature of pyrochlore group. American Mineralogist **1977**, *62* (5-6), 403-410.

[29] Ewing, R.C. Safe management of actinides in the nuclear fuel cycle: role of mineralogy. Comptes Rendus Geoscience **2011**, *343* (2-3), 219-229.

[30] Icenhower, J.P.; Strachan, D.M.; McGrail, B.P.; Scheele, R.A.; Rodriguez, E.A.; Steele, J.L.; Legore, V.L. Dissolution kinetics of pyrochlore ceramics for the disposition of plutonium. American Mineralogist **2006**, *91* (1), 39-53.

[31] Jiang, C.; Stanek, C.R.; Sickafus, K.E.; Uberuaga, B.P. First-principles prediction of disordering tendencies in pyrochlore oxides. Physical Review B **2009**, *79* (10), 104203.

[32] Knop, O.; Brisse, F.; Castelliz, L.; Sutarno Determination of the crystal structure of erbium titanate, $Er_2Ti_2O_7$, by X-ray and neutron diffracton. Can. J. Can. Chem. **1965**, *43*, 2812-2826.

[33] Pöml, P.; Menneken, M.; Stephan, T.; Niedermeier, D.R.D.; Geisler, T.; Putnis, A. Mechanism of hydrothermal alteration of natural self-irradiated and synthetic crystalline titanate-based pyrochlore. Geochimica et Cosmochimica Acta **2007**, *71* (13), 3311-3322.

[34] Shoup, S.S.; Bamberger, C.E.; Haire, R.G. Novel plutonium titanate compounds and solid solutions $Pu_2Ti_2O_7$-$Ln_2Ti_2O_7$: relevance to nuclear waste disposal. Journal of the American Ceramic Society **1996**, *79* (6), 1489-1493.

[35] Strachan, D.M.; Scheele, R.D.; Buck, E.C.; Icenhower, J.P.; Kozelisky, A.E.; Sell, R.L.; Elovich, R.J.; Buchmiller, W.C. Radiation damage effects in candidate titanates for Pu disposition: pyrochlore. Journal of Nuclear Materials **2005**, *345* (2–3), 109-135.

[36] Harvey, E.J.; Whittle, K.R.; Lumpkin, G.R.; Smith, R.I.; Redfern, S.A.T. Solid solubilities of $(La,Nd)_2(Zr,Ti)_2O_7$ phases deduced by neutron diffraction. Journal of Solid State Chemistry **2005**, *178* (3), 800-810.

[37] Cullity, B.D.; Stock, S.R., Elements of X-ray diffraction. 3rd ed.; Prentice Hall: Upper Saddle River, NJ, **2001**.

[38] Nelson, J.B.; Riley, D.P. An experimental investigation of extrapolation methods in the derivation of accurate unit-cell dimensions of crystals. Proc. Phys. Soc., London **1945**, *57*, 160-177.

[39] Klug, H.P.; Alexander, L.E., X-ray diffraction procedures for polycrystalline and amorphous materials. Wiley: New York, **1954**.

[40] Williamson, G.K.; Hall, W.H. X-ray line broadening from filed aluminium and wolfram. Acta Metallurgica **1953**, *1* (1), 22-31.

[41] Putnis, A., Introduction to mineral sciences. Cambridge University Press: Cambridge, **1993**.

[42] Williams, D.B.; Carter, C.B., Transmission electron microscopy : a textbook for materials science 2nd ed.; Springer: New York, NY, **2009**.

[43] Putnis, A., Introduction to mineral sciences. Cambridge University Press: Cambridge, **1992**.

[44] Beitz, J.V. Laser-induced fluorescence studies of Cm^{3+} complexes in solution. Radiochimica Acta **1991**, *52-53*, 35-39.

[45] Horrocks, W.D.; Sudnick, D.R. Lanthanide ion probes of structure in biology - laser-induced luminescence decay constants provide a direct measure of the number of metal-coordinated water-molecules. Journal of the American Chemical Society **1979**, *101* (2), 334-340.

[46] Kimura, T.; Choppin, G.R. Luminescence study on determination of the hydration number of Cm(III). Journal of Alloys and Compounds **1994**, *213*, 313-317.

[47] Buenzli, J.-C.G., Lanthanide probes in life, chemical and earth sciences : theory and practice. Elsevier: Amsterdam, **1989**; p 219-293.

[48] Icenhower, J.P.; Strachan, D.M.; Lindberg, M.M.; Rodriguez, E.A.; Steele, J.L. Dissolution kinetics of titanate-based ceramic waste forms: results from single-pass flow tests on radiation damaged specimens; **2003**.

[49] Gregg, D.J.; Zhang, Y.J.; Middleburgh, S.C.; Conradson, S.D.; Triani, G.; Lumpkin, G.R.; Vance, E.R. The incorporation of plutonium in lanthanum zirconate pyrochlore. Journal of Nuclear Materials **2013**, *443* (1-3), 444-451.

[50] Toth, L.M.; Friedman, H.A.; Osborne, M.M. Polymerization of Pu(IV) in aqueous nitric acid solutions. Journal of Inorganic & Nuclear Chemistry **1981**, *43* (11), 2929-2934.

[51] Walther, C.; Rothe, J.; Brendebach, B.; Fuss, M.; Altmaier, M.; Marquardt, C.M.; Buechner, S.; Cho, H.R.; Yun, J.I.; Seibert, A. New insights in the formation processes of Pu(IV) colloids. Radiochimica Acta **2009**, *97* (4-5), 199-207.

[52] Coleman, G.H. The radiochemistry of plutonium; AEC Contract No. W-7405-eng-48; University of California, Lawrence Radiation Laboratory Livermire, California; **1965**.

[53] Drummond, J.L.; Welch, G.A. The preparation and properties of some plutonium compounds. Part IV. Crystalline plutonium nitrate. Journal of the Chemical Society **1956**, (JUL), 2565-2566.

[54] Lasaga, A.C., Kinetic theory in the earth sciences. Princeton University Press: Princeton, **1998**.

[55] Lasaga, A.C. Fundamental approaches in describing mineral dissolution and precipitation rates. Chap. 2 in Chemical weathering rates of silicate minerals, Vol. 31, White, A.F., Mineralogical Society of America: Washington, D.C., pp 23-86, **1995**.

[56] Horlait, D.; Tocino, F.; Clavier, N.; Dacheux, N.; Szenknect, S. Multiparametric study of $Th_{1-x}Ln_xO_{2-x/2}$ mixed oxides dissolution in nitric acid media. Journal of Nuclear Materials **2012**, *429* (1–3), 237-244.

[57] Brantley, S.L. Kinetics of mineral dissolution. Chap. 5 in Kinetics of Water-Rock Interaction, Brantley, S.L.; Kubicki, J.D.; White, A.F., Springer: New York, **2008**.

[58] Oelkers, E.H. General kinetic description of multioxide silicate mineral and glass dissolution. Geochimica et Cosmochimica Acta **2001**, *65* (21), 3703-3719.

[59] Kossel, W. Zur Theorie des Kristallwachstums. Nachr. Akad. Wiss. Göttingen, math.-phys. Kl **1927**, 135-143.

[60] Stranski, I.N. Zur Theorie des Kristallwachstums. Zeitschrift für Physikalische Chemie Stöchiometrie Und Verwandtschaftslehre **1928**, *136* (3/4), 259-278.

[61] Frank, F.C. The influence of dislocations on crystal growth; Discuss. Faraday Soc.; **1949**.

[62] Kubicki, J.D. Transition state theory and molecular orbital calculations applied to rates and reaction mechanisms in geochemical kinetics. Chap. 2 in Kinetics of Water-Rock Interaction, Brantley, S.L.; Kubicki, J.D.; White, A.F., Springer: New York, **2008**.

[63] Furrer, G.; Stumm, W. The coordination chemistry of weathering: I. Dissolution kinetics of δ-Al_2O_3 and BeO. Geochimica Et Cosmochimica Acta **1986**, *50* (9), 1847-1860.

[64] Brantley, S.L. Reaction kinetics of primary rock-forming minerals under ambient conditions. in Treatise on geochemistry, Holland, H.D.; Turekian, K.K., pp 73-117, **2003**.

[65] Guy, C.; Schott, J. Multisite surface reaction versus transport control during the hydrolysis of a complex oxide. Chemical Geology **1989**, *78* (3-4), 181-204.

[66] Carroll-Webb, S.A.; Walther, J.V. A surface complex reaction model for the pH-dependence of corundum and kaolinite dissolution rates. Geochimica et Cosmochimica Acta **1988**, *52* (11), 2609-2623.

[67] Schott, J.; Oelkers, E.H.; Bénézeth, P.; Goddéris, Y.; François, L. Can accurate kinetic laws be created to describe chemical weathering? Comptes Rendus Geoscience **2012**, *344* (11–12), 568-585.

[68] Brantley, S.L.; Mellott, N.P. Surface area and porosity of primary silicate minerals. American Mineralogist **2000**, *85* (11-12), 1767-1783.

[69] Helgeson, H.C.; Murphy, W.M.; Aagaard, P. Thermodynamic and kinetic constraints on reaction-rates among minerals and aqueous-solutions. II. Rate constants, effective surface-area, and the hydrolysis of feldspar. Geochimica Et Cosmochimica Acta **1984**, *48* (12), 2405-2432.

[70] Holdren, G.R.; Speyer, P.M. Reaction rate-surface area relationships during the early stages of weathering: II. Data on eight additional feldspars. Geochimica Et Cosmochimica Acta **1987**, *51* (9), 2311-2318.

[71] Rufe, E.; Hochella, M.F. Quantitative assessment of reactive surface area of phlogopite during acid dissolution. Science **1999**, *285* (5429), 874-876.

[72] Bickmore, B.R.; Bosbach, D.; Hochella, M.F.; Charlet, L.; Rufe, E. In situ atomic force microscopy study of hectorite and nontronite dissolution: Implications for phyllosilicate edge surface structures and dissolution mechanisms. American Mineralogist **2001**, *86* (4), 411-423.

[73] Brandt, F.; Bosbach, D.; Krawczyk-Bärsch, E.; Arnold, T.; Bernhard, G. Chlorite dissolution in the acid ph-range: a combined microscopic and macroscopic approach. Geochimica et Cosmochimica Acta **2003**, *67* (8), 1451-1461.

[74] Luettge, A.; Arvidson, R.; Fischer, C.; Luttge, A. A stochastic treatment of crystal dissolution kinetics. Elements **2013**, *9* (3), 183-188.

[75] Bosbach, D.; Hochella Jr, M.F. Gypsum growth in the presence of growth inhibitors: a scanning force microscopy study. Chemical Geology **1996**, *132* (1–4), 227-236.

[76] Peruffo, M.; Mbogoro, M.M.; Edwards, M.A.; Unwin, P.R. Holistic approach to dissolution kinetics: linking direction-specific microscopic fluxes, local mass transport effects and global macroscopic rates from gypsum etch pit analysis. Physical Chemistry Chemical Physics **2013**, *15* (6), 1956-1965.

[77] Lasaga, A.C.; Luettge, A. Variation of crystal dissolution rate based on a dissolution stepwave model. Science **2001**, *291* (5512), 2400-2404.

[78] Oelkers, E.H.; Poitrasson, F. An experimental study of the dissolution stoichiometry and rates of a natural monazite as a function of temperature from 50 to 230 °C and pH from 1.5 to 10. Chemical Geology **2002**, *191* (1-3), 73-87.

[79] Dacheux, N.; de Kerdaniel, E.D.F.; Clavier, N.; Podor, R.; Aupiais, J.; Szenknect, S. Kinetics of dissolution of thorium and uranium doped britholite ceramics. Journal of Nuclear Materials **2010**, *404* (1), 33-43.

[80] Rimstidt, J.D.; Dove, P.M. Mineral solution reaction-rates in a mixed flow reactor - wollastonite hydrolysis. Geochimica Et Cosmochimica Acta **1986**, *50* (11), 2509-2516.

[81] Neeway, J.; Abdelouas, A.; Grambow, B.; Schumacher, S. Dissolution mechanism of the SON68 reference nuclear waste glass: new data in dynamic system in silica saturation conditions. Journal of Nuclear Materials **2011**, *415* (1), 31-37.

[82] Berger, G.; Claparols, C.; Guy, C.; Daux, V. Dissolution rate of a basalt glass in silica-rich solutions - implications for long-term alteration. Geochimica Et Cosmochimica Acta **1994**, *58* (22), 4875-4886.

[83] Dove, P.M.; Crerar, D.A. Kinetics of quartz dissolution in electrolyte-solutions using a hydrothermal mixed flow reactor. Geochimica Et Cosmochimica Acta **1990**, *54* (4), 955-969.

[84] Chou, L.; Wollast, R. Study of weathering of albite at room-temperature and pressure with a fluidized-bed reactor. Geochimica Et Cosmochimica Acta **1984**, *48* (11), 2205-2217.

[85] Nagy, K.L.; Lasaga, A.C. Dissolution and precipitationn kinetics of gibbsite at 80 °C and pH 3: the dependence on solution saturation state. Geochimica Et Cosmochimica Acta **1992**, *56* (8), 3093-3111.

[86] Kulik, D. *GEM-Selektor. Research package for thermodynamic modelling of aquatic (geo)chemical systems by Gibbs Energy Minimization (GEM). http://gems.web.psi.ch*.

[87] Kulik, D.A.; Wagner, T.; Dmytrieva, S.V.; Kosakowski, G.; Hingerl, F.F.; Chudnenko, K.V.; Berner, U.R. GEM-Selektor geochemical modeling package: revised algorithm and GEMS3K numerical kernel for coupled simulation codes. Computational Geosciences **2013**, *17* (1), 1-24.

[88] Wagner, T.; Kulik, D.A.; Hingerl, F.F.; Dmytrieva, S.V. GEM-Selektor geochemical modeling package: TSolMod library and data interface for multicomponent phase models. Canadian Mineralogist **2012**, *50* (5), 1173-1195.

[89] Davies, C.W., Ion association. Butterworths: Washington, D.C., **1962**.

[90] Jacob, K.T.; Dasgupta, N.; Waseda, Y. Composition-graded solid electrolyte for determination of the Gibbs energy of formation of lanthanum zirconate. Journal of the American Ceramic Society **1998**, *81* (7), 1926-1930.

[91] Lutique, S.; Javorský, P.; Konings, R.J.M.; van Genderen, A.C.G.; van Miltenburg, J.C.; Wastin, F. Low temperature heat capacity of $Nd_2Zr_2O_7$ pyrochlore. The Journal of Chemical Thermodynamics **2003**, *35* (6), 955-965.

[92] Lutique, S.; Konings, R.J.M.; Rondinella, W.; Somers, J.; Wiss, T. The thermal conductivity of $Nd_2Zr_2O_7$ pyrochlore and the thermal behaviour of pyrochlore-based inert matrix fuel. Journal of Alloys and Compounds **2003**, *352* (1-2), 1-5.

[93] Diakonov, II; Ragnarsdottir, K.V.; Tagirov, B.R. Standard thermodynamic properties and heat capacity equations of rare earth hydroxides: II. Ce(III)-, Pr-, Sm-, Eu(III)-, Gd-, Tb-, Dy-, Ho-, Er-, Tm-, Yb-, and Y-hydroxides. Comparison of thermochemical and solubility data. Chemical Geology **1998**, *151* (1-4), 327-347.

[94] Lide, D., CRC Handbook of chemistry and physics, 88th Edition (CRC Handbook of chemistry & physics). CRC Press: **2007**.

[95] Hummel, W.; Berner, U.; Curti, E.; Pearson, F.J.; Thoenen, T. Nagra/PSI chemical thermodynamic data base 01/01. Radiochimica Acta **2002**, *90* (9-11), 805-813.

[96] Shock, E.L.; Sassani, D.C.; Willis, M.; Sverjensky, D.A. Inorganic species in geologic fluids: correlations among standard molal thermodynamic properties of aqueous ions and hydroxide complexes. Geochimica Et Cosmochimica Acta **1997**, *61* (5), 907-950.

[97] Bryan, G.H.; Thompson, J.K.; Van Tuyl, H.H.; Brown, C.L.; Ryan, J.L. Results of research to evaluate solid plutonium nitrate as a safe shipping form; **1976**.

[98] van Dijk, M.P. Electrical and catalytical properties of some oxides with the fluorite or pyrochlore structure. Mat. Res. Bull. **1984**, *19*, 1149-1156.

[99] Icenhower, J.P.; McGrail, B.P.; Schaef, H.T.; Rodriguez, E.A. Dissolution kinetics of titanium pyrochlore ceramics at 90 °C by single pass flow-through experiments, Proceedings of Materials Research Society **2000**, Vol. 608, pp 373-378.

[100] Strakhov, V.I.; Klyuchar.Yv; Sergeev, G.G. ZrO_2 and Nd_2O_3 interactions in isothermal processing conditions. Zhurnal Prikladnoi Khimii **1973**, *46* (9), 2083-2085.

[101] Payne, J.L.; Tucker, M.G.; Evans, I.R. From fluorite to pyrochlore: characterisation of local and average structure of neodymium zirconate, $Nd_2Zr_2O_7$. Journal of Solid State Chemistry **2013**, *205*, 29-34.

[102] Zhang, Z.M.; Middleburgh, S.C.; de los Reyes, M.; Lumpkin, G.R.; Kennedy, B.J.; Blanchard, P.E.R.; Reynolds, E.; Jang, L.Y. Gradual structural evolution from pyrochlore to defect-fluorite in $Y_2Sn_{2-x}Zr_xO_7$: average vs local structure. Journal of Physical Chemistry C **2013**, *117* (50), 26740-26749.

[103] Chakoumakos, B.C. Systematics of the pyrochlore structure type, ideal $A_2B_2X_6Y$. Journal of Solid State Chemistry **1984**, *53* (1), 120-129.

[104] McCauley, R.A. Structural characteristics of pyrochlore formation. Journal of Applied Physics **1980**, *51* (1), 290-294.

[105] Minervini, L.; Grimes, R.W.; Tabira, Y.; Withers, R.L.; Sickafus, K.E. The oxygen positional parameter in pyrochlores and its dependence on disorder. Philosophical Magazine A **2002**, *82* (1), 123-135.

[106] Shannon, R.D. Revised effective ionic-radii and systematic studies of interatomic distances in halides and chalcogenides. Acta Crystallographica Section A **1976**, *32*, 751-767.

[107] Reid, D.P.; Stennett, M.C.; Hyatt, N.C. The fluorite related modulated structures of the $Gd_2(Zr_{2-x}Ce_x)O_7$ solid solution: an analogue for Pu disposition. Journal of Solid State Chemistry **2012**, *191*, 2-9.

[108] Kowalski, P., Preliminary calculations of defect formation energies in pyrochlore. **2014**.

[109] Ubic, R.; Abrahams, I.; Hu, Y. Oxide ion disorder in $Nd_2Hf_2O_7$. Journal of the American Ceramic Society **2008**, *91* (1), 235-239.

[110] Withers, R.L.; Thompson, J.G.; Barlow, P.J.; Barry, J.C. The defect fluorite phase in the ZrO_2-$PrO_{1.5}$ system and its relationship to the structure of pyrochlore. Australian Journal of Chemistry **1992**, *45* (9), 1375-1395.

[111] Holliday, K.; Finkeldei, S.; Neumeier, S.; Walther, C.; Bosbach, D.; Stumpf, T. TRLFS of Eu^{3+} and Cm^{3+} doped $La_2Zr_2O_7$: a comparison of defect fluorite to pyrochlore structures. Journal of Nuclear Materials **2013**, *433*, 479-485.

[112] Görller-Walrand, C.; Binnemans, K., Handbook on the physics and chemistry of rare earths. Elsevier: Amsterdam, **1996**.

[113] Hirayama, M.; Sonoyama, N.; Yamada, A.; Kanno, R. Relationship between structural characteristics and photoluminescent properties of $(La_{1-x}Eu_x)_{(2)}M_2O_7$ (M = Zr, Hf, Sn) pyrochlores. Journal of Luminescence **2008**, *128* (11), 1819-1825.

[114] Clark, D.L.; Hecker, S.S.; Jarvinen, G.D.; Neu, M.P. Plutonium. Chap. 7 in The Chemistry of the Actinide and Transactinide Elements, 4th ed.; Morss, L.R.; Edelstein, N.M.; Fuger, J., Springer: Dordrecht, pp 813-1264, **2010**.

[115] Glazyrin, S.A.; Rodchenko, P.Y.; Sokhina, L.P. Oxidation of plutonium(IV) during thermal treatment of its highly concentrated nitric acid solutions. Radiokhimiya **1989**, *31* (4), 48-52.

[116] Jarvenin, G. Precipitation and crystallization processes. http://www.cresp.org/wordpress/wp-content/uploads/2011/12/11%20-%20Complexation%20Chemistry%20and%20Precipitation_Crystallization%20Processes.pdf (accessed 06.09.2014).

[117] David, F.; Fourest, B.; Duplessis, J. Hydration thermodynamics of plutonium and transplutonium ions. Journal of Nuclear Materials **1985**, *130*, 273-279.

[118] Finkeldei, S.; Brandt, F.; Bukaemskiy, A.A.; Neumeier, S.; Modolo, G.; Bosbach, D. Synthesis and dissolution kinetics of zirconia based ceramics. Progress in Nuclear Energy **2014**, *72*, 130-133.

[119] Finkeldei, S.; Brandt, F.; Rozov, K.; Bukaemskiy, A.A.; Neumeier, S.; Bosbach, D. Dissolution of ZrO_2 based pyrochlores in the acid pH range: a macroscopic and electron microscopy study. Applied Geochemistry **2014**, *49,* 31-41.

[120] Kamizono, H.; Hayakawa, I.; Muraoka, S. Durability of zirconium-containing ceramic waste forms in water. Journal of the American Ceramic Society **1991**, *74* (4), 863-864.

[121] Wagner, T.; Kulik, D.A.; Hingerl, F.F.; Dmytrieva, S.V. GEM-Selektor geochemical modeling package: TSolMod library and data interface for multicomponent phase models. The Canadian Mineralogist **2012**, *50* (5), 1173-1195.

[122] Casey, W.H.; Bunker, B. Leaching of mineral and glass surfaces during dissolution. in Mineral water interface geochemistry., Hochella, M.F.; Bancroft, G.M., Mineralogical Society of America: Washington, D.C., p 603, **1990**.

[123] Knauss, K.G.; Thomas J, W. Muscovite dissolution kinetics as a function of pH and time at 70°C. Geochimica et Cosmochimica Acta **1989**, *53* (7), 1493-1501.

[124] Wehrli, B. Monte Carlo simulations of surface morphologies during mineral dissolution. Journal of Colloid and Interface Science **1989**, *132* (1), 230-242.

[125] Szenknect, S.; Mesbah, A.; Horlait, D.; Clavier, N.; Dourdain, S.; Ravaux, J.; Dacheux, N. Kinetics of structural and microstructural changes at the solid/solution interface during dissolution of cerium(IV)–neodymium(III) oxides. The Journal of Physical Chemistry C **2012**, *116* (22), 12027-12037.

[126] Tocino, F.; Szenknect, S.; Mesbah, A.; Clavier, N.; Dacheux, N. Dissolution of uranium mixed oxides: the role of oxygen vacancies vs the redox reactions. Progress in Nuclear Energy **2013**, *72*, 101-106.

[127] *PHREEQC 2.15 A computer program for speciation, batch-reaction, one-dimentional transport and inverse geochemical calculation.*; U.S. Geological Survey.; **1999**.

[128] Pouchon, M.A. Contribution to the study of a zirconia based nuclear fuel for plutonium use in light water reactor. University of Geneva, **2000**.

[129] Pouchon, M.A.; Curti, E.; Degueldre, C.; Tobler, L. The influence of carbonate complexes on the solubility of zirconia: new experimental data. Progress in Nuclear Energy **2001**, *38* (3–4), 443-446.

[130] Kovalenko, P.N.; Bagdasarov, K.N. Opredelenie rastvorimosti gidrookisi tsirkoniya. Zhurnal Neorganicheskoi Khimii **1961**, *6* (3), 534-538.

[131] Sheka, I.A.; Pevzner, T.V. Rastvorimost gidrookisei tsirkoniya I gafniya V rastvorakh edkogo natra. Zhurnal Neorganicheskoi Khimii **1960**, *5* (10), 2311-2314.

[132] Bilinski, H.; Branica, M.; Sillen, L.G. Precipitation and hydrolysis of metallic ions .2. Studies on solubility of zirconium hydroxide in dilute solutions and in 1 M $NaClO_4$. Acta Chemica Scandinavica **1966**, *20* (3), 853-861.

[133] Curti, E.; Degueldre, C. Solubility and hydrolysis of Zr oxides: a review and supplemental data. Radiochimica Acta **2002**, *90* (9-11), 801-804.

[134] Baes, C.F.; Mesmer, R.E., The hydrolysis of cations. R.E. Krieger: Malabar, Fla., **1986**.

[135] Hingant, N.; Clavier, N.; Dacheux, N.; Barre, N.; Hubert, S.; Obbade, S.; Taborda, F.; Abraham, F. Preparation, sintering and leaching of optimized uranium thorium dioxides. Journal of Nuclear Materials **2009**, *385* (2), 400-406.

[136] Bellière, V.; Joorst, G.; Stephan, O.; de Groot, F.M.F.; Weckhuysen, B.M. Phase segregation in cerium−lanthanum solid solutions. The Journal of Physical Chemistry B **2006**, *110* (20), 9984-9990.

[137] Lei, Y.; Ito, Y.; Browning, N.D.; Mazanec, T.J. Segregation effects at grain boundaries in fluorite-structured ceramics. Journal of the American Ceramic Society **2002**, *85* (9), 2359-2363.

[138] Luo, M.-F.; Yan, Z.-L.; Jin, L.-Y.; He, M. Raman spectroscopic study on the structure in the surface and the bulk shell of $Ce_xPr_{1-x}O_{2-\delta}$ mixed oxides. The Journal of Physical Chemistry B **2006**, *110* (26), 13068-13071.

11 Acknowledgements

Ich möchte mich bei meinem Doktorvater Herrn Professor Dirk Bosbach für die Möglichkeit diese Doktorarbeit anzufertigen und für seine stetige Unterstützung bedanken. Bei Herrn Professor Georg Roth möchte ich mich für die Übernahme der Zweitbegutachtung und eine konstruktive Diskussion zu dieser Arbeit bedanken.

Besonders herzlich möchte ich mich bei Herrn Dr. Felix Brandt und Herrn PD Dr. Giuseppe Modolo für die hervorragende Betreuung, stete Diskussionsbereitschaft und freundschaftliche Unterstützung bei der Erstellung dieser Arbeit bedanken. Herrn Dr. Andrey Bukaemskiy und Frau Dr. Martina Klinkenberg danke ich für zahlreiche Anregungen und Hilfestellungen in allen Phasen dieser Doktorarbeit.

Herrn Dr. Kiel Holliday, Professor Clemens Walther und Professor Thorsten Stumpf danke ich besonders für die Möglichkeit, am KIT-INE meine Proben mittels TRLFS zu charakterisieren und für ihre Unterstützung bei der Auswertung.

Nachfolgend möchte ich mich bei meinen internationalen Kooperationspartnern bedanken:
Herrn Professor Neil Hyatt und Herrn Dr. Martin Stennett von der University of Sheffield danke ich für die TEM Aufnahmen und die Hilfestellung bei der Auswertung.
Herrn Dr. Frodo Klaassen, Frau Dr. Eva de Visser – Týnová, Frau Jessica Bruin und Herrn Paul van den Idsert danke ich für die Bereitstellung des Plutoniumnitrats und die Möglichkeit, in den Laboren von NRG in Petten (NL) mein Pu-Pyrochlore zu synthetisieren.
Frau Dr. Stéphanie Szenkneckt und Herrn Johann Ravaux danke ich für die Unterstützung und Weiterführung des mikroskopischen Auflösungsexperimentes am ICSM in Marcoule (FR).
Herrn Associate Professor Nigel Marks und Herrn Professor Brendan Kennedy danke ich für anregende Diskussionen in Australien über die Ordnungs- und Unordnungsphänomene im Pyrochlor.

Herrn Professor Andreas Lüttge und Herrn PD Dr. Cornelius Fischer von der Universität Bremen sei für VSI Aufnahmen und die konstruktive Diskussion meiner Daten aus den Auflösungsexperimenten gedankt.

Herrn Professor Tobias Reich und Herrn Dr. Samer Amayri danke ich, dass sie mich an ihrem Wissen über die Plutoniumchemie teilhaben ließen.

Besonders bedanken möchte ich mich bei Herrn Dr. Andreas Wilden für seine Unterstützung. Herrn Dr. Konstantin Rozov danke ich für thermodynamische Modellierungen und Herrn Dr. Piotr Kowalski und Herrn Dr. Yan Li für atomistische Modellrechnungen.
Bei der Arbeitsgruppe von PD Dr. Hartmut Schlenz bedanke ich mich für die Röntgendiffraktometriemessungen.
Herrn Volker Bader danke ich für die Durchführung zahlreicher thermischer Behandlungen meiner Proben und Frau Sigrid Schwartz-Lückge für die BET-Messungen meiner Pulverproben.
Bei Herrn Fabian Sadowski möchte ich mich für unzählige ICP-MS Messungen bedanken.
Für ihre Hilfe bei der Probenpräparation danke ich Özlem Yilmaz, Tim Schuppik, Yulia Arinicheva, Rainer Engelmann und Dennis Heckroth.
Meinen Kollegen im IEK-6 danke ich für die gute Arbeitsatmosphäre und Zusammenarbeit. Besonders bedanken möchte ich mich bei Herrn Dr. Stefan Neumeier, Herrn Dr. Guido Deissmann, Frau Dr. Carole Babelot, Julia Heuser, Herrn Dr. Clemens Listner, Herrn Christian Schreinemachers, Herrn Dr. Henrik Daniels, Juliane Weber, Herrn Dr. Thomas Krings, Herrn Alexander Knott und Jana Assenmacher.

Meiner Schwester Ines, meiner Oma Lotte und meinem Papa, danke ich dafür, dass sie immer an mich geglaubt haben und mich in allen Phasen dieser Arbeit unterstützt und ermutigt haben weiter zu machen.
Lydia, Claudia und ihren Familien danke ich dafür, dass sie mir in all den Jahren immer ein zweites Zuhause waren.

Lynn, Janine und Hans möchte ich für Ihre Unterstützung und Aufmunterung danken.

Parts of this thesis have already been published:

Holliday, K.; Finkeldei, S.; Neumeier, S.; Walther, C.; Bosbach, D.; Stumpf, T. TRLFS of Eu^{3+} and Cm^{3+} doped $La_2Zr_2O_7$: a comparison of defect fluorite to pyrochlore structures. Journal of Nuclear Materials **2013**, *433*, 479-485.

Finkeldei, S.; Brandt, F.; Bukaemskiy, A.A.; Neumeier, S.; Modolo, G.; Bosbach, D. Synthesis and dissolution kinetics of zirconia based ceramics. Progress in Nuclear Energy **2014**, *72*, 130-133.

Finkeldei, S.; Brandt, F.; Rozov, K.; Bukaemskiy, A.A.; Neumeier, S.; Bosbach, D. Dissolution of ZrO_2 based pyrochlores in the acid pH range: a macroscopic and electron microscopy study. Applied Geochemistry **2014**.

Conference Presentation

Finkeldei, S., Holliday, K., Brandt, F., de Visser-Týnová, E., Bruin, J., Neumeier, S., Modolo, G., and Bosbach, D., 2014, Structural Uptake of Actinides by Zirconia Based Pyrochlores, IUMRS-ICA 2014, Fukuoka, Japan.

Finkeldei, S., Pyrochlore as Nuclear Waste Form: Actinide Uptake and Chemical Stability, 2014, HITEC Symposium, Jülich. (**HITEC Communicator Award***).*

Finkeldei, S., Brandt, F., Bukaemskiy, A., Holliday, K. S., de Visser-Týnova, E., Bruin, J., Neumeier, S., Modolo, G., and Bosbach, D., 2013, Zirconia based Nuclear Waste Forms for Actinides: Synthesis and dissolution Kinetics, GDCh Wissenschaftsforum Chemie 2013: Darmstadt, Germany.

Finkeldei, S., Brandt, F., Bukaemskiy, A., Neumeier, S., Modolo, G., and Bosbach, D., 2013, Dissolution kinetics of ZrO_2 based ceramics, E-MRS Spring Meeting: Strasbourg, Germany.

Finkeldei, S., Brandt, F., Bukaemskiy, A., Neumeier, S., Modolo, G., and Bosbach, 2013, Dissolution kinetics of ZrO_2 based innovative waste forms, Goldschmidt Conference: Florence, Italy.

Finkeldei, S., Brandt, F., Holliday, K., Bukaemskiy, A., Arinicheva, J., Neumeier, S., Modolo, G., and Bosbach, D., 2012, Conditioning of Minor Actinides in Zirconate based Pyrochlore-type Ceramics, ATALANTE 2012- Nuclear Chemistry for Sustainable Fuel Cycles: Le Corum Montpellier, France.

Finkeldei, S., Bukaemskiy, A., Neumeier, S., Brandt, F., Schlenz, H., Modolo, G., and Bosbach, D., 2012, Conditioning of Minor Actinides in Zirconate Based Pyrochlore, EMPG 2012 Conference: Kiel.

Bukaemskiy, A., Finkeldei, S., Arinicheva, Y., Brandt, F., Neumeier, S., Modolo, G., and Bosbach, D., 2013, Evolution of phase compositions and crystallization behavior of different ceramics for nuclear applications, Euromat 2013 Conference: Sevilla, Spain.

Neumeier, S., Babelot, C., Finkeldei, S., Schuppik, T., Bukaemskiy, A. A., Brandt, F., Schlenz, H., Modolo, G., and Bosbach, D., 2012, Conditioning of Minor Actinides in Monazite- and Pyrochlore-type Ceramics, E-MRS Spring Meeting: Strasbourg, France.

Neumeier, S., Brandt, F., Bosbach, D., Bukaemskiy, A., Finkeldei, S., Arinicheva, Y., Heuser, J., Ebert, E., Schreinemachers, C., Wilden, A., and Modolo, G., 2014, Ceramic Waste Forms: Present status and perspectives, International Conference and exposition on Advanced Ceramics and Composites: Daytona Beach, Florida, US.

Neumeier, S., Bukaemskiy, A., Brandt, F., Finkeldei, S., Arinicheva, Y., Modolo, G., and Bosbach, D., 2013, Ceramic waste forms for the conditioning of minor actinides, First Russian Nordic Symposium on Radiochemistry (RNSR): Moscow, Russia.

Neumeier, S., Finkeldei, S., Arinicheva, Y., Bukaemskiy, A., Brandt, F., Modolo, G., and Bosbach, D., 2013, Mechanical properties and dissolution behaviour of Monazite- and Pyrochlore-type ceramics for the immobilization of Minor Actinides, Euromat 2013 Conference: Sevilla, Spain.

Poster

Finkeldei, S., Holliday, K., de Visser-Týnová, E., Bruin, J., Brandt, F., Neumeier, S., Modolo, G., Stumpf, T., and Bosbach, D., 2013, Pyrochlore – a promising host phase for actinide immobilization, Actinides 2013: Karlsruhe, Germany. (**Best Poster Award**)

Finkeldei, S., Holliday, K., Neumeier, S., Walther, C., Bosbach, D., and Stumpf, T., 2012, Time-resolved laser fluorescence of Cm^{3+} and Eu^{3+} doped $La_2Zr_2O_7$, International Workshop on ATAS: Dresden-Rossendorf, Germany.

Finkeldei, S., Neumeier, S., Bukaemskiy, A., Schlenz, H., Modolo, G., Bosbach, D., Holliday, K., and Stumpf, T., 2011, Synthesis and characterization of ZrO_2 based ceramics for nuclear waste management, 494. WE-Heraeus-Seminar, Bad Honnef.

Finkeldei, S., Neumeier, S., Bukaemskiy, A., Schlenz, H., Modolo, G., and Bosbach, D., 2011, Darstellung und Charakterisierung ZrO_2 basierter Keramiken für die nukleare Entsorgung, GDCh-Tagung 2011: Bremen.

Bukaemskiy, A., Finkeldei, S., Brandt, F., Neumeier, S., Modolo, G., and Bosbach, D., 2013, Phase stability of Zirconia based Pyrochlore ceramics, CALPHAD XLII: San Sebastian, Spain.

Band / Volume 263
The role of soil heterogeneity on field scale evapotranspiration: 3D integrative modelling and upscaling of root water uptake
K. Huber (2015), xii, 128 pp
ISBN: 978-3-95806-057-9

Band / Volume 264
Strontium-Diffusion in Cer-Gadolinium-Oxid als Degradationsmechanismus der Festoxid-Brennstoffzelle
T. Mandt (2015), iii, 160 pp
ISBN: 978-3-95806-058-6

Band / Volume 265
Cluster analysis of European surface ozone observations for evaluation of MACC reanalysis data
O. Lyapina (2015), 187 pp
ISBN: 978-3-95806-060-9

Band / Volume 266
Real-time quantification of oxygen isotope exchange between carbon dioxide and leaf/soil water in terrestrial ecosystems with laser-based spectroscopy
L. Gangi (2015), XX, 156 pp
ISBN: 978-3-95806-061-6

Band / Volume 267
Secondary Uranium Phases of Spent Nuclear Fuel – CoXnite, $USiO_4$, and Studtite, $UO_4 4H_2O$ – Synthesis, Characterization, and Investigations Regarding Phase Stability
S. Labs (2015), 153, xlii pp
ISBN: 978-3-95806-063-0

Band / Volume 268
Chemische, verfahrenstechnische und ökonomische Bewertung von Kohlendioxid als Rohstoff in der chemischen Industrie
A. Otto (2015), viii, 272 pp
ISBN: 978-3-95806-064-7

Band / Volume 269
Energetische und wirtschaftliche Optimierung eines membranbasierten Oxyfuel-Dampfkraftwerkes
Y. Nazarko (2015), IV, 337 pp
ISBN: 978-3-95806-065-4

Band / Volume 270
Investigation of light propagation in thin-film silicon solar cells by dual-probe scanning near-field optical microscopy
S. Lehnen (2015),120 pp
ISBN: 978-3-95806-066-1

Band / Volume 271
Characterization of soil water content variability at the catchment scale using sensor network and stochastic modelling
W. Qu (2015), XVI, 123 pp
ISBN: 978-3-95806-067-8

Band / Volume 272
Light Absorption and Radiative Recombination in Thin-Film Solar Cells
T. C. M. Müller (2015), ii, 146 pp
ISBN: 978-3-95806-068-5

Band / Volume 273
Innenbeschichtung poröser Körper mittels Atomlagenabscheidung zur Redoxstabilisierung anodengestützter Festoxidbrennstoffzellen
T. Keuter (2015), XII, 133 pp
ISBN: 978-3-95806-069-2

Band / Volume 274
Thermochemical Modeling of Laves Phase Containing Ferritic Steels
A. Jacob (2015), 200 pp
ISBN: 978-3-95806-070-8

Band / Volume 275
Lithiumbatterien für stationäre und mobile Anwendungen: Benchmarking und experimentelle Umsetzung
T. Bergholz (2015), vi, 387 pp
ISBN: 978-3-95806-071-5

Band / Volume 276
Pyrochlore as nuclear waste form: actinide uptake and chemical stability
S. C. Finkeldei (2015), IX, 155 pp
ISBN: 978-3-95806-072-2

Energie & Umwelt /
Energy & Environment
Band / Volume 276
ISBN 978-3-95806-072-2